

Super-resolution microscopy of plasma membrane receptors



Doctoral thesis for a doctoral degree
at the Julius-Maximilians-Universität Würzburg

submitted by
Patrick Eiring
from Schweinfurt

Würzburg, 2021



Submitted on:

.....

Office stamp

Members of the Thesis Committee

Chairperson:

.....

Primary Supervisor: Prof. Dr. Markus Sauer

Supervisor (Second): Prof. Dr. Martin Kortüm

Date of Public Defence:

Date of Receipt of Certificates:

.....

Abstract

Plasma membrane receptors are the most crucial and most commonly studied components of cells, since they not only ensure communication between the extracellular space and cells, but are also responsible for the regulation of cell cycle and cell division. The composition of the surface receptors, the so-called "Receptome", differs and is characteristic for certain cell types. Due to their significance, receptors have been important target structures for diagnostic and therapy in cancer medicine and often show aberrant expression patterns in various cancers compared to healthy cells. However, these aberrations can also be exploited and targeted by different medical approaches, as in the case of personalized immunotherapy. In addition, advances in modern fluorescence microscopy by so-called single molecule techniques allow for unprecedented sensitive visualization and quantification of molecules with an attainable spatial resolution of 10-20 nm, allowing for the detection of both stoichiometric and expression density differences.

In this work, the single molecule sensitive method dSTORM was applied to quantify the receptor composition of various cell lines as well as in primary samples obtained from patients with hematologic malignancies. The focus of this work lies on artefact-free quantification, stoichiometric analyses of oligomerization states and co-localization analyses of membrane receptors.

Basic requirements for the quantification of receptors are dyes with good photoswitching properties and labels that specifically mark the target structure without generating background through non-specific binding. To ensure this, antibodies with a predefined DOL (degree of labeling) were used, which are also standard in flow cytometry. First background reduction protocols were established on cell lines prior analyses in primary patient samples. Quantitative analyses showed clear expression differences between the cell lines and the patient cells, but also between individual patients.

An important component of this work is the ability to detect the oligomerization states of receptors, which enables a more accurate quantification of membrane receptor densities compared to standard flow cytometry. It also provides information about the activation of a certain receptor, for example of FLT3, a tyrosine-kinase, dimerizing upon activation. For this purpose, different well-known monomers and dimers were compared to distinguish the typical localization statistics of single bound antibodies

from two or more antibodies that are in proximity. Further experiments as well as co-localization analyses proved that antibodies can bind to closely adjacent epitopes despite their size.

These analytical methods were subsequently applied for quantification and visualization of receptors in two clinically relevant examples. Firstly, various therapeutically relevant receptors such as CD38, BCMA and SLAMF7 for multiple myeloma, a malignant disease of plasma cells, were analyzed and quantified on patient cells. Furthermore, the influence of *TP53* and *KRAS* mutations on receptor expression levels was investigated using the multiple myeloma cell lines OPM2 and AMO1, showing clear differences in certain receptor quantities.

Secondly, FLT3 which is a therapeutic target receptor for acute myeloid leukemia, was quantified and stoichiometrically analyzed on both cell lines and patient cells. In addition, cells that have developed resistance against midostaurin were compared with cells that still respond to this type I tyrosine-kinase-inhibitor for their FLT3 receptor expression and oligomerization state.

Zusammenfassung

Plasmamembranrezeptoren sind die wohl wichtigsten und meist untersuchten Komponenten einer Zelle, da sie nicht nur die Kommunikation zwischen dem extrazellulären Bereich und den Zellen gewährleisten, sondern auch für die Regulierung des Zellzyklus und der Zellteilung zuständig sind. Dabei unterscheidet sich die Zusammensetzung der Oberflächenrezeptoren, das sogenannte „Rezeptom“, und ist charakteristisch für bestimmte Zelltypen. Aufgrund ihrer Bedeutsamkeit sind Rezeptoren wichtige Zielstrukturen für Diagnose und Therapie in der Krebsmedizin, welche häufig bei verschiedensten Krebserkrankungen im Vergleich zu gesunden Zellen aberrante Expressionsmuster aufweisen. Diese Abweichungen können sich allerdings auch zu Nutzen gemacht werden und zum Ziel verschiedener medizinischer Behandlungsmethoden, wie es bei der personalisierten Immuntherapie der Fall ist, werden. Zusätzlich hat der Fortschritt in der modernen Fluoreszenzmikroskopie durch sogenannte Einzelmolekültechniken, es auch erlaubt, eine noch nie dagewesene empfindliche Visualisierung und Quantifizierung von Molekülen mit einer räumlichen Auflösung von 10-20 nm zu erreichen, wodurch sowohl stöchiometrische Unterschiede, als auch Unterschiede in der Expressionsdichte detektiert werden können.

In dieser Arbeit wurde die einzelmolekülsensitive Methode *d*STORM genutzt, um die Rezeptorkomposition von verschiedenen Zelllinien aber auch von primären Patientenzellen mit zugrundeliegenden hämatologischen Erkrankungen zu quantifizieren. Schwerpunkte dieser Arbeit sind dabei die artefaktfreie Quantifizierung, stöchiometrische Analysen von Oligomerisierungszuständen, sowie die Kollokalisationsanalyse von Membranrezeptoren.

Grundvoraussetzung für die Quantifizierung von Rezeptoren sind dabei gut schaltbare Farbstoffe, sowie Label, welche die Zielstruktur spezifisch markieren ohne dabei Hintergrund durch unspezifische Bindung zu generieren. Um dies zu gewährleisten, kamen Antikörper mit einem vordefinierten DOL (degree of labeling; engl. für: Markierungsgrad) zum Einsatz, welche auch in der Durchflusszytometrie standardmäßig eingesetzt werden. Protokolle zur Hintergrundreduktion wurden dabei an Zelllinien etabliert, bevor Primärzellen von Krebspatienten analysiert wurden. Durch quantitative Analysen konnten dabei deutliche Expressionsunterschiede zwischen den

Zelllinien und den Patientenzellen, aber auch zwischen den verschiedenen Patienten gezeigt werden.

Ein wichtiger Bestandteil dieser Arbeit ist die Fähigkeit, den Oligomerisierungszustand von Rezeptoren zu erkennen, was eine genauere Quantifizierung der Membranrezeptordichten im Vergleich zur Durchflusszytometrie ermöglicht. Allerdings können diese Oligomerisierungszustände auch Informationen über die Aktivierung eines Rezeptors beinhalten, wie zum Beispiel von FLT3, einer Tyrosinkinase, welche zur Aktivierung dimerisieren muss. Hierfür wurden verschiedene bekannte Monomere und Dimere verglichen, um die typische Lokalisationsstatistik von vereinzelt gebundenen Antikörpern mit der von zwei oder mehr Antikörpern, welche nah beieinanderliegen, zu vergleichen. Durch weitere Etablierungsexperimente sowie Koloalisationsanalysen konnte außerdem bewiesen werden, dass Antikörper trotz ihrer Größe auch an nah benachbarte Epitope binden können.

Diese Analyseverfahren wurden im weiteren Verlauf zur Quantifizierung und Visualisierung von Rezeptoren an zwei klinisch relevanten Beispielen angewendet. Zum einen wurden verschiedene therapeutisch relevante Rezeptoren wie z.B. CD38, BCMA und SLAMF7 für das Multiple Myelom, einer malignen Erkrankung von Plasmazellen, auf Patientenzellen analysiert und quantifiziert. Zusätzlich wurde der Einfluss von *TP53* und *KRAS* Mutationen auf die Rezeptorexpressionen anhand der Multiplen Myelom Zelllinien OPM2 und AMO1 untersucht, bei denen eindeutige Unterschiede in der Rezeptorexpression detektiert wurden.

Zum anderen wurde FLT3, welches ein therapeutischer Zielrezeptor für die akute myeloische Leukämie ist, sowohl auf Zelllinien als auch auf Patientenzellen quantifiziert und stöchiometrisch analysiert. Hierbei wurden auch Zellen, welche eine Midostaurinresistenz entwickelt haben mit Zellen, welche auf diesen Typ I Tyrosinkinase Inhibitor ansprechen, auf ihre FLT3 Rezeptorexpression und ihren Oligomerisierungszustand verglichen.

Table of Contents

1	Introduction	1
1.1	Receptors and their importance for immunotherapy	1
1.2	Regulatory T cells and their main functions	4
1.3	Specific receptors and their main function	7
1.4	Multiple myeloma.....	9
1.5	The role of FLT3 in acute myeloid leukemia.....	11
1.6	Microscopy	12
1.6.1	Fluorescence microscopy	12
1.6.2	Confocal laser scanning microscopy.....	16
1.6.3	Super-resolution microscopy techniques	16
1.6.4	Quantification and analysis of SMLM data using Clustering algorithms	19
1.7	Objective of this work	21
2	Material and Methods.....	22
2.1	Cell culture	22
2.2	Cell thawing and plating	23
2.3	Antibody labeling	23
2.4	Live cell staining	25
2.5	Fixed cell staining	25
2.6	Imaging.....	27
2.6.1	Confocal Laser Scanning Microscope (CLSM)	27
2.6.2	One-color <i>d</i> STORM	28
2.6.3	Preparation of TetraSpeck sample.....	28
2.6.4	Two-color <i>d</i> STORM	29
2.6.5	Analysis of <i>d</i> STORM data by rapid <i>d</i> STORM, Locan and ImageJ.....	29
3	Results.....	31
3.1	Stoichiometric receptor quantification on Jurkat T cells.....	31
3.2	The Treg receptome	45
3.3	Multiple myeloma.....	49
3.3.1	CD38 detection on multiple myeloma cells	49
3.3.2	Promising targets for multiple myeloma	53
3.3.3	Influence of knock-out and point mutations on the receptor expression of multiple myeloma cells	58
3.4	Quantification of FLT3 on cell lines and primary patient cells	65
4	Discussion.....	68
4.1	Stoichiometric receptor quantification on cell lines	68

4.2	The Treg receptome	72
4.3	Multiple myeloma.....	74
4.3.1	CD38 detection on multiple myeloma	74
4.3.2	Promising targets for multiple myeloma	75
4.3.3	Influence of knock-out and point mutations on the receptor expression of multiple myeloma cells	78
4.4	Quantification of FLT3 on AML cell lines and primary cells	80
5	Conclusion and Outlook	83
6	Bibliography	89
	List of abbreviations.....	99
	Acknowledgement	101
	Publication list.....	103
	Affidavit.....	104
	Curriculum vitae.....	105

1 Introduction

1.1 Receptors and their importance for immunotherapy

Receptors are specialized protein complexes that are signal transducers and receivers, typically triggered upon binding of a ligand, leading to a signaling cascade with a cellular response (Heldin et al. 2016). Receptors can be divided into intracellular and cell surface receptors (Alberts et al. 2015). While intracellular receptors are located entirely inside the cell, plasma membrane receptors consist of an intracellular domain, a hydrophobic membrane-spanning region and an external ligand-binding domain, allowing communication between the extracellular space and the cells by messenger molecules (Alberts et al. 2015). Those cell surface receptors can be divided into three subgroups containing ion channel-linked receptors (Traynelis et al. 2010), G-protein-coupled receptors (Hilger, Masureel, and Kobilka 2018) and enzyme-linked receptors (Luo et al. 2019). Each receptor type has a specific function and expression levels can vary depending on environmental and genetic factors (Shahrabi et al. 2020).

To define the receptor composition on cell surfaces and to be able to compare results from different scientific working groups, a uniform classification system was defined during the first “International workshop and conference on human leukocyte differentiation antigens” in Paris in 1982 (WHO 1984). The aim was to characterize all known monoclonal antibodies and to group them depending on their targeted glycoprotein independent of the epitope. To date, more than 370 of these cell surface molecules, called clusters of differentiation (CDs), have been described and for most of them, at least partially, their main function is characterized (Engel et al. 2015). Because each cell type has a unique receptor composition on their surface, cell sorting is possible by their characteristic CDs (Herold and Mitra 2021).

Innovative cancer treatment relies on the immunophenotypic characterization of the target cell to confirm the presence or absence of specific surface epitopes. Ideally, targets would be present on the tumor, but not on healthy cells, however, such ideal targets are rare. Monoclonal antibodies (mAbs) are commonly used to tackle the tumor cells, such as rituximab, a mAb against CD20, which is used to treat lymphoma. However, also healthy B Cells are depleted using rituximab, causing side effects of various strengths. Monoclonal antibodies apply two different mechanisms of cell lysis for the killing of tumor cells (Figure 1): First, the mAb has the ability to induce close contact to immune effector cells like NK cells or T cells by binding to its fragment

crystallizable region (FcR), resulting in injection of cytokines and granules. This leads to a disruption of the cell membrane and therefore to an antibody dependent cell-mediated cytotoxicity (ADCC) (Saltarella et al. 2020). Second, complement component C1q can bind to IgM or IgG antibodies which activates the complement cascade and leads to the proteolytic release of the chemotactic/activating agents C3a and C5a that ultimately form a membrane attack complex inducing 100 Å pores in the cell membrane. Finally, high concentrations of C3a and C5a results in effector cells moving to the target cells. By modifying those mAbs with radioactive immunoconjugates or cytotoxic agents, so-called radioligands or immunoconjugates, the killing efficiency can be further increased when bound to their target receptor (Adams and Weiner 2005; Thomas, Teicher, and Hassan 2016).

Recently, a novel class of bispecific antibodies (BiTEs) has been introduced (Buss et al. 2012). BiTEs consist of two single-chain variable fragments (scFv) that have two antigen-binding domains (Figure 1) (Thakur, Huang, and Lum 2018). One targets a receptor on the aberrant cells while the other binding domain (typically CD3 for T cells) recruits a T cell resulting in an immune response similar to the ADCC caused by mAbs. This approach is highly efficient compared to monoclonal antibodies due to its higher affinity for low expressed targets (Thakur, Huang, and Lum 2018; Shim 2020).

A third upcoming approach applies genetically modified T cells. The T cells are isolated from the patients' blood and modified with special chimeric antigen receptors (CARs) against a target expressed on the malignant cells. After *ex-vivo* T cell expansion, the living CAR-T cells are given back to the patient (Whilding and Maher 2015; Subklewe, von Bergwelt-Baildon, and Humpe 2019). Binding of the target protein leads to a direct activating signaling cascade of the CAR-T cells resulting in lysing the malignant cells without the need of a TCR and antigen presentation (Figure 1). CAR-T cells consist of a short chain variable fragment (scFv) fused to an intracellular signaling domain. For first generation CARs only the CD3 ζ signaling domain is fused as activation molecule leading to a rather short immune response and low IL-2 production. This intracellular signaling domain has been further improved by adding co-stimulatory factors like 4-1BB or CD28 (2nd generation CARs) or even both co-stimulatory molecules to CD3 ζ (3rd generation CARs) for a long-lasting immune response without binding to their respective complementary receptor (Subklewe, von Bergwelt-Baildon, and Humpe 2019). Additionally, 4th generation CARs have been developed increasing safety of

therapy and minimizing toxicity and side effects by expressing certain domains. CARs of the 4th generation have i.e. additional safety switches (self-destruct CARs) or need at least two tumor-associated antigens on the targeted cells (Dual CARs) to be triggered (Petersen and Krenciute 2019).

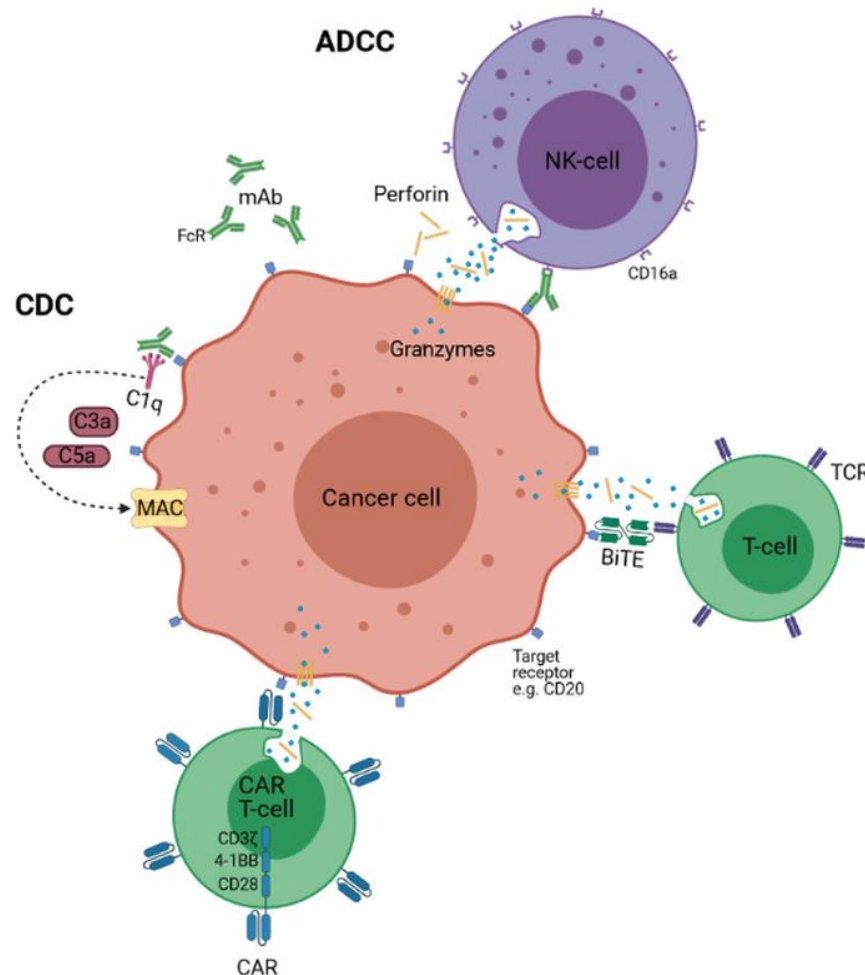


Figure 1 - Malignant cell lysis by different immunotherapeutic approaches. Specific monoclonal antibodies (mAbs) bind to an exogenous target expressed on the cancer cell and cause either a complement-dependent cytotoxicity (CDC) or an antibody dependent cell-mediated cytotoxicity (ADCC). During CDC the complement component 1q (C1q) binds to the mAb activating a signaling cascade resulting in release of C3a and C5a. Together with C5-9 the membrane attack complex is formed inducing pores and leading to cell lysis and death. However, ADCC makes use of effector cells that are able to bind to the fragment crystallizable region (FcR) establishing a close contact to the cancerous cell. Distribution of perforin and granzymes ultimately perforate the cell membrane leading to cell death. Bispecific antibodies (BiTE) consist of two single-chain variable Fragments (scFv) with one target binding domain and one binding to a specific receptor on immune cells e.g. TCR resulting in an ADCC. In addition, immune cells like T cells can be modified with chimeric antigen receptors (CARs) against a specific target receptor to mediate cell cytotoxicity. After binding, those 3rd generation CARs are activated because also co-stimuli like CD28 and 4-1BB, that are important for activation, are simultaneously triggered. Created with BioRender.com

Personalized receptor-directed therapies improved the overall survival rate of many patients with malignancies, but despite such innovative treatments, relapses are

common. In particular, multiple myeloma patients are not being cured, in part because CAR T cells do not persist in the patient, but diminish over time. To overcome this issue, checkpoint inhibitors have been identified to boost the innate immune system by inhibiting the immune-suppressive effect caused by certain surface molecules (Zander et al. 2020). Nowadays specific mAbs are approved for medical usage against certain checkpoint inhibitors like CTLA-4 and PD-1. Both can bind to their respective receptors on T cells inhibiting binding to a possible antigen presenting cell (APC). Additional stimulatory effects for T cells by APCs are also supported leading to a more effective immune response. Even though boosting the innate immune system seems like a promising approach, only a small percentage of the patients respond to this therapy and the success of therapy for individual patients cannot yet be adequately predicted (Zander et al. 2020; Robert 2020). With discovery of new checkpoint inhibitors and first successful therapies a new promising field has been opened for which specific biomarkers need to be identified to decide about efficacy and toxicity of this therapy.

1.2 Regulatory T cells and their main functions

The mammalian immune system is a complex machinery protecting its host from pathogenic organisms and aberrant cells while at the same time excessive immune reactions are avoided in healthy individuals (Sakaguchi et al. 2008). B and T cell populations are mainly responsible for immunosuppressive or harmful reactions, which can cause, if imbalanced or altered, autoimmune diseases or cancer (Kondelkova et al. 2010; Gol-Ara et al. 2012; Ohue and Nishikawa 2019). Nowadays, it is mainly accepted that specific T cells maintain the balance by regulating immune suppression (Sakaguchi 2011). The so-called regulatory T cells (Tregs) are a subpopulation of 2-10% of the total CD4⁺ T cell population. Those harbor inhibitory effects on the pro-inflammatory activity of cells (Venken et al. ; Niu et al. 2020). Two major subclasses of Tregs are known, which are distinguished based on their precursor cells and their site of origin and can be further separated into smaller subtypes (Venken et al. ; Zhang et al. 2014; Niedzwiecki et al. 2019). The best-investigated and understood phenotype is CD4⁺ CD25^{high} FoxP3⁺, also known as (natural) regulatory T cells derived from CD4⁺ thymocytes (tTregs) after TCR stimulation. This induces high CD25 expression on the cell surface to which IL-2 can bind causing an upregulation of the transcription factor

FoxP3 (Sakaguchi et al. 2008; Takeuchi and Nishikawa 2016). The second type of Tregs (pTregs) is thought to originate from conventional T effector cells in the periphery under certain conditions when IL-2 and TGF- β are present (Zheng et al. 2007) or are induced *in vitro* (iTregs) after TGF- β or retinoic acid stimulation (Coombes et al. 2007; Shevach and Thornton 2014). Even though transcription factors like Helios and Neuropilin-1 suggest a thymic origin, no true marker to separate tTregs and pTregs has been identified yet (Szurek et al. 2015; Thornton et al. 2019). It is, however, proposed that Tregs lacking the transcription factor Helios have less suppressive capability compared to Helios⁺ Tregs (Shevach and Thornton 2014; Thornton et al. 2019). Moreover, suppressive activity against specific T effector cells may be associated with expression of specific transcription factors of the T effector population while presumably being dependent on the cytokine background of the Treg environment (Ghoreschi et al. 2011; Shevryev and Tereshchenko 2019).

Immune suppression by tTregs is achieved through multiple mechanisms (Figure 2): Availability of IL-2 is strongly reduced for T effector cells by binding to its corresponding receptor CD25 that is highly abundant on regulatory T cells. Additionally, CTLA-4 can bind to CD80 and CD86 expressed on antigen presenting cells with higher affinity than CD28, both inhibiting co-stimulatory signals and transmitting suppressive signals. Production of TGF- β or the cytokines IL-10 and IL-35 cause further activity reduction of APCs or T effector cells and secreted perforin and granzymes can even lyse these cells. Large amounts of ATP produced by Tregs are converted by CD39 and CD73 to adenosine, which can also have immunosuppressive effects on T effector cells and APCs (Togashi, Shitara, and Nishikawa 2019). Additionally, Tregs express the immune checkpoint inhibitor PD-1 and its corresponding ligand PD-1L. Binding of the ligand to PD-1 on activated effector cells can lead to a missing reaction (anergy) or induce the transformation to pTregs. Signaling through this receptor is necessary for FoxP3 expression and Treg homeostasis (Gianchecchi and Fierabracci 2018; Shevryev and Tereshchenko 2019). For personalized immunotherapy Tregs are targeted to treat graft-versus-host diseases (GvHD) after organ transplantations and in autoimmune diseases but are also used for cancer therapies. A high Treg activity during a tumor burden is typically associated with a poor prognosis. Due to the tumor microenvironment, Tregs are often recruited to the tumor, helping this malignancy to evade immune response (Gun et al. 2019).

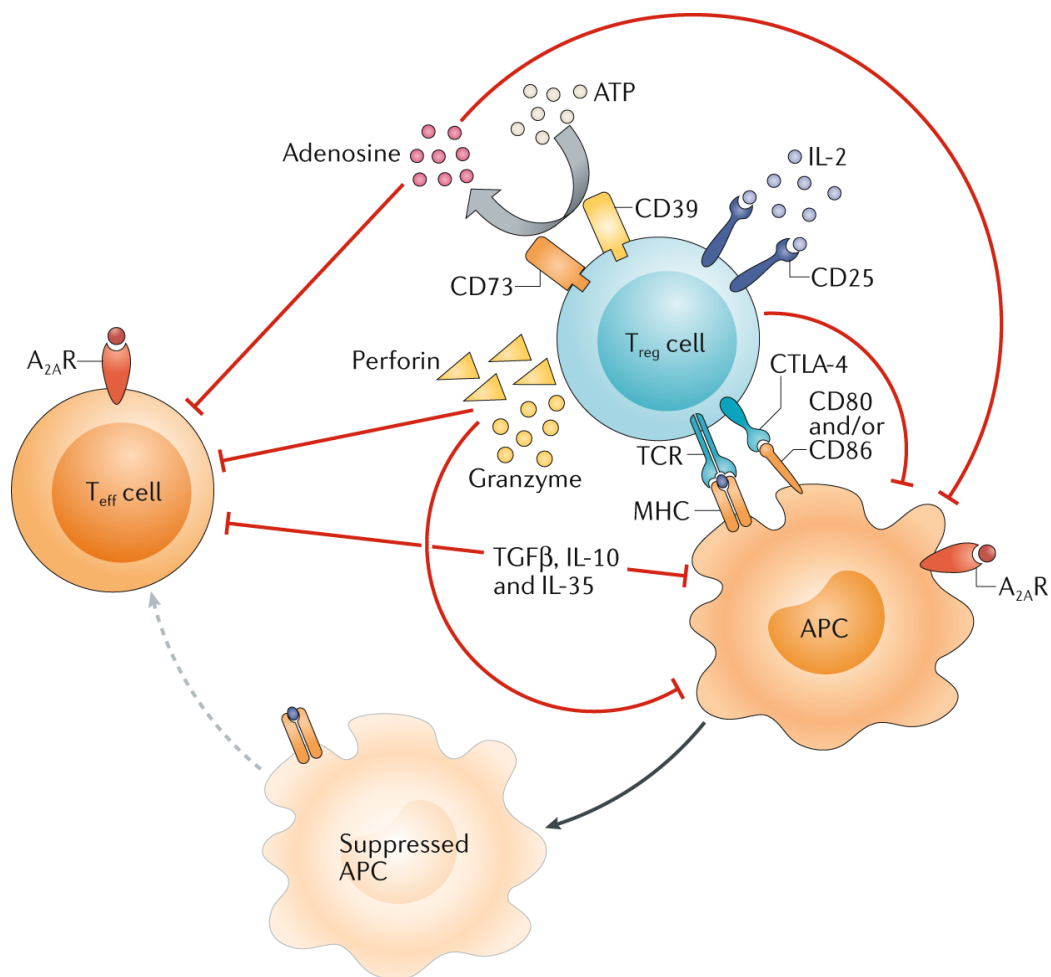


Figure 2 - Different mechanisms of Tregs suppressing immune response. IL-2 concentration is strongly reduced due to the high amount of CD25 expressed on Treg surface. In addition, CTLA-4 competes with CD28 for CD80 and CD86 expressed on APC, but has a greater affinity. Therefore, binding of CTLA-4 inhibits co-stimulatory effects caused by CD28, but also transmits suppressive signals. Production and release of TGF- β , IL-10 and IL-35 reduce activity of APC or T-effector cells. Moreover, secretion of perforin and granzymes can even kill those cells. Treg cells further produce large amounts of ATP, which is converted by CD39 and CD73 to adenosine which also has immune-suppressive effects on effector or APCs. Copyright permission was granted by Springer Nature. (Togashi, Shitara, and Nishikawa 2019)

Therefore, to achieve anti-tumor effects, the amount of present Treg cells is either reduced by certain drugs or their suppressive function is minimized by the blocking of checkpoint inhibitors resulting in an increased activity of immune cells helping the innate system to target syngeneic tumor cells (Verma et al. 2019). Patients with autoimmune diseases in contrast often lack effective Tregs causing the immune system to overreact and target healthy cells. Different therapies are currently under investigation to increase the number of active Tregs in patients by either *ex-vivo* expansion or by using activating or inducing drugs like IL-2 (Eggenhuizen, Ng, and Ooi 2020).

In contrast to the well-studied activation mechanism of T cells, immune suppression by Tregs is poorly investigated and understood. This is mainly caused by the lack of unique markers for phenotyping different Treg populations, but also by the poor knowledge of the underlying molecular mechanism by the actively suppressed cells (Schmidt, Oberle, and Krammer 2012; Shevryev and Tereshchenko 2019).

1.3 Specific receptors and their main function

Plasma membrane surface receptor combinations on malignant and healthy cells are highly variable. In the following chapter, a selection of important cell surface receptors, which were analyzed as part of this thesis, are described.

CD2 (LFA-2) is a 39.4 kDa transmembrane glycoprotein expressed especially on T cells and a subset of NK-cells, but also on thymocytes and dendritic cells. It is known that CD2 tends to partially dimerize up to 15-30% and is involved in T-cell activation as a co-stimulatory effector when bound to CD58 (LFA-3) or CD48, albeit with a much lower affinity (Murray et al. 1995; Espagnolle et al. 2007).

CD3 is a protein complex consisting of CD3 γ chain, a CD3 δ chain, and two CD3 ϵ chains. When associated together with the T cell receptor (TCR) and two intracellular CD3 ζ domains an activating signal is generated. The TCR-CD3 protein complex induces aggregation of adhesion structures and co-receptors on T cells. Upon activation, CD3 organizes in clusters ranging from a few nanometers to more than a micrometer in size (Pageon et al. 2016).

CD11a/CD18 (LFA-1) is a leucocyte specific heterodimeric integrin with non-covalently linked subunits (Semmrich et al. 2005; Takada, Ye, and Simon 2007). During blood circulation β 2 integrins (CD18) are in an inactive non-binding low affinity conformation. Co-stimulation by other receptors trigger inside-out signaling leading to an activation and therefore to an extension of subunits. This high-affinity state exists only transiently and has to be stabilized with divalent cations (Dransfield et al. 1992; Shattil, Kim, and Ginsberg 2010). In this state integrins can bind to the corresponding ligand ICAM and, for example, leave the bloodstream and emigrate to the side of an infection (Springer and Wang 2004).

CD19 is a 95 kDa transmembrane immunoglobulin, which is ubiquitous on B cells binding to CD81, CD82 and VAV2 (Thalappilly et al. 2010; Wang, Wei, and Liu 2012;

Zou et al. 2018). CD19 expression is highly regulated during B cell maturation and gets lost during plasma cell differentiation. During B cell receptor (BCR) activation CD19 acts as enhancer for BCR induced signaling, but still helps mediating regulatory functions in BCR signaling (Scheuermann and Racila 1995; Wang, Wei, and Liu 2012). Additionally, an abnormal CD19 expression on B cells in most cases is associated with an autoimmune disease or cancer, nowadays making it a preferred target in immunotherapy (Li et al. 2017).

CD20 is a ~35 kDa protein expressed on B Lymphocytes, some follicular dendritic cells and on low levels on a T cell subset (Pavlasova and Mraz 2020). CD20 is important for B cell activation and can form homodimers and homooligomers, which are thought to form Ca²⁺-conductive ion channels in the plasma membrane (Rouge et al. 2020).

CD138 (Syndecan-1) is a 30 kDa type I heparan sulfate proteoglycan that is found on plasma cells as well as on mature epithelial cells, mesenchymal cells, endothelial cells and pre-B cells (Palaiologou, Delladetsima, and Tiniakos 2014). It is important for cell proliferation, migration and adhesion. In addition, CD138 is involved in apoptosis, angiogenesis tumor invasion and metastasis, making it an important parameter for a patients' prognosis (Pasqualon et al. 2015; Akhmetzyanova et al. 2020).

CD269 (BCMA) is a 21 kDa transmembrane protein belonging to the tumor necrosis factor family (Huang et al. 2013). It is important for long term plasma cell survival and exclusively expressed on differentiated plasma cells and plasmablasts (Cho, Anderson, and Tai 2018). BCMA tends to form homodimers and is known to bind to the cell survival factor APRIL, making it a successful target for immunotherapy (Tai et al. 2016).

CD319 (SLAMF7) is a 66 kDa glycoprotein highly expressed on plasma and myeloma cells, but also to a certain amount on many NK cells, mostly CD56⁺ T cells, mature dendritic cells, a small subset of CD4⁺ T cells and B cells but also on some monocytes and macrophages (Campbell, Cohen, and Pazina 2018; Hsi et al. 2008; O'Connell et al. 2019). When EAT-2 is expressed and binds to the endogenous part of SLAMF7 an activation of cellular immune response is triggered in NK cells with a complementary effect in the absence of SLAMF7 (Campbell, Cohen, and Pazina 2018). In diseases characterized by chronic immune activation SLAMF7 is often overexpressed, making it an interesting target for mAb or CAR-T cell therapy (Campbell, Cohen, and Pazina

2018; Gogishvili et al. 2017; Prommersberger et al. 2021; Rasche, Einsele, and Nitschmann 2019)

1.4 Multiple myeloma

Multiple myeloma (MM) is a malignant disease originated from plasma cells and is the second most commonly diagnosed hematologic cancer with elderly patients affected at a median age of ~60 years or older (Kazandjian 2016). Even though this disease is well studied and investigations have been conducted for decades, MM remains incurable with an average survival of 5-7 years after diagnosis (White et al. 2021). To date, the underlying mechanisms that lead to MM are largely unknown, however, risk factors were identified that contribute to the development of this disease. This includes radiation exposure, certain chemicals, obesity or stress (Panaroni, Yee, and Raje 2017; Joshua et al. 2019).

Multiple myeloma is a genetically heterogeneous disease, which cannot be attributed to a single lesion and highly individualized disease courses are commonly observed. Only few genes are recurrently mutated such as *KRAS*, *BRAF* and *NRAS*, leading to an excess of growth signals, which contributes to uncontrolled proliferation of the affected cells (Joshua et al. 2019). The malignant plasma cells produce large amounts of monoclonal immunoglobulins (Figure 3), the so-called paraproteins that are used to assess treatment response and disease activity. Light chains produced can block the kidney tubules and in most patients impaired kidney function is being observed (Eslick and Talaulikar 2013).

Another characteristic of symptomatic MM is activation of osteoclasts leading to lytic lesions in the bones, so-called osteolysis, and many of the affected patients suffer from bone pain and pathologic fractures (Figure 3). This process can result in life-threatening hypercalcemia crises (Panaroni, Yee, and Raje 2017; Zamagni et al. 2018).

First treatment effects were observed in the 1960s with the alkylator melphalan combined with steroids (e.g. dexamethasone). Today, this compound is still applied in fit patients using a high-dose treatment, requiring autologous stem cell support to avoid long term aplasia (Joshua et al. 2019).

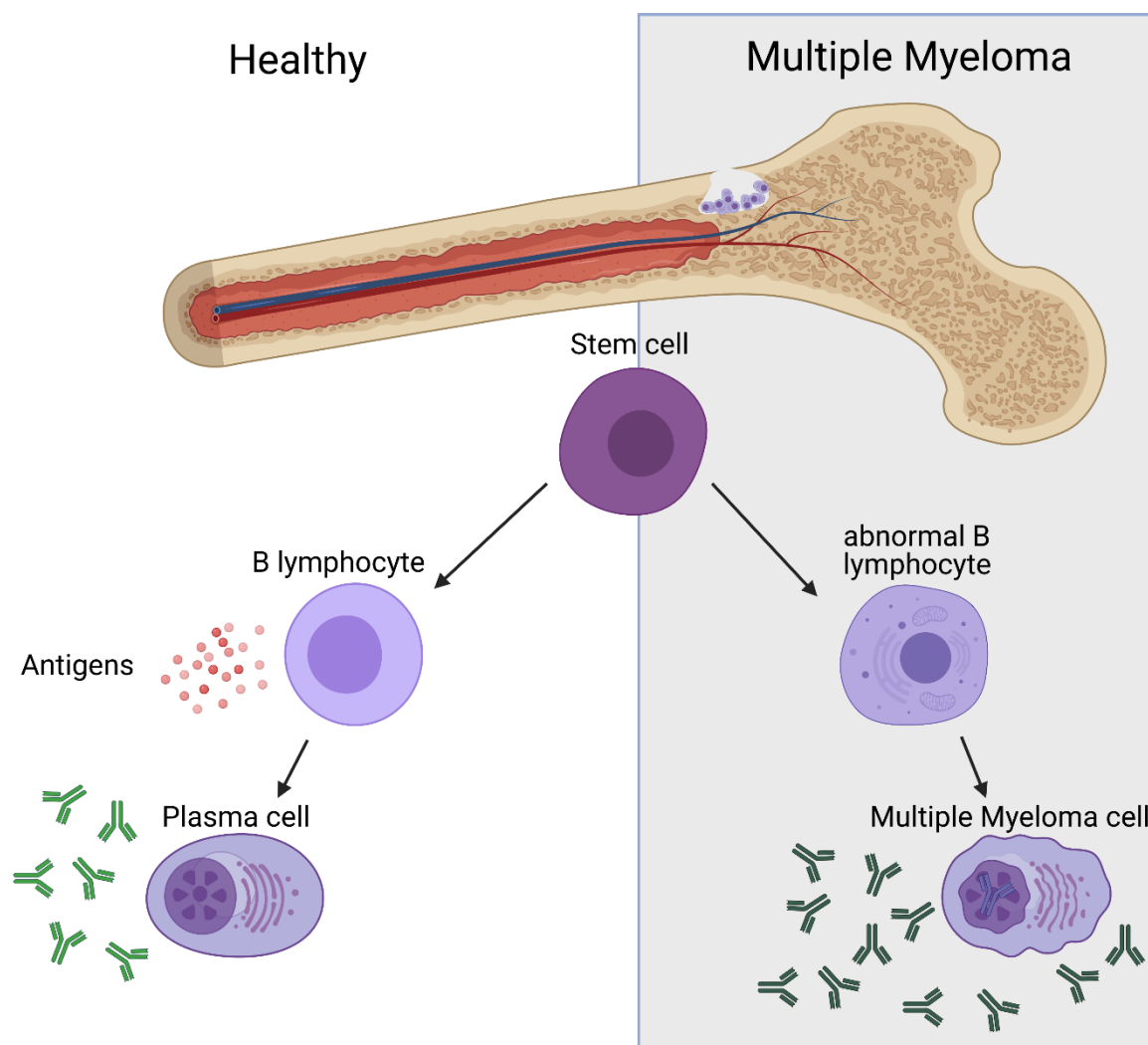


Figure 3 - Comparison of healthy plasma cells and malignant multiple myeloma cells. In healthy bone marrow stem cells can differentiate to B lymphocytes. When certain antigens are present, those B cells can develop into antibody-producing plasma cells. Due to mutations, uncontrolled proliferation transforms B cells into multiple myeloma cells producing the same antibody or unfinished paraproteins. In addition, myeloma cells recruit osteoclasts mainly involved in the degradation of bone tissue resulting in hypercalcemia, osteopenia and bone pain. Created with BioRender.com.

Since 2000, remarkable advances in MM treatment could be achieved, mainly through the approval of novel and highly active compounds, such as immunomodulators, proteasome inhibitors and monoclonal antibodies. These diverse treatment options increased the median survival, especially of younger patients, to 7-8 years (Joshua et al. 2019; Saltarella et al. 2020; Rodriguez-Lobato et al. 2020).

Most importantly, CD38 directed mAb immunotherapy has been incorporated in first line treatments in transplant eligible and transplant ineligible MM patients. By doing so, rate of responders and depth of remission could be significantly improved.

Most recently innovative immunotherapy has been approved or is being tested in late stage clinical trials including immunoconjugates, bispecific antibodies and CAR-T cells. Targets include most commonly BCMA, but also CD19, CD20, CD38, CD40, CD44, CD47, ICAM1, NCAM1, CD74, CD81, CD86, CD200, IGF1R, CD307, SLAMF7, PD-L1 are currently investigated and are possible promising targets for specific CAR-T cell approaches (Atanackovic et al. 2016; Rodriguez-Lobato et al. 2020).

1.5 The role of FLT3 in acute myeloid leukemia

Acute myeloid leukemia is a life threatening malignancy derived from hematopoietic cells with patients having a median age of ~68 years at diagnosis (Juliussen and Hough 2016). Affected cells are from the myeloid lineage, e.g., granulocytes, megakaryocytes and macrophages (Iwasaki and Akashi 2007; Prada-Arismendy, Arroyave, and Rothlisberger 2017). AML prognosis depends on the genetic subtype but also age and condition of the patient, whereas some patients can be cured others face dismal prognosis with only short survival (Swaminathan and Wang 2020). Molecular profiling is used in standard diagnostic workflows to identify the underlying mutations and to optimize therapy. (Liu et al. 2020). Today, patients can be divided into *favorable*, *intermediate* and *adverse* risk profiles (Dohner et al. 2017; Estey 2018).

One recurrent genetic alteration in AML is a internal tandem duplication (ITD) of the FMS-like tyrosine-kinase 3 (FLT3) receptor, detected in about 15-35% of all AML patients (Stirewalt and Radich 2003). FLT3 is a proto-oncogene important for proliferation, differentiation and survival of hematopoietic stem cells (De Kouchkovsky and Abdul-Hay 2016; Patnaik 2018). ITDs are a duplication of the gene sequence coding for the juxtamembrane that typically has an auto inhibitory function (Griffith et al. 2004). They are inserted in direct (head-to-tail) orientation resulting in a constitutive activation by autophosphorylation promoting a ligand-independent dimerization caused by the missing intrinsic negative regulatory effects of the juxtamembrane (Lagunas-Rangel and Chavez-Valencia 2017). As a consequence, signaling pathways like MAPK, STAT5 and AKT get activated resulting in cell proliferation and anti-apoptotic signals (Kiyoi, Kawashima, and Ishikawa 2020).

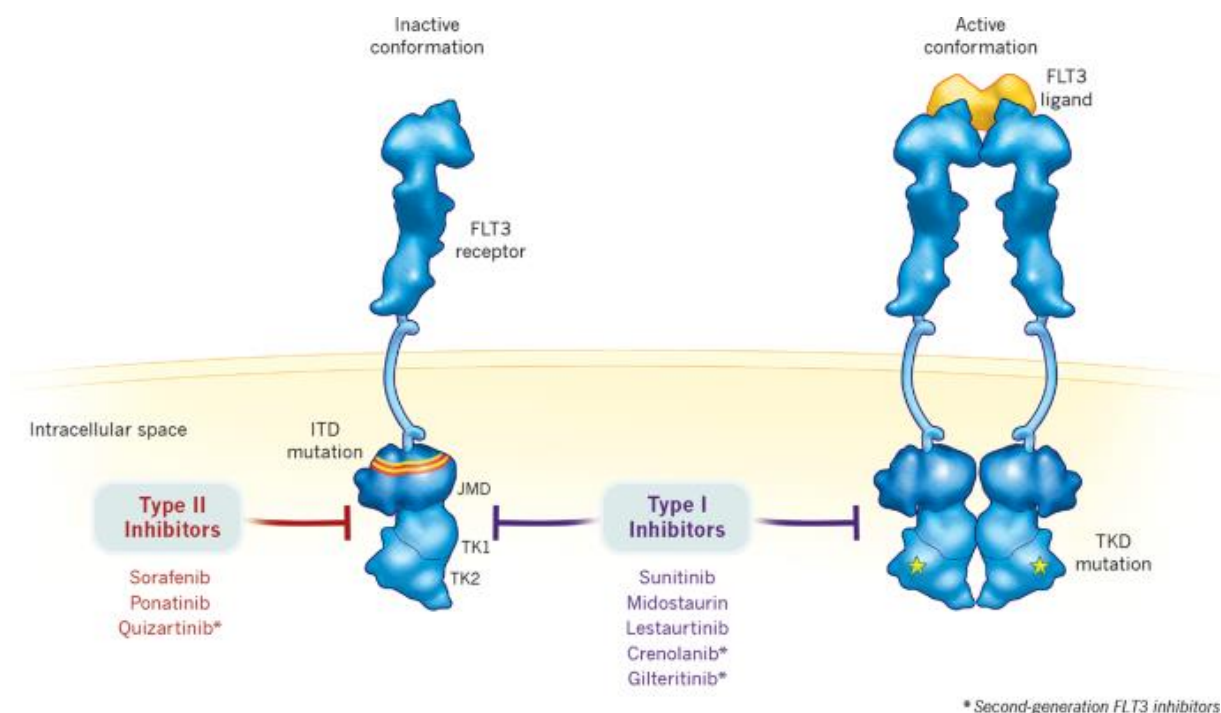


Figure 4 - Scheme of FLT3 activation and different inhibitors preventing signaling. While type I inhibitors bind the FLT3 receptor in the dimeric conformation near the activation loop or the ATP-binding pocket, type II FLT3 inhibitors bind the FLT3 receptor in the inactive, monomeric conformation in a region adjacent to the ATP-binding domain. This results in type II FLT3 inhibitors preventing activity of ITD mutations but they do not target TKD mutations. Copyright permission was granted by nature (Daver et al. 2019).

Due to the high overlap between processes and signaling of AML and hematopoietic stem cells, therapeutic options stagnated until very recently. Nowadays, different pathway inhibitors are used depending on the underlying mutation (Figure 4), for example midostaurin, a FLT3 inhibitor or venetoclax, a BCL-2 inhibitor (Carter et al. 2020).

Due to these novel individual treatments, the survival rates drastically increased showing the high benefit of personalized immunotherapy.

1.6 Microscopy

1.6.1 Fluorescence microscopy

In 1676 Antonie van Leeuwenhoek, achieved one of the biggest breakthroughs for today's microscopy by creating lenses with a magnification sufficient to visualize small organisms, like bacteria, for the very first time. This simple microscope only consisted of a single lens and was further improved in the late 19th and early 20th century (Kriss and Kriss 1998). Nowadays, light microscopy is a widely used biological tool, which nonetheless suffers from poor contrast and optical resolution being limited to ~600 nm.

Discovery of fluorescence in the 19th century, but also of the green fluorescent protein (GFP) expressed in *Aequorea victoria* in 1962 paved the way for first fluorescent visualizations of subcellular structures with superior contrast due to the high signal-to-noise ratio (Shimomura 2009). Nowadays, fluorescence microscopy is the most common and versatile tool in biotechnology with countless different fluorescent proteins, synthetic dyes or labeling strategies available, allowing multicolor detection of the structures of interest.

Aleksander Jabłoński sought to explain this fluorescence by describing different electronic states of molecules and the transition between them. In his so-called “Jablonski diagram” (Figure 5) the photo physical radiation processes during photon absorption of a molecule are described, and an explanation of fluorescence and phosphorescence is given.

All fluorescent molecules share the basic requirement of having delocalized π -electron-systems and possess electrons being in the ground state S_0 . When those electrons are excited with light of appropriate wavelength, the energetically higher singlet states S_1 or S_2 can be reached if the amount of the absorbed energy is at least as big as the energy difference. Absorption is a very fast process occurring in the order of 10^{-15} seconds. After excitation the electron dissipates part of its energy via vibrational relaxation or by internal conversion. From here the electron may fall back to one of the sublevels of the ground state, emitting a photon with energy equivalent to the transition. This process, called fluorescence, takes place in the order of 10^{-9} - 10^{-8} seconds. Because of the loss of energy due to internal conversion and vibrational relaxation, the emitted photon has less energy and therefore a longer wavelength compared to the absorbed photon. This phenomenon was first described 1852 by George Gabriel Stokes and is known as the “Stokes shift”, which makes it possible to use optical filters to separate excitation and emission light to gather high contrast images. Besides fluorescence, some of the excited molecules might also transit to the triplet state T_1 by radiation-less intersystem crossing. From the triplet state T_1 the electrons can recover to the ground state by emitting phosphorescence. Due to the competition for the relaxation process not every absorbed photon will result in the emission of fluorescence. The amount of absorbed photons that actually lead to the emission of fluorescence is described as the quantum efficiency and is a criterion for the brightness of the fluorescent molecule. Therefore, a high quantum yield indicates

a bright fluorescence. For today's microscopy a broad range of numerous dyes, particles and proteins is available, covering not only the whole visible spectrum, but also the ultraviolet and infrared region. All of these tools have been further improved to achieve maximum stability and a high quantum yield (Lakowicz 2013; Sanderson et al. 2014).

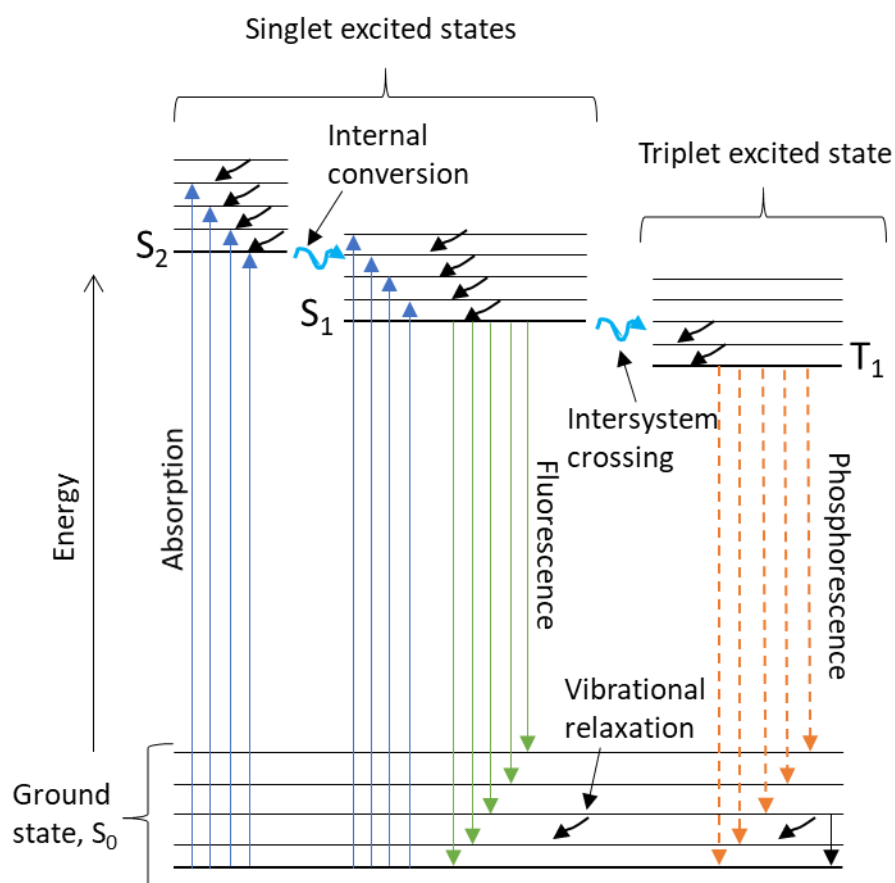


Figure 5 - Jablonski energy diagram introducing the different energy states after absorption of photons. Valence electrons of a fluorophore are excited from the ground state S_0 onto the energetically higher states S_1 and S_2 . Due to vibrational relaxation or internal conversion some energy dissipates, before emitting fluorescence while falling back into the ground state S_0 . This loss of energy causes a shift toward longer wavelengths for the emitted light, known as Stokes shift. Via intersystem crossing some excited electrons can also enter a triplet state T_1 before falling back to the ground state S_0 , thereby emitting phosphorescence.

Even though fluorescence microscopy is ideal to study cellular structures and processes in a non-invasive manner, the diffraction of light is a huge drawback for the usability of fluorescence for the detection of small molecules. This limitation is caused by the physical diffraction property due to the wave nature of light and was first described by Ernst Abbe in 1873 (Patterson 2009). Abbe stated that the resolution of

an optical system (d) for two lines of an optical grid is depending on the emitted light (λ) and the numerical aperture (NA) of the objective (Abbe 1873).

$$d = \frac{\lambda}{2NA} \quad (1)$$

However, due to the characteristic of light being a wave and a particle at the same time a fluorescent spot can be described as a point-like light source, with one main and several side maxima, a so-called airy pattern. In 1896, Lord Rayleigh further addressed the question of diffraction in light microscopy and brought two self-emitting spots in such a proximity until the airy disks of both spots overlapped, making a separation impossible (Figure 6). He stated that two adjacent spots can only be resolved if the maximum of one airy disk coincides with the minimum of first order of the second airy disk (Etoh et al. 2017). This minimal resolvable distance can be described as:

$$d = \frac{0.61\lambda}{NA} \quad (2)$$

In fluorescence microscopy we are therefore able to get a lateral resolution of around half the wavelength of the emitted light, which is limited to 200 nm for conventional microscopy methods, due to optical but also visible light limitations.

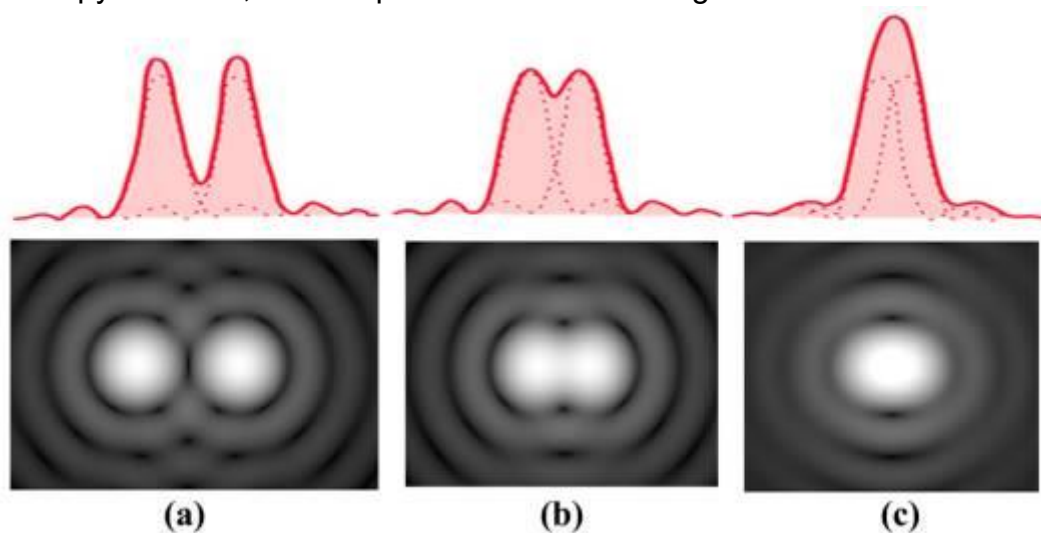


Figure 6 - Diffraction limit of two self-emitting spots and their intensity profile. A) Both spots are far enough away to be well separated. B) The maximum of one spot lies at minimum first order of the other spot, therefore they can be barely detected as two unique spots (Rayleigh Criterion) C) Both spots are too close to each other and can't be separated. Copyright permission was granted from Etoh et al. 2017.

1.6.2 Confocal laser scanning microscopy

One of the most widely used types of fluorescence microscopes are confocal laser scanning microscopes (CLSM), a special sort of light microscope, used to get sharper images of the exact plane of focus. In contrast to a widefield microscope, where the whole specimen is illuminated, a confocal microscope illuminates only small parts of the specimen in the focal plane. Therefore, only the fluorescence in focus can be observed without out-of-focus background fluorescence. This is achieved by a laser focused onto a defined spot at a certain depth within the specimen. The emitted light is reflected from the focal plane as well as from the area below and can pass through a dichroic mirror due to its longer wavelength. The tube lens focuses the light beam through a pinhole onto the detector (e.g. a CCD-camera). Due to the pinhole, only the light beam originating from the focal plane can pass through and hit the detector converting the fluorescent light into an electric signal. This also reduces background noise which allows for obtaining a better resolution of the specimen. However, the pinhole cannot be chosen randomly small, because this results in a loss of brightness and underlying information.

1.6.3 Super-resolution microscopy techniques

For a long time, the diffraction limit of light was an inevitable barrier limiting light microscopy to a resolution of ~200 nm, making it impossible to study small cellular components. However, during the last two decades new fluorescent microscopy techniques like structured illumination microscopy (SIM) (Wu and Shroff 2019), stimulated emission depletion (STED) (Vicidomini, Bianchini, and Diaspro 2018), PALM (Photoactivated localization microscopy) STORM (stochastic optical reconstruction microscopy) (Rust, Bates, and Zhuang 2006) and *direct* stochastic optical reconstruction microscopy (*d*STORM) (Heilemann et al. 2009) arose, overcoming limitations of optical microscopy and improving resolution. These super-resolution microscopy methods rely on different physical principles having their advantages and disadvantages at the same time (Feng et al. 2018).

SIM microscopy makes use of non-uniform excitation light patterns created by a grid resulting in moire effect interference patterns. By deconvolution of the interference signal with specialized software, a twofold resolution improvement up to ~120 nm is possible. Even though the maximal obtained resolution is inferior compared to other

super-resolution techniques, live cell, multi-color and 3D-data can be gathered in a rather short time period (Wu and Shroff 2019).

A different approach is STED microscopy which uses pairs of synchronized laser pulses. A first laser pulse excites the dye, while the second doughnut shaped laser pulse is used to deplete emission from the area. Due to its shape, only the fluorescence from the center of the doughnut remains unaffected and can be detected by single photon sensitive detectors. When using appropriate dyes, a lateral resolution up of to 30 nm can be achieved (Blom and Widengren 2017).

PALM makes use of specific photoactivatable fluorescent proteins like mEOS, which are spontaneously activated upon irradiation with a short laser pulse of the right wavelength. A stack of images is recorded until all proteins were activated and photo bleached or destroyed (Lee et al. 2012). However, due to its long acquisition time and the low brightness of fluorescent proteins the resolution is lower compared to *d*STORM.

*d*STORM follows the same principle, however, instead of using fluorescent proteins bright photoswitching dyes like carbocyanine fluorophores, rhodamine fluorophores or oxazine fluorophores are used. To obtain a high resolution image, no adjacent fluorophores are allowed to overlap in their emission. Therefore, it is important to have most of the dyes in a long-lived non-fluorescent off state (Figure 7 B). To transfer photoswitching dyes into this off state, high laser powers as well as reducing agents like thiols are essential. When illuminating the dye with a laser with appropriate wavelength, the dye is transferred into the excited state F_1 from which it can fall back into the ground state, F_0 emitting fluorescence (Figure 7 C). However, a small subset of those dyes can spontaneously enter the spin-forbidden triplet state 3F by intersystem crossing with a specific rate K . By increasing the laser power most of the dyes stochastically enter the triplet state. From this state the fluorophore either can fall back into the ground state by reacting with molecular oxygen or be reduced by agents like primary thiols. This reaction creates a fluorophore radical anion F^* that is less reactive to molecular oxygen compared to the thiolate molecule, making it very stable. Due to this, an off state that can last several milliseconds to seconds, is created. Additionally, some dyes like ATTO 655 can be even further reduced into its leucoform. Spontaneous reaction with oxygen brings the fluorophore back to the ground state before it can be excited again and re-enter the cycle (Heilemann et al. 2009; van de Linde et al. 2011).

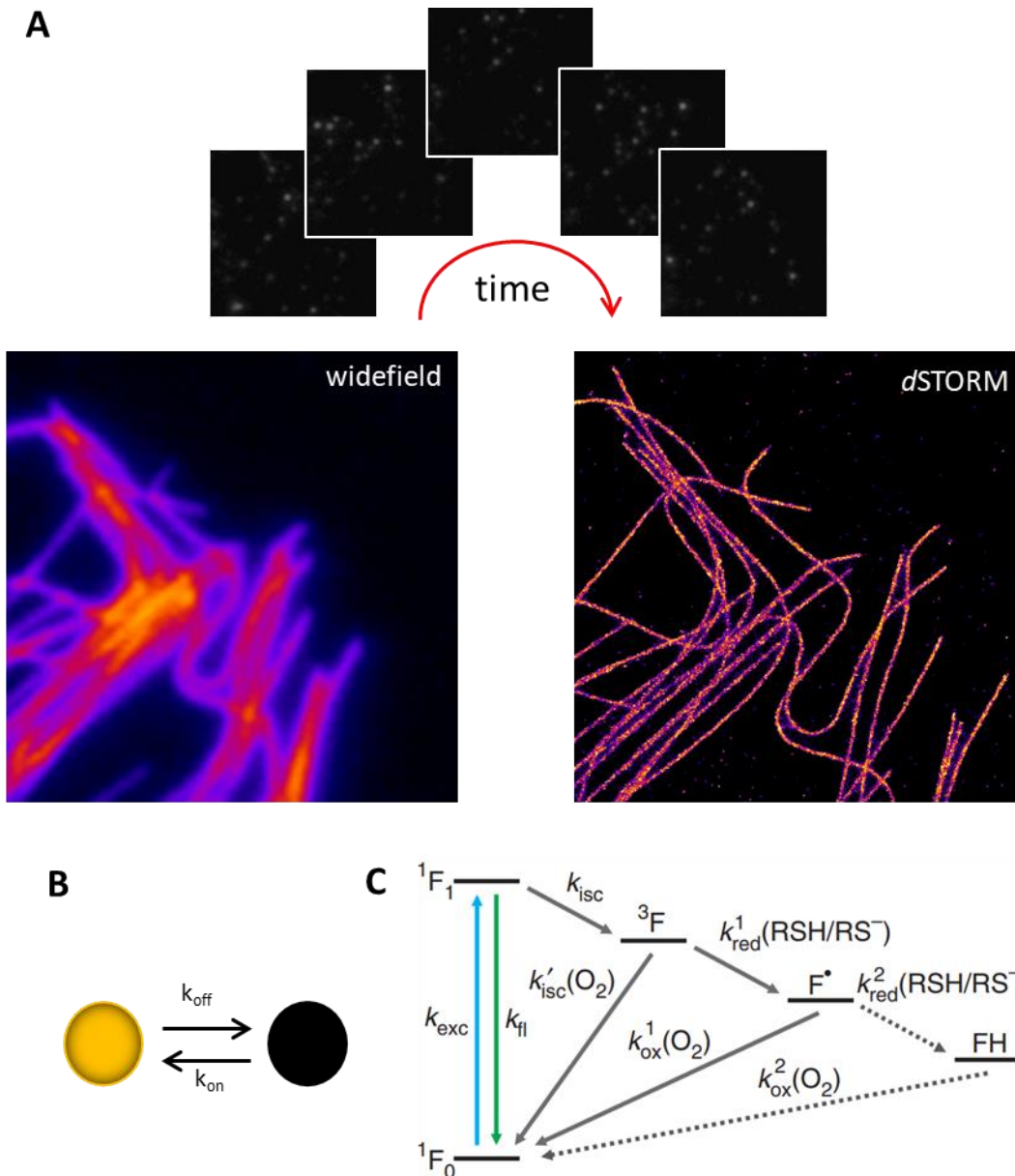


Figure 7 - Working principle of *d*STORM. A) By adding thiol containing switching buffer and use of appropriate laser powers most of the switchable dyes will enter a long-lived non-fluorescent dark state. Acquisition of several thousands of diffraction limited widefield images with separated fluorescent spots lead to a highly resolved *d*STORM image when reconstructed with rapid*d*STORM. B) The on-off ratio k_{on} to k_{off} of a fluorophore depends on the chemical environment and the used laser power. C) Chemical principle of *d*STORM: Reversible photoswitching is enabled by dyes cycling between the ground state F_0 and F_1 while some few spontaneously enter the triplet state 3F . Dyes in the triplet state either interact with molecular oxygen to recover to the ground state or react with the thiols in the switching buffer to form a very stable fluorophore radical anion (F^*). From this state the ground state can again be recovered by reacting with molecular oxygen. Certain fluorophores such as ATTO 655 also accept a second electron to form the fully reduced leuco-form (FH) that can also react with molecular oxygen to get back into the ground state. For part C copyright permission has been granted by Springer Nature (van de Linde et al. 2011).

Generally, each of those fluorophores is detected several times before being bleached. Afterwards, each of these localizations positions can be determined with different available software using two-dimensional Gaussian fits resulting in a lateral resolution of up to 10-20 nm (Figure 7 A).

1.6.4 Quantification and analysis of SMLM data using Clustering algorithms

Localization-based approaches allow a precise quantification of the underlying signal and are helpful to detect oligomerization or clustering processes above 10-20 nm. To date, several clustering algorithms are available that are suited for single molecule localization microscopy techniques. Although many algorithms are biased towards circular clusters, arbitrary shapes are more common in biological systems. Therefore in 1996, Ester et al. introduced a “**Density Based Spatial Clustering of Applications with Noise**” (**DBSCAN**) algorithm needing only two user defined input parameters, the maximal distance ϵ between two points for grouping and the minimal amount of points (MinPts), to define a true cluster and discard noise (Ester et al. 1996; Khater, Nabi, and Hamarneh 2020).

The underlying principle is visualized in Figure 8 A. The algorithm selects a random starting point and if enough points are in the defined vicinity, a cluster is build up. This propagates until no more points are in the proximity of the defining border points (BP) of this cluster. Clusters not fulfilling the minimal amount of points within the defined distance are declared as noise (N) and are excluded. In addition, clusters can vary in their shape and amount of points as visualized in Figure 8 B.

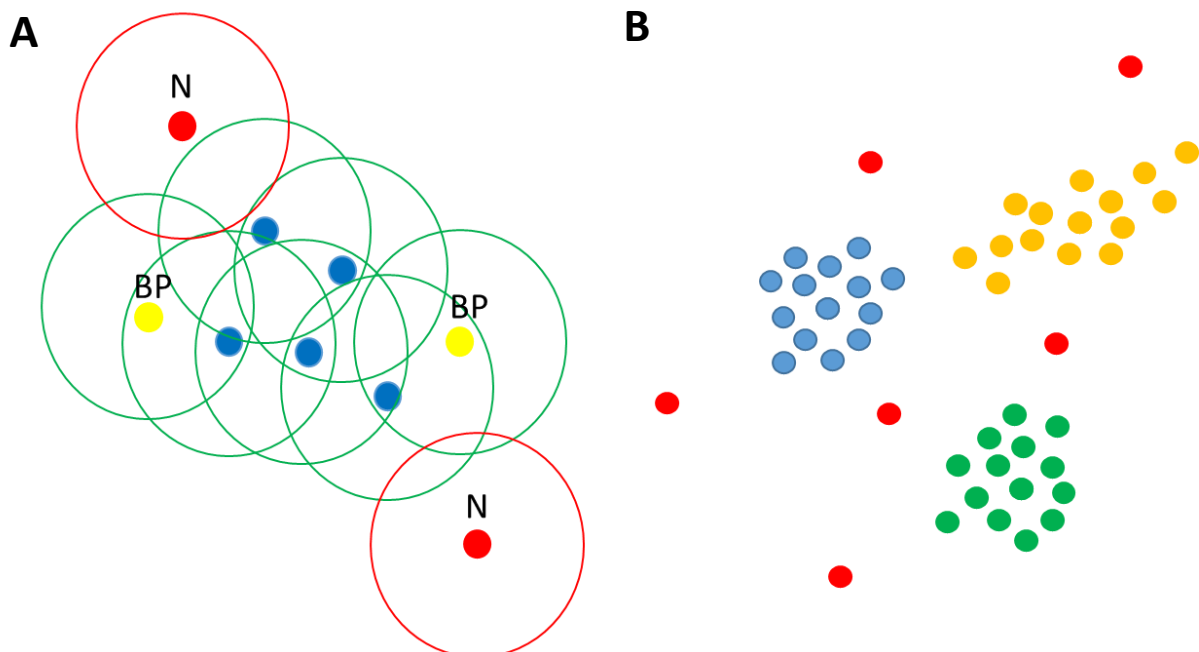


Figure 8 - Principle of cluster analyzes with DBSCAN. A: Points are joined up as long as the maximal distance ϵ (depicted as green circles) is compiled to. The border points (BP) are still included into the cluster, even though they are only reachable by one point. The red points are laying within the defined diameter and therefore do not fulfill the minimal point criterion and are excluded. B: Different cluster shapes that fulfill the parameters shown in blue, green and yellow. Red spots between these clusters are defined as noise points as they are not reachable with the predefined parameters.

Besides DBSCAN, Ripley's h , k and I functions are widely used to describe aggregation of proteins (Figure 9 B). With these, the amount of proteins present within a certain distance r is compared to protein densities expected for a random distribution (gray dotted line Figure 9 B) to decide whether aggregation of microclusters is present or not (Kiskowski, Hancock, and Kenworthy 2009; Wilschut et al. 2015). It is however thought that microclusters of proteins are typically present as a small subset in a background of monomers on the cell membrane (Sharma et al. 2004).

Ripley's k functions are able to detect deviations from spatial homogeneous populations such as dispersed clustered events. Additionally, the linearized k -function, Ripley's I -function, can be normalized yielding to the h -function. The h -function is commonly used for experimental data indicating clustering if $h(r) > 0$, a disperse distribution if $h(r) < 0$ and a stochastically uniform distribution if $h(r) = 0$. The maximum positive value of $h(r)$ indicates an approximation of the average size of spatial patterns like clusters within the analyzed ROI (Shivanandan, Unnikrishnan, and Radenovic 2016).

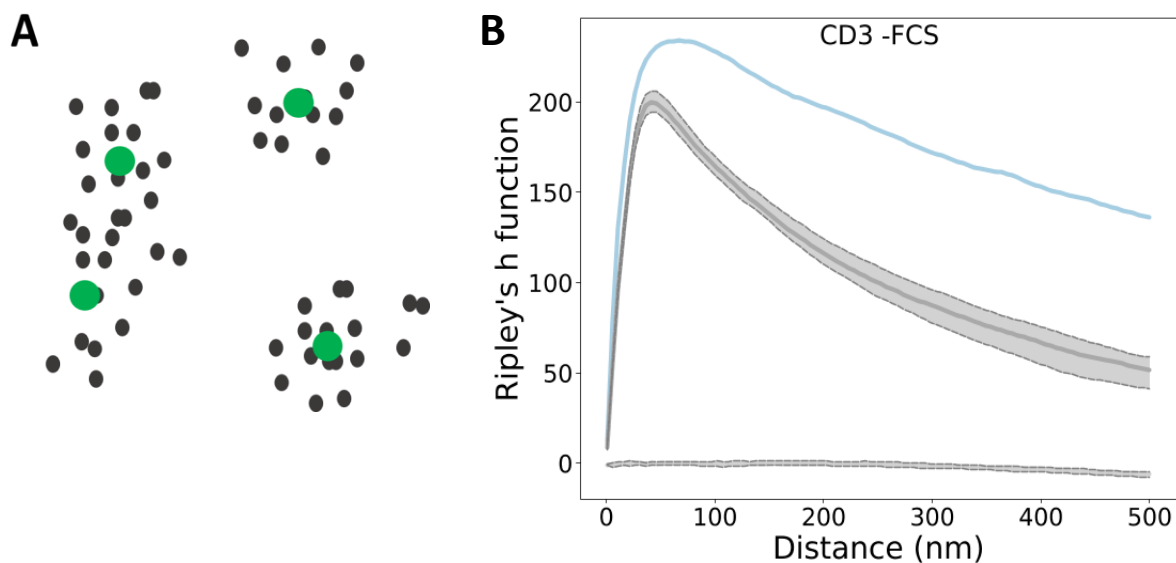


Figure 9 - Neyman–Scott distribution (A) and a representative Ripley's h -function (B) of CD3 receptors detected by a monoclonal antibody on Jurkat T cells. Due to photoswitching, fluorophore-coupled proteins are observed multiple times (black dots) and a center of mass (green dots) needs to be found for each fluorophore. Simulation of a homogeneous distribution (Completely spatial randomness) of fluorophores for the h -function (B), is shown as lower gray line with its corresponding confidence interval (dotted gray lines), while the homogeneous distribution for multiple blinking events is taken into account for the upper gray line, known as Neyman-Scott-process. The amplitude of the experimental data (blue line) is compared to the gray line to see if r_{\max} changed, indicating in this case protein aggregations with a cluster size of ~ 60 nm.

However, due to the stochastic photoswitching during *d*STORM image acquisition, multiple localization events need to be taken into account for one single protein and are described best as a Neyman-Scott distribution for random point processes when proteins are homogeneously distributed (Figure 9 B, upper gray curve) and can be compared with experimental generated data (Figure 9 B, blue curve) (Yau and Loh 2012). Typically, the observed blinking events (Figure 9 A, gray dots) differ from the latent events, being the center of mass (Figure 9 A, green spots).

However, because Ripley's h-function averages all detected clusters within a ROI it might not be suited for strong heterogeneity within a population. Also small changes in the range of a few nanometers are not detected.

1.7 Objective of this work

Within this work the super-resolution microscopy method *d*STORM was used to visualize membrane receptors and to establish a working protocol to differentiate between different oligomeric receptors. For this, the Jurkat T cell line was used and antigens with known stoichiometry were investigated according to their localization statistics. This protocol was later on applied to quantify and visualize receptors on two clinically relevant examples. One was FLT3, a tyrosine-kinase, targeted by inhibitors to treat acute myeloid leukemia. The second clinical example was the multiple myeloma. Here different relevant receptors like CD19, CD20, CD38, CD138, BCMA and SLAMF7 were imaged and quantified. Additionally, the influence of gene mutations on receptor expressions were investigated by using the myeloma cell lines OPM2 and AMO1. Main aim of this work is to enable the quantification and detection of receptor aggregations for personalized immunotherapy helping to identify risk factors or important novel targets.

2 Material and Methods

2.1 Cell culture

Quantification of plasma membrane receptors was done for various cell lines like Jurkat E6-1, Raji, MM.1S, MV4-11, MOLM-13, COS-7, but also for primary blood cells like T cells, multiple myeloma cells and white blood cells. Jurkat E6-1, Raji, MM.1S, MV4-11, MOLM-13 were cultured in RPMI1640 (Sigma, R8758) supplied with 10% FCS (Sigma, F7524) and 100 U/ml penicillin and 0.1 mg/ml streptomycin (Sigma, P4333) at 37°C and 5% CO₂, whereas COS-7 cells were cultured under same conditions in DMEM Ham's F12 (Sigma, D8062) with the same supplements. Cell splitting was carried out according to the recommendation of the ATCC, but latest when the cells became confluent enough. Cultivation of the adherent cell lines was done by the technical assistance of our department. Primary mouse Treg cell isolation was performed by Dr. Julia Delgado-Tascon from the Department of Medicine II & Pediatrics whereas primary multiple myeloma cells (Table 2) were provided by Prof. Dr. med. Martin Kortüm (Department of Medical Clinic and Polyclinic II) and primary AML cells by Dr. Sabrina Kraus (Center for allogeneic stem cell therapy).

Table 1 - List of used cell lines, their cell types and origin.

Cell line	Type	Disease
Jurkat E6-1	T cells	acute T cell leukemia
Raji	B cells	Burkitt's lymphoma
MM.1S	B Lymphoblast	immunoglobulin A lambda myeloma
MV4-11	Macrophages	biphenotypic B myelomonocytic leukemia
MOLM-13	Macrophages	acute myeloid leukemia
COS-7	SV40 transformed	

Table 2 - Multiple myeloma patients, their applied treatment and underlying genetically mutations.

Patients	Treatment with Daratumumab	Other treatments	Mutations
Pat225	Yes, progressive (2021)	/	/
Pat379	Yes, responding	1x DaraVTD with response, then Daratumumab, Revlimid, Bortezomib, Doxorubicin, Dexamethason	not high risk t(11;14)
Pat394	Yes, progressive (2019)	Belantamab	high risk, gain (1q) t(14;20) or t(14;16)

2.2 Cell thawing and plating

Cryopreserved primary samples were thawed in a water bath at 37°C for 1-2 minutes until only some ice crystals were left and transferred into a 15 ml centrifuge tube filled with 10 ml pre-warmed cell media. The tube was centrifuged at room temperature for 6 min at 1610 rpm, the supernatant removed and the cell pellet resuspended in 10 ml fresh pre-warmed cell media. On the next day, the vital cell number was determined by a hemocytometer and a total amount of 2×10^5 cells were plated onto PDL or antibody coated Lab-Teks.

2.3 Antibody labeling

For the conjugation of different dyes to proteins like an antibody a buffer exchange to 100 mM sodium bicarbonate (NaHCO_3) (pH8.3) in 1x phosphate-buffered saline (PBS) (Sigma, D1408) was necessary to have optimal conditions for the NHS-reaction to take place. For this 300 μl of NaHCO_3 (Fisherscientific, S/4240/60) were given into 0.5 ml 7 or 40 kDa Spin desalting columns (Thermo Fischer, 87767), centrifuged by 1000x g for 1 minute, the suspension discarded and the procedure repeated two additional times. Afterwards, 100 μl solution containing between 25-50 μg antibody were run through the columns at 1000x g for 2 minutes before the *N*-Hydroxysuccinimide (NHS)-dye was added in a 10 fold molar excess. After incubation for 3 h in the dark at room temperature, the columns were equilibrated like before with 1x PBS supplemented with

0.02% Sodium azide (NaN_3) (Sigma, S-8032), before the antibody-dye solution was added. By this step, unreacted NHS-dye was removed and the antibody concentration and degree of labeling (DOL) was determined by using a UV-vis spectrophotometer (Jasco V-650) and the following formula:

$$\text{Protein concentration (M)} = \frac{A_{280} - (A_{\text{max}} \times \text{CF})}{\epsilon} \times \text{dilution factor} \quad (3)$$

$$\text{Degree of labeling (DOL)} = \frac{A_{\text{max}}}{\epsilon' \times \text{protein concentration (M)}} \times \text{dilution factor} \quad (4)$$

A_{280} = Absorbance at 280 nm

A_{max} = Absorbance of the dye solution measured at the wavelength maximum

CF = Correction factor; adjusts for the amount of absorbance at 280 nm caused by the dye

ϵ = Molar extinction coefficient of the protein

ϵ' = Molar extinction coefficient of the fluorescent dye

Dilution factor = The extent to which the protein:dye sample was diluted for absorbance image.

For all experiments, the DOL of the antibodies/ligands ranged from 2-4 to ensure at least one dye per protein and to avoid unspecific binding events caused by too many dyes attached to the proteins.

Table 3 - List of used dyes for protein labeling and their correction factor and extinction coefficients.

Dye	Correction Factor (CF)	Extinction coefficient ϵ	Company (Catalog number)
AF532-NHS	0.09	81,000	Thermo Fisher (A20101)
AF647-NHS	0.03	239,000	Thermo Fisher (A20006)
Cy5B-NHS	0.55	210,000	Martin Schnermann (Laboratory of Chemical Biology)

2.4 Live cell staining

Visualization of membrane receptors was achieved by seeding 2×10^5 suspension cells into pre-coated eight-well chambers (Lab-Tek II, Nunc, Thermo Fisher Scientific or Cellvis C8-1.5H-N). For the poly-D-lysine (PDL) (Sigma, P6407) coating, the chambers were cleaned by using 1 M potassium hydroxide (KOH) (Sigma, 06203) for 10 min, washed two times with ddH₂O and incubated with 100% ethanol (EtOH) (Sigma, 32221) for 20 min. After the EtOH had been removed and the chambers were air dried under the clean bench 150 μ l PDL was added for 1 h in a concentration of 0.1 mg/ml. The PDL was removed from the wells and washed once with 1x PBS before being air dried.

Antibody coating was done by adding 5-10 μ g/ml in 1x PBS of the required antibody on the pre-cleaned surface for 2 h at 37°C before being washed one time with 1x PBS. After the cells had successfully attached to the glass surface, they were stored at room temperature for 5 minutes before being transferred on ice for a further 5 minutes. Afterwards, the media was removed and replaced by the ice-cold antibody solution, containing 0.5-20 μ g/ml of the desired antibody in 1x PBS for 30-60 min. The cells were washed three times with ice-cold 1x PBS before the fixative containing 2% formaldehyde (FA) (Sigma Aldrich, F8775) and 0.25% glutaraldehyde (GA) (EMSDiasum, 16220) was added for 15 minutes at room temperature. The cells were washed additional three times with 1x PBS and stored at 4°C in the dark until imaging. For some plasma membrane receptors staining had to be performed at 37°C.

2.5 Fixed cell staining

20,000 COS-7 cells were seeded on non-coated eight well Lab-Tek chambers (Lab-Tek II, Nunc, Thermo Fisher Scientific) and allowed to grow overnight at 37°C at 5 % CO₂. As a first step cells were fixed with 0.3% GA + 0.25% TritonX-100 (Thermo Fisher, 28314) in cytoskeleton buffer (CB) (10 mM MES, 150 mM NaCl, 5 mM EGTA, 5 mM Glucose, 5 mM MgCl₂, pH 6,1) for 1-2 minutes at 37°C. The suspension was removed and replaced by 2% GA in CB buffer for 10 minutes at room temperature. After removing the fixative the sample was washed three times with 1x PBS, followed by background reduction with 0.1% sodium borohydride (NaBH₄) (Sigma, 71320) for seven minutes. Additional three washing steps with 1x PBS were followed by 30 minutes incubation of 5% bovine serum albumin (BSA) (Carl Roth, 3737-3) in ddH₂O

(Blocking solution) to reduce unspecific binding. The primary antibody was added in the required concentration for 1 h followed by three washing steps with blocking solution. If needed, a secondary antibody was added for additional 45 minutes followed by three washing steps. To ensure longer storage the sample was postfixed with 4% FA for 10 min and washed three times with 1x PBS before stored at 4°C in the dark.

Table 4 - List of used primary antibodies.

Antibody	Clone	Host	Conjugate	Used Concentration	Company
Anti-CD2	TS1/8	mouse	Alexa Fluor 647	5 µg/ml	Biolegend
Anti-CD3	UCHT1	mouse		5 µg/ml	Biolegend
Anti-CD11a	HI111	mouse		2 µg/ml	Biolegend
Anti-CD11a (active)	mab24	mouse		5 µg/ml	Biolegend
Anti-CD18	TS1/18	mouse		5 µg/ml	Biolegend
Anti-CD28	CD28.2	mouse		5 µg/ml	Biolegend
Anti-CD34	581	mouse		2 µg/ml	Biolegend
Anti-CD38	HIT2	mouse	Alexa Fluor 647	7.5 µg/ml	Biolegend
Anti-CD38 (Multiepitope)	ME-CD38	rabbit		5 µg/ml	Cytognos
Anti-CD45	2D1, HI30	mouse		5 µg/ml	Biolegend
Anti-CD69	FN50	mouse		2 µg/ml	Biolegend
Anti-CD135	BV10A4H2	mouse		2 µg/ml	Biolegend
Anti-CD135	A2F10	mouse	Alexa Fluor 647	2 µg/ml	eBioscience
Anti-CD138	MI15	mouse		5 µg/ml	Biolegend
Anti-α-tubulin	ab15246	rabbit		2 µg/ml	abcam
IgG2a, κ Isotype Ctrl	MG2a-53	rat		5 µg/ml	Biolegend
IgG2b, κ Isotype Ctrl	MPC-11	rat		5 µg/ml	Biolegend

Table 5 - List of used primary antibodies for regulatory T cell staining.

Antibody	Clone	Host	Conjugate	Used Concentration	Company
Anti-CD3	17A2	rat	/	5 µg/ml	Biolegend
Anti-CD4	GK1.5	rat	/	5 µg/ml	Biolegend
Anti-CD25	7D4	rat	/	5 µg/ml	Biolegend
Anti-CD103	2E7	rat	/	5 µg/ml	Biolegend
Anti-CD120b	TR75-54	armenian hamster	/	5 µg/ml	ebioscience
Anti-CD134	OX86	rat	/	2 µg/ml	Biolegend
Anti-CD137	17B5	rat	/	2 µg/ml	Biolegend
Anti-CD279	RMP1-30	rat	/	2 µg/ml	Biolegend
Anti-DR3	4C12	rat		2 µg/ml	Biolegend
Anti-GARP	7B11	rat		2 µg/ml	Biolegend
Anti-GITR	5F1	rat		7.5 µg/ml	Biolegend

Table 6 - List of used secondary antibodies.

Antibody	Host	Conjugate	Company
Anti-rabbit	goat	Alexa Fluor 647	Thermo Fisher (A21246)
Anti-mouse	goat	Alexa Fluor 647	Thermo Fisher (A21237)
Anti-rabbit	goat	Alexa Fluor 532	Thermo Fisher (A111009)
Anti-mouse	goat	Alexa Fluor 532	Thermo Fisher (A11002)
Anti-rabbit	goat	/	Invitrogen (31212)
Anti-mouse	goat	/	Sigma (SAB3701063)

2.6 Imaging

2.6.1 Confocal Laser Scanning Microscope (CLSM)

All confocal images were taken on a “LSM 700 Confocal Microscope” by Zeiss installed on a vibration-cushioned table to reduce drift of the sample. The setup is equipped with a standard objective (EC Plan-Neofluar 10x 0.3 NA, Zeiss) and an oil immersion

objective (PlanApochromat 63x 1.40 NA, Zeiss). The setup contains a 5 mW red laser (637 nm), a 5 mW green laser (555 nm) and a 10 mW blue laser (488nm). An URGB beamsplitter (405, 488, 555 and 639 nm) separates the emitting light from the excitation light and additional filters allow removing of external emission light send out by other wavelengths. The setup also can carry out multicolor imaging by using two confocal channels each with an own photomultiplier detector. All images were gathered by using 5% laser power with a pixel dwell time of 11.1 μ s, one airy unit, optimal pixel size and an additional gain of 650.

2.6.2 One-color dSTORM

dSTORM imaging was carried out on a homebuilt widefield setup with an inverted microscope (Olympus IX-71) using an oil immersion objective (Olympus APON 60xO TIRF, NA 1.49). The setup is equipped with excitation lasers of the wavelengths 639 nm (Genesis MX639-1000, Coherent), 558 (Genesis MX561-500, Coherent) and 514 nm (Genesis MX514-500, Coherent). To separate the excitation beam from the fluorescence, a dichroic beam splitter was used (either ZT405/514/635rpc, Chroma or FF410/504/582/669, Chroma) and the emission was additionally filtered by emission filters (Brightline HC 679/41 (Semrock), Brightline HC 607/70 (Semrock) or BrightLine HC 582/75 (Semrock) in front of the EMCCD-cameras (iXon Ultra 897, Andor). dSTORM imaging was performed in a switching buffer containing 100 mM β -mercaptoethylamin (Sigma, M6500) at a pH depending on the used dyes (7.4 for AF647, 7.0 for AF532) with integration times of 20 ms for 15,000 frames at laser intensities of \sim 2.5 kW/cm². The basal membrane of the cells were imaged in TIRF-illumination mode (Total internal reflection fluorescence microscopy) to ensure high signal-to-noise measurements. All acquired image stacks were reconstructed with rapidSTORM 3.3 (Wolter et al. 2012).

2.6.3 Preparation of TetraSpeck sample

Glass surface cleaning and coating with PDL was done according to the protocol mentioned in 2.4. The TetraSpecks (Invitrogen, T7279) were diluted 1:100 in 80 mM Pipes buffer (Sigma, P1851) containing 1 mM MgCl₂ and 1 mM EGTA (pH 6.8) before being sonicated for 30 min. Afterwards, the solution was given into the cleaned Lab-Tek well for 1h at room temperature before being washed three times with 1x PBS.

2.6.4 Two-color *d*STORM

Two-color *d*STORM imaging was performed on the same homebuilt widefield setup as described in 2.6.2. First, both channels were pixel precise aligned with a self-made TetraSpeck sample described in 2.6.3. Afterwards, the sample containing the imaging buffer was put on stage and after focusing on the basal layer the setup was left for a certain time until no z-dimensional drift was observed anymore. The image stacks were first acquired from the longer wavelength absorbing dye followed by the shorter wavelength absorbing dye (sequentially). The sample was removed and replaced by the TetraSpeck sample, which was imaged (100 frames with 50 ms exposure time) until at least a few TetraSpecks were located in each corner and in the middle of the camera chip. This workflow was repeated after each two-color image to ensure a high precision of the later created elastic transformation by the Fiji plugin “bUnwarpJ”.

The reconstructed TetraSpeck images were opened in “bUnwarpJ” and manually a landmark in each corner and the middle was set. After this, an elastic transformation was created with these settings:

Table 7 - Settings used for creating an elastic transformation with bUnwarpJ.

Registration Mode	Mono
Initial Deformation	Coarse
Final Deformation:	Fine
Divergence Weight	0.0
Image Weight	0.1
Consistency weight	1.0
Stop Threshold	0.01

The elastic transformation was applied on the respective sample images. Afterwards, a region of interest (ROI) was drawn around the basal layer and the Fiji plugin “Colocalization threshold” determined the Manders overlap coefficient (MOC).

2.6.5 Analysis of *d*STORM data by rapid*d*STORM, Locan and ImageJ

Processing of *d*STORM localization data was done using the open source software rapid*d*STORM 3.3. The pixel size of one input pixel was 128 nm with a PSF FWHM of 360 nm for red absorbing dyes and 131 nm/px with a PSF FWHM of 340 nm for the

green/yellow absorbing dyes. The intensity threshold was set to a minimum of 800 photons to reduce background noise localizations. The pixel size of the final reconstructed image was set to 10 nm/pixel for all three dimensions unless otherwise noted.

The quantification of the plasma membrane receptors was done by using the software Locan. Locan is a custom written python script, programmed by PD Dr. Sören Doose from our department, which uses the localization data of rapidSTORM or ThunderStorm to perform cluster analyses or stoichiometric analyses. First, the localization file was opened with the image viewer “Napari” and the region of interest (ROI), the location of the basal plasma membrane attached to the glass surface, was determined. Afterwards, a DBSCAN algorithm with $\epsilon = 20$ nm and MinPts = 3 was used to determine the amount of clustered single point events on the cell surface. Because antibodies labeled with Alexa Fluor 647 show on average 7-10 blinking events additional receptor estimations could be obtained. The processed data were further imported to OriginPro 2016G and depicted as Box-plots.

3 Results

3.1 Stoichiometric receptor quantification on Jurkat T cells

The following chapter describes the results of experiments on Jurkat T cells used to establish and validate receptor quantification. For this, various receptors with known stoichiometries were used as ground-truth and analyzed using single- and two-color *d*STORM to gather information about epitope accessibility, blinking behavior and artificial clustering in the range of 10-50 nm.

Jurkat T cells were stained on ice with different antibodies according to the live cell staining protocol 2.4 to avoid internalization, before *d*STORM imaging was performed according to 2.6.2 and reconstructed with rapid*d*STORM 3.3. Additionally, fixation occurred as a last step as it is thought to cause crosslinking of accessible epitopes and therefore drastically reducing detection of present receptors. All single-color *d*STORM measurements were performed with self-labeled AF647 primary monoclonal antibodies with a DOL ranging between 2 and 4. Representative *d*STORM images of the basal layer of Jurkat T cells are shown in Figure 10. All antibodies show a quite diverse quantity of detected receptors on the cell surface with CD2 and CD3 being highly abundant, compared to CD11a, CD18, CD45, CD69 and CD105 which are sparsely distributed (Figure 11). Interestingly, even though most of the detected targets demonstrate a homogeneous distribution on the cell surface (Figure 10, red circles), LFA-1, CD69 and CD105 indicate two or three adjacent detected antibodies more often than others do (Figure 10, yellow circles). In comparison, CD3 clearly shows a heterogeneous distribution of single spots and clusters of antibodies in different sizes and shapes. As one single antibody is detected multiple times due to stochastic photoswitching, cluster analysis of the localization data has been performed to group these localizations to its corresponding antibody. To this end, quantitative cluster analyses of localization data with the software Locan and the implemented DBSCAN algorithm with $\epsilon = 20$ nm and MinPts = 3 was done. Using these parameters ensures identification of present fluorophore coupled antibodies and removes background or noise localizations, which only appeared one or two times. For the different receptors strongly varying mean cluster densities (Cluster/ μm^2) \pm standard error (s.e.) ranging from 16.9 ± 3.3 (s.e.) for CD2 (n=7), 15.4 ± 2.1 (s.e.) for CD3 (n=5), 3.0 ± 0.3 (s.e.) for CD11a (n=13), 3.9 ± 0.4 (s.e.) for CD18 (n=20), 5.2 ± 0.4 (s.e.) for LFA-1 (n=18),

4.4 ± 0.4 (s.e.) for CD45 (n=14), 5.2 ± 0.4 (s.e.) for CD69 (n=27) and 3.0 ± 1.1 (s.e.) for CD105 (n=6) were observed (Figure 11).

Note that “cluster densities” refers to clustering of single localizations observed from multiple blinking events of a single antibody and not a clustering of receptors in this case. Therefore, for monoclonal antibodies, the cluster density is equal to the receptor density only for monomeric receptors, that do not form clusters, whereas for dimers or clustering receptors (e.g. CD3), receptor densities have to be estimated by the number of detected localizations divided by the localizations given from a single antibody. This

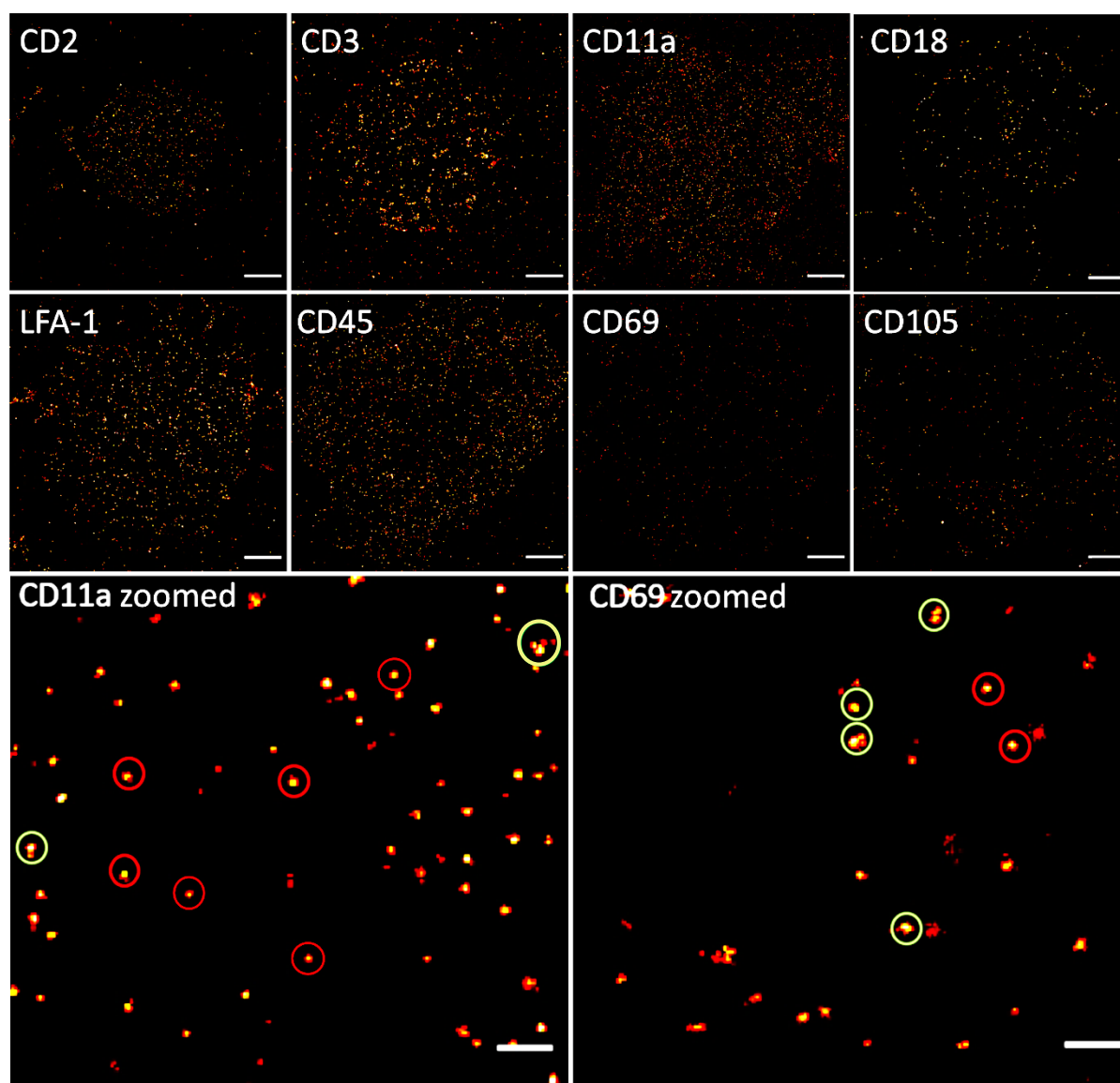


Figure 10 - Representative dSTORM images of the basal membrane of Jurkat T cells labeled with different Alexa Fluor 647 conjugated antibodies. Cells were stained on ice and fixed afterwards. While most of the different detected receptors show a rather homogeneous distribution on the cell surface, cluster formation is clearly visible for CD3. Additionally, some of the receptors (e.g. CD69) seem to form - besides monomers (red circles) - small oligomers visible by two adjacent antibodies (yellow circles) more often than others do (e.g. CD11a). Scale bars: 2 μ m; CD11a and CD69 zoomed: 200 nm.

value has to be identified first by determining localizations per cluster for monomeric receptors. All cluster densities (cluster/ μm^2) are shown in Figure 11 with each boxplot representing an individual detected receptor by the antibody and each point within the plot representing a single analyzed cell.

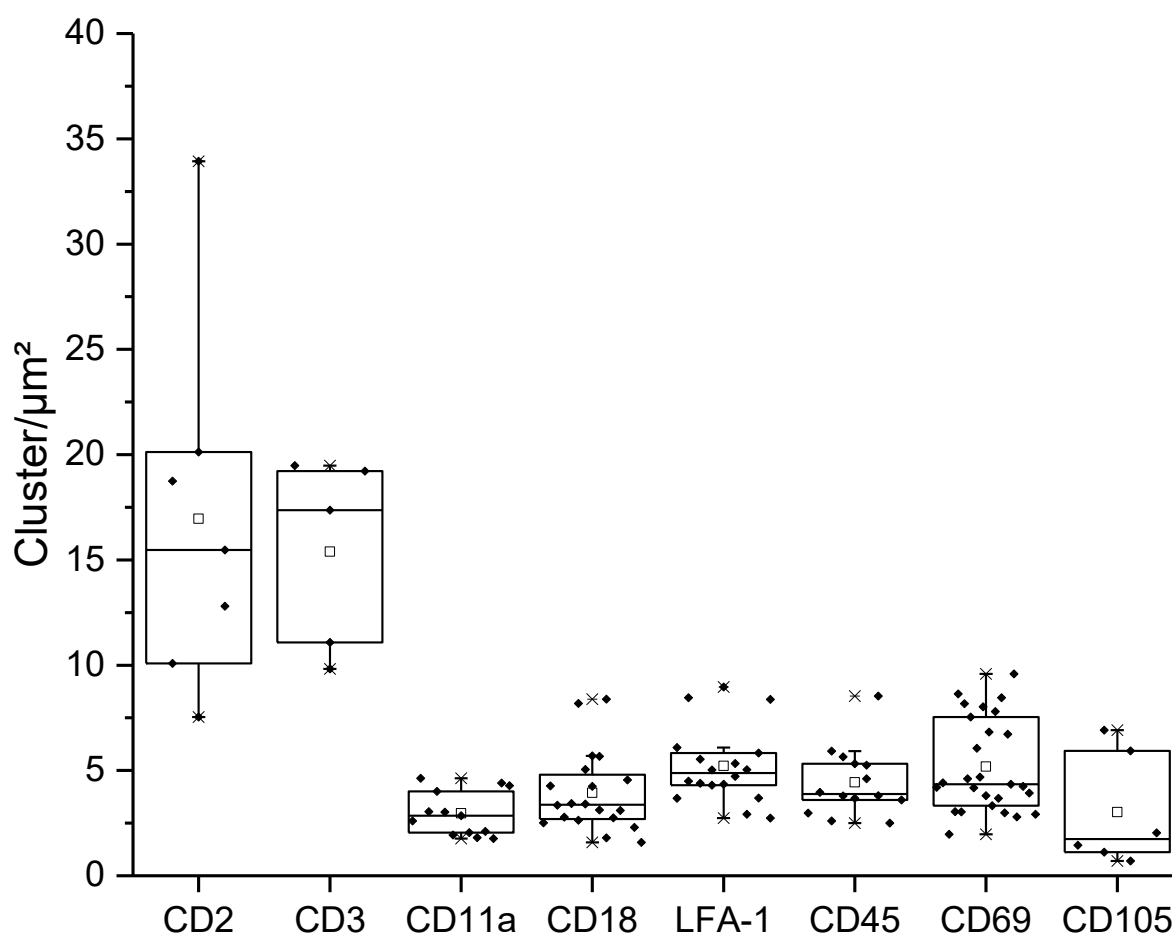


Figure 11 - Cluster densities of different detected receptors on the basal membrane of Jurkat T cells. Cells were analyzed using the implemented DBSCAN algorithm of Locan with $\epsilon = 20$ nm and $\text{MinPts} = 3$. Each dot represent a single analyzed cell and a box plot the representative receptor.

Especially for CD2 and CD3, high variance in cluster density within the cell population can be observed. Additionally, to ensure drift free and high signal-to-noise measurements, the achieved localization precision (sigma) was checked for all measurements which on average ranged from 6.8 nm to 9.4 nm for the different analyzed receptors (Table 8).

Table 8 - Mean localization precision (sigma) \pm standard error of different analyzed receptors during dSTORM measurements. Mean of the localization precision in x- and y-direction is given for each receptor. All samples were stained with directly AF647 conjugated antibodies.

Receptor	CD2	CD3	CD11a	CD18	LFA-1	CD45	CD69	CD105
Localization precision [nm]	7.1 \pm 0.2	8.1 \pm 0.5	7.2 \pm 0.3	7.3 \pm 0.4	7.4 \pm 0.2	6.8 \pm 0.2	7.8 \pm 0.2	9.4 \pm 0.3

To obtain information about epitope accessibility in the range of a few nanometers, two-color dSTORM experiments were performed. However, the achievable maximum co-localization value under ideal conditions has to be determined first. Therefore, Jurkat T cells were stained according to the live cell staining protocol with an anti-CD45-AF647 antibody for 30 minutes with additional 15 minutes of 5 μ g/ml goat-anti-mouse (gam)-AF532 F(ab)₂ secondary antibody incubation prior to fixation. This duration was chosen because longer incubation times result in a clearly visible clustering of the otherwise homogeneously distributed CD45 receptor (Figure 12 A and B). A representative two-color image of anti-CD45-AF647 (magenta) and gam-AF532 (green) antibodies is shown in Figure 12 C. Although many pixels co-localize (white dots), still single green and magenta spots are visible. Co-localization analyses was performed by using Manders overlap coefficient (MOC) instead of the Pearson correlation coefficient (PCC). This is due to the fact that PCC reflects the correlation between intensities in two channels, while the MOC describes co-occurrence of two different spots in both channels. As co-localization of two proteins were analyzed MOC is better suited for this approach and was calculated with the Fiji Plugin *Coloc threshold* for three separate CD45 images. The plugin determines the co-occurrence of spots from one channel to another and vice versa named as tM1 (AF532 to AF647) and tM2 (AF647 to AF532) with a value of 1.0 for a completely co-localizing population. As unspecific binding can occur in both channels and more unspecific binding is observed for AF532 coupled antibodies tM2 is used to define the maximum co-localization. For anti-CD45-AF647 stained with a gam-AF532 a mean MOC of 0.55 (tM2) and 0.34 (tM1) for 20 nm/pixel image resolution and 0.34 (tM2) and 0.21 (tM1) for 10 nm/pixel was observed respectively (Table 9). This highlights that about half of the detected antibodies are not observed near their corresponding primary or secondary antibody. Even though not all spots showed an overlap, detection of co-localization in the range of 10-20 nm is possible for a certain amount of antibodies following the protocol described in 2.6.4. As a next step, co-localization within the same receptor population

was investigated using equal amounts of a directly-conjugated AF647- and AF532-coupled primary antibody. The cells were stained according to the live cell staining protocol and three different cells were analyzed respectively. Calculation of the MOC with *Coloc threshold* demonstrated no co-localization for CD11a ($tM1=0.00$; $tM2=0.00$), but a MOC of 0.07 for 10 nm/px and 0.14 for 20 nm/px for CD69. Representative *d*STORM images of CD11a and CD69 are shown in Figure 13 A and B. As an addition, the known heterodimer LFA-1, composed of CD11a stained by an AF647 coupled antibody (magenta) and CD18 stained by an AF532 coupled antibody (green), was imaged (Figure 13 C) and the MOCs determined. A subset of antibodies was able to bind adjacent areas visible by white spots with an average MOC of 0.26 for 20 nm/px ($n=3$) (Table 9). This means that for the dimeric receptors CD69 and LFA-1, a subset of antibodies was able to bind within a radius of a few nanometers. Additionally, comparing the localization precision of AF647 coupled antibodies to AF532 coupled antibodies showed better values for AF647, with localization precisions ranging between 7.23 nm and 7.57 nm compared to 8.13 nm to 12.03 nm for AF532.

Table 9 - Manders overlap coefficients of reconstructed rapid*d*STORM images with 10 and 20 nm per pixel for different receptors imaged with two-color *d*STORM. The shown Manders coefficients are averaged from $n=3$ cells.

	10 nm/px		20 nm/px	
	tM1	tM2	tM1	tM2
CD45 (AF647) + gam (AF532)	0.21	0.34	0.34	0.55
CD11a (AF647/AF532)	0.00	0.00	0.003	0.007
CD69 (AF647/AF532)	0.06	0.07	0.09	0.14
CD11a (AF647) + CD18 (AF532)	0.13	0.15	0.25	0.26

Table 10 - Localization precision (σ) \pm s.d. in x- and y-direction of AF532 and AF647 coupled antibodies. Measurements were acquired on the basal membrane of Jurkat T cells. Analysis was done on two-color *d*STORM images of cells stained prior to fixation with AF532 and AF647 coupled antibodies mixed in a 50:50 ratio.

	Localization precision [nm] AF532		Localization precision [nm] AF647	
	x-direction	y-direction	x-direction	y-direction
CD11a	11.37 \pm 2.10	12.03 \pm 1.88	7.57 \pm 1.07	7.23 \pm 1.43
CD45	8.13 \pm 0.53	9.78 \pm 0.86	7.25 \pm 0.40	7.33 \pm 0.53
CD69	9.03 \pm 1.0	11.47 \pm 1.14	7.47 \pm 1.01	7.36 \pm 0.79

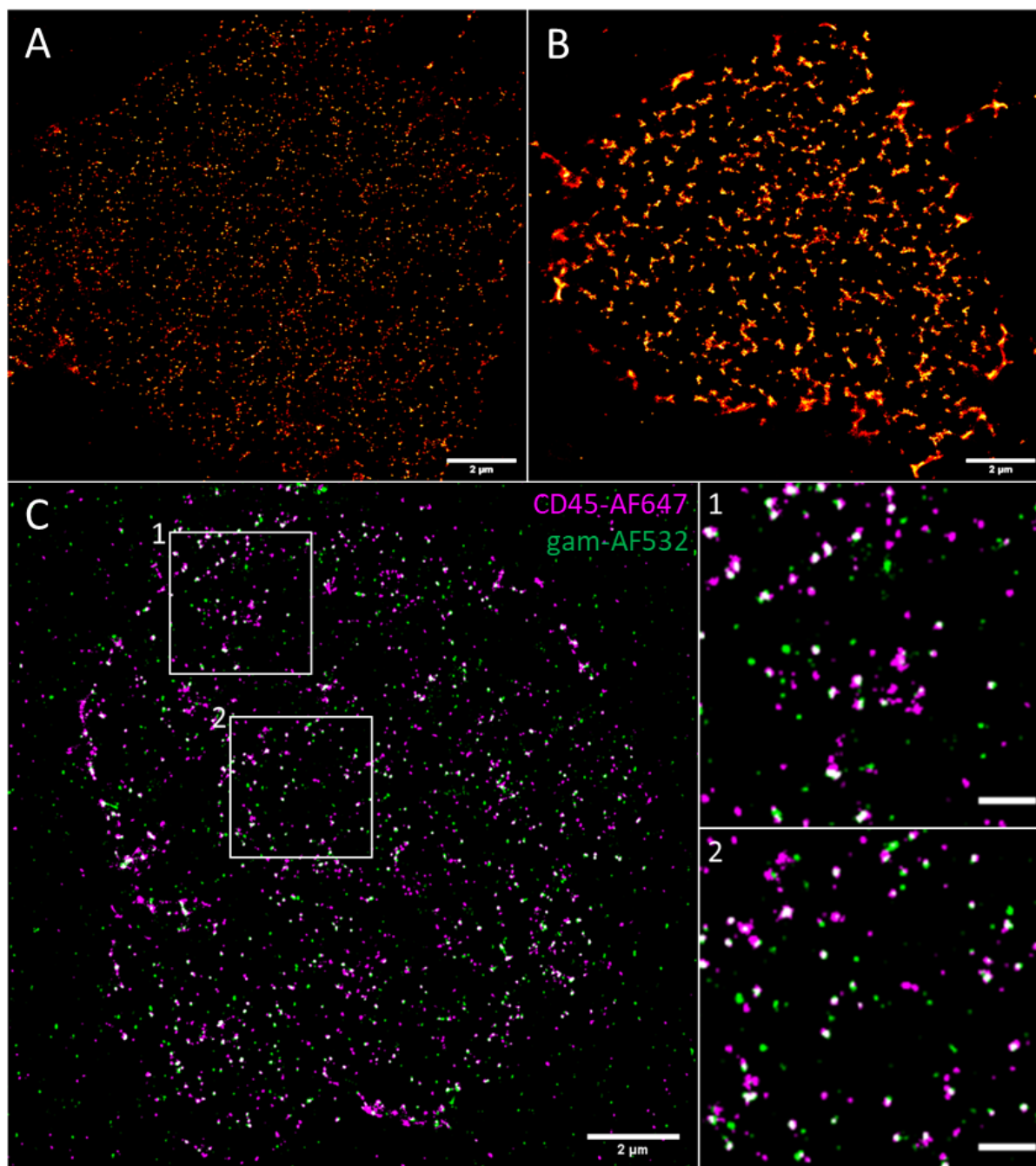


Figure 12 - Reconstructed *d*STORM images of the basal membrane of Jurkat T cells labeled with 5 $\mu\text{g/ml}$ anti-CD45-AF647. Cells were stained on ice for 30 min with an additional incubation of 5 $\mu\text{g/ml}$ goat-anti-mouse (gam) antibody for 15 min (A), 30 min (B) or with 5 $\mu\text{g/ml}$ gam-AF532 for 15 min (C) prior fixation. While short incubation times of the secondary antibody (A and C) preserve the mostly homogeneous distribution of the receptor, longer incubation times induce a strong aggregation of the receptor (B). Two-color *d*STORM images (C) demonstrate co-localization (overlaps in white) of anti-CD45-AF647 (magenta) and gam-AF532 (green) antibodies (20 nm/px). However, still approximately half of the antibodies seem to not co-localize. Scale bar of the insets: 500 nm.

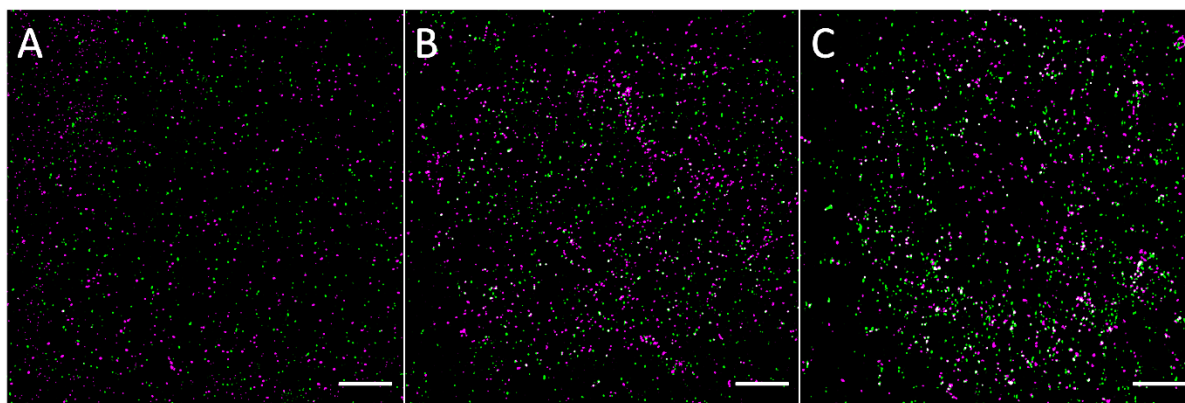


Figure 13 - Two-color dSTORM images of CD11a (A), CD69 (B) and CD11a/CD18 (C) on the basal membrane of Jurkat T cells. For A and B the staining solution contained half of the recommended amount AF532 (green) and the other half of AF647 (magenta) directly conjugated primary antibodies. In C the heterodimer LFA-1, composed of CD11a (magenta) and CD18 (green), is shown. Compared to LFA-1, CD69 shows less co-localization (white spots) and CD11a no co-localization at all. Manders overlap coefficients (MOC) for the shown images are 0.0 (A), 0.21 (B) and 0.32 (C) for tM2. All images were reconstructed with rapidSTORM and a pixelsize of 20 nm/px. Scale bars: 2 μ m.

Because some receptors show visible clustering, Ripley's h-function was calculated for all imaged receptors and compared with the simulated data. Ripley's h-function is helpful to determine the average size of localization clusters making aggregation of proteins visible. As one visualized antibody contains around 7-10 localizations on average, a Neyman-Scott distribution (upper gray lines Figure 14) was simulated as it reflects the random distribution of experimental gathered SMLM data better than the complete spatial randomness (lower gray line Figure 14). Comparison of the mainly monomeric receptors CD2, CD11a, CD18 and CD45 (Figure 14 A blue curve), but also of the dimeric receptors LFA-1, CD45 + γ F(ab)₂, CD69 and CD105 (Figure 14 B blue curve) demonstrated no difference to the simulated data with the amplitude of localization cluster sizes at \sim 20 nm. However, CD3 (Figure 14 C blue curve) shows a clear shift of the localization cluster size towards \sim 60 nm. Additionally, Ripley's h-function of equal amounts of unlabeled and AF647-labeled CD69 antibody (Figure 14 D blue curve) showed the same trend seen for the monomeric and dimeric receptors.

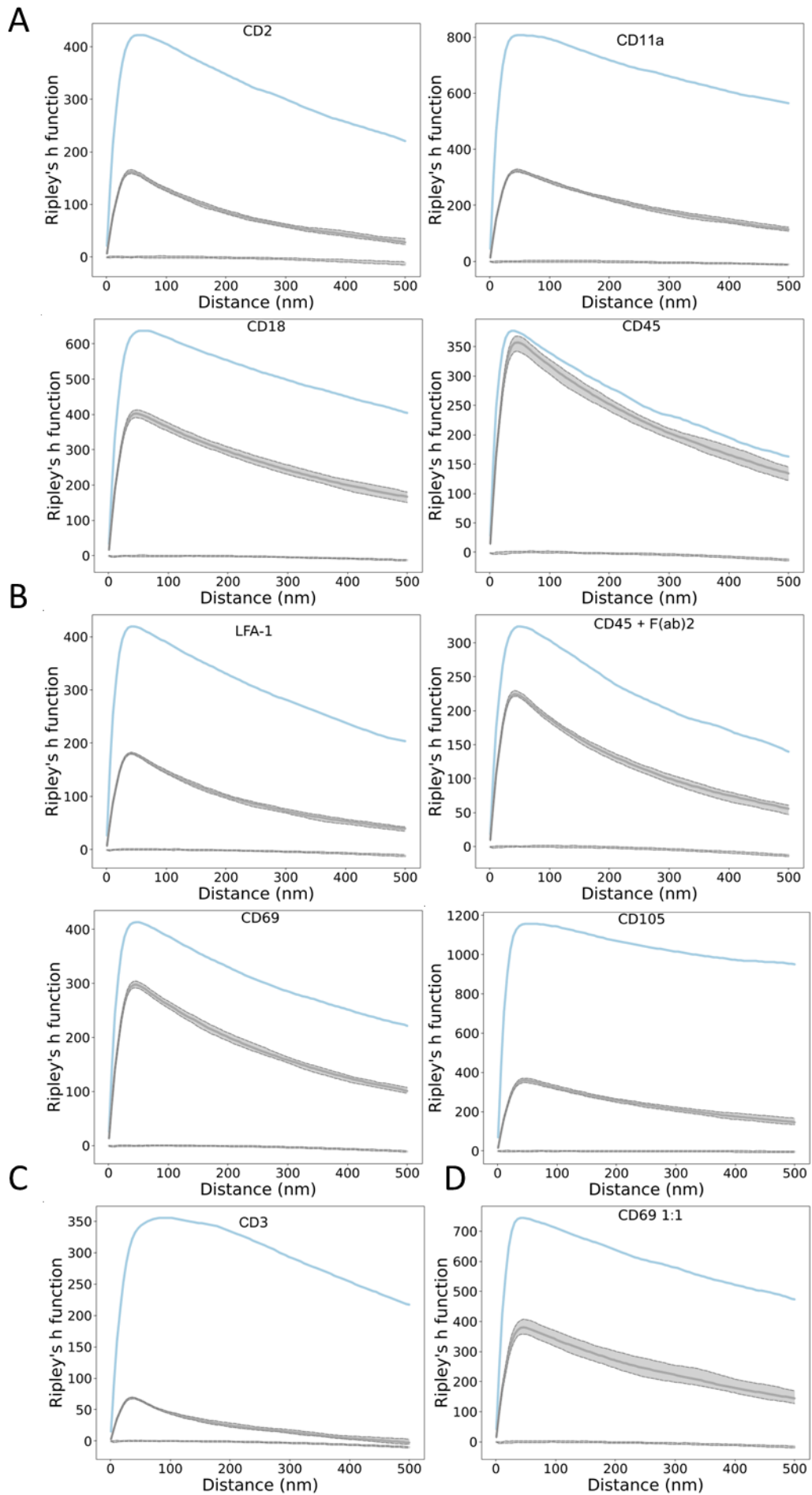


Figure 14 - Ripley's h-function of different monomeric (A), dimeric (B), a clustering (C) and a CD69 1:1 (D) receptors. No difference for the size of the localizations clusters between the experimental data (blue curves) of A and B and the simulated data of a clustered Neyman-Scott process (gray curves) was observed. For CD3 (C) a shift of the maximum localization cluster size towards ~60 nm compared to the Neyman-Scott process is visible suggesting present receptor aggregations. CD69 used in a 1:1 ratio of unlabeled and AF647 coupled antibodies also follows the trend of A and B. Additionally, simulated data with spatial distributions following complete spatial randomness is shown (lower gray curves).

As Ripley's h-function was able to detect changes in receptor aggregation of bigger clusters but not of smaller oligomers, a different parameter was required to distinguish between small nanocluster and monomeric receptors. Therefore localization data of two known homodimeric (CD69, CD105), one heterodimeric (LFA-1) and one monomeric receptor (CD45) were analyzed. Additionally, a primary CD45 antibody with an additional goat-anti-mouse F(ab)₂ secondary antibody was used creating a pseudodimer and compared to the monomeric receptors (CD11a, CD18, CD45) stained only with a primary antibody. All the different primary monoclonal antibodies and the secondary gam F(ab)₂ antibody were coupled to AF647 with an average degree of labeling of 2-4 each. Cluster analyses was performed by the DBSCAN algorithm implemented in Locan with $\epsilon = 20$ nm and MinPts = 3 and the localizations per cluster were plotted as probability density function (PDF). Of note, PDFs display the normalized probability of all present localizations per cluster quantities which add up to 1. Further analyses demonstrated less localizations per cluster for CD2, CD11a, CD18 and CD45 (Figure 15 A) compared to LFA-1, CD69, CD105 and CD45 with an additional F(ab)₂-AF647 attached to it (Figure 15 B). All monomeric receptors showed localization quantities over 0.12 for three blinking events, with a fast decreasing distribution and basically no localization events over 25 occurring per cluster. The mean localizations per cluster \pm standard error (s.e.) varied between 7.3 ± 0.2 (s.e.) and 10.1 ± 0.4 (s.e.) localizations per cluster. In contrast, all known dimeric receptors or CD45-AF647 stained with an additional gam F(ab)₂-AF647 (pseudodimer) started below 0.1 for 3 localizations per cluster and decreased significantly slower with more events occurring over 25. For these receptors, compared to the monomeric receptors, higher mean localization numbers per cluster \pm standard error (s.e.) were observed, varying between 14.4 ± 0.3 (s.e.) and 17.9 ± 0.9 (s.e.) localizations per cluster. For CD3 (Figure 15 C) the distribution is similar to the dimeric receptors, probably due to the strong heterogeneity of the receptor, with a mean localization density of 16.4 ± 0.6 (s.e.) localizations per cluster. Staining Jurkat T cells with equal amounts of unlabeled

and AF647-labeled CD69 antibody (Figure 15 C CD69 1:1) also resulted in a PDF curve between the monomeric and the dimeric trends. This is also visible by the mean localizations per cluster \pm standard error of 12.2 ± 0.2 (s.e.) localizations per cluster (Table 11). Taken together, the combination of Ripley's h-function and localization data analyses show the possibility to distinguish between monomeric, small oligomers and strongly clustered receptors, although small oligomers are barely visible in the reconstructed images.

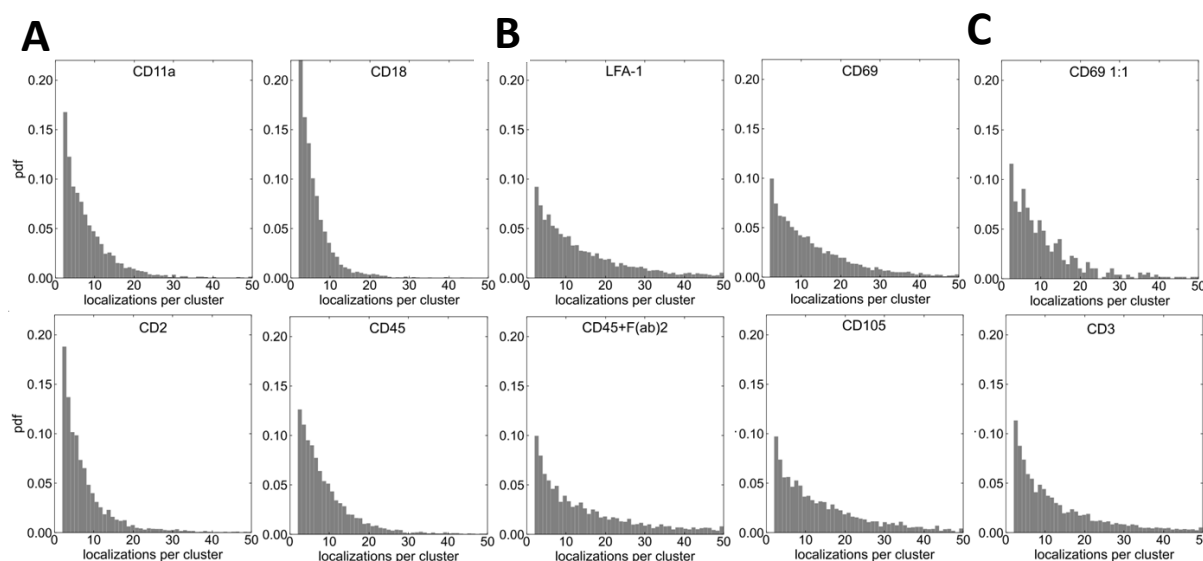


Figure 15 - Probability density functions (PDF) of the localizations per cluster for different monomeric and dimeric receptors. Monomeric receptors (A) show higher quantities of 5-8 localizations per cluster and barely any events over 25 localizations per cluster. The PDF of known homodimeric, heterodimeric or receptors carrying at least two antibodies (B) has a value below 0.10 for 5-8 localizations per cluster and is right shifted with significantly more localizations per cluster over 25. The partially clustering and heterogenic receptor CD3 (C) shows a similar distribution of localizations per cluster as the dimeric ones. In contrast, the combination of unlabeled and AF647-labeled CD69 antibodies in a 1:1 ratio shows a trend between monomeric and dimeric distribution (C, CD69 1:1). Analyses was done with Locan and the DBSCAN parameters $\epsilon = 20$ nm and MinPts = 3.

Table 11 - Mean localizations per cluster \pm standard error for different analyzed receptors on Jurkat T cells.

Monomer	Receptor	Mean localization per cluster \pm standard error
	CD2	9.2 ± 0.2
	CD11a	9.6 ± 0.3
	CD18	7.3 ± 0.2
	CD45	10.1 ± 0.4
Monomer/Dimer	CD69 1:1	12.2 ± 0.2
Dimer	LFA-1	16.3 ± 0.4

	CD45+F(ab)2	17.9 ± 0.9
	CD69	14.4 ± 0.3
	CD105	16.3 ± 1.1
Oligomer	CD3	16.4 ± 0.6

Even though all cells from the previously described experiments originated from the same cell population, high fluctuations of receptor expression and oligomerization were observed. For TNF receptors, for example, a decrease in receptor expression has been shown during the M-phase (Pocsik et al. 1995) of the cell cycle. Because no cell cycle synchronization prior to the staining procedure was performed, Jurkat T cells were arrested in different cell cycle phases and the receptor expression and aggregation of two different receptors was compared. By incubating cells with 5 mM hydroxyurea for 24 h the movement of DNA replication is slowed down, leading to an arrest in the S-phase (Xu, Singh, and Alter 2016). An arrest in the G0/G1 phase was induced by serum starvation (0% FCS) for 24 h. Afterwards, the expression of CD28 and CD69 was compared to control cells cultivated under standard conditions. Because receptor aggregations were observed, receptor densities were estimated by dividing the localization density (localizations/ μm^2) by 9 according to the results for monomeric receptors (see Table 11).

On control cells, CD28 showed a mean receptor density \pm standard error (s.e.) of 40.0 ± 0.2 (n=12) receptors per μm^2 and aggregation of some CD28 molecules. Those aggregations are also visible for serum starved, but not for hydroxyurea-treated cells. Additionally, receptor densities are strongly reduced for hydroxyurea-treated cells visible by receptor densities \pm standard error of 10.0 ± 0.5 (s.e.) (n=17) compared to 40.0 ± 0.3 (s.e.) receptors per μm^2 for FCS-starved cells (n=7) (Figure 16 A). In comparison, Jurkat T cells are negative for CD69 on cells trapped in the S-phase while an upregulation is visible for FCS-starved cells (25.0 ± 1.0 (s.e.) (n=9)) compared to control cells (n=27) with 5.2 ± 0.4 (s.e.) receptors per μm^2 (Figure 16 B). At least for CD28, besides the receptor expression, aggregation of the molecules was altered for all three conditions, posing a possible explanation for high fluctuations on the same cell line.

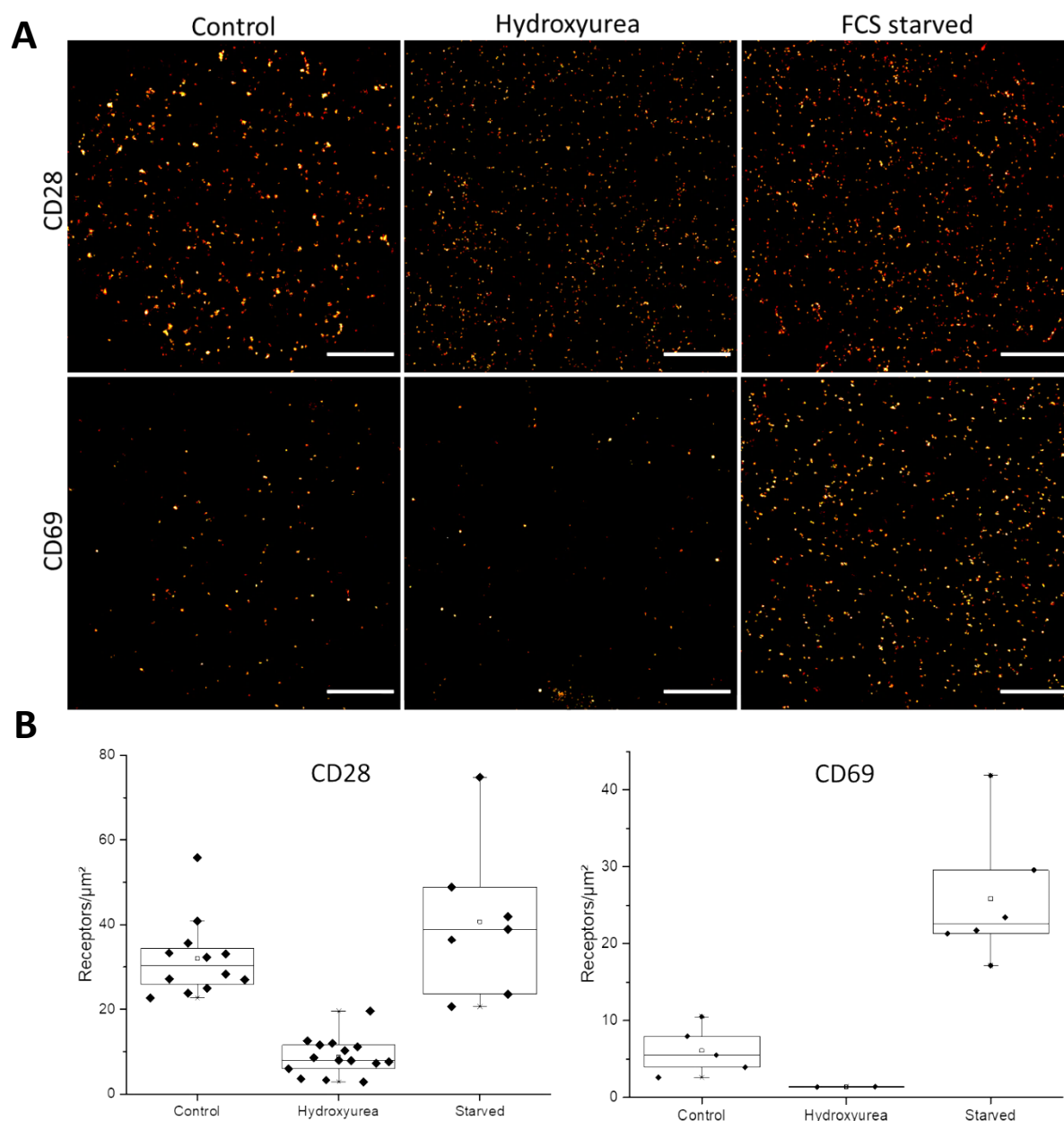


Figure 16 - Influence of different cell cycle phases on CD28 and CD69 receptor expression on Jurkat T cells. Cells were either treated under standard conditions (control cells), with 5 mM hydroxyurea for 24h (S-phase) or serum starved for 24h (G0/G1-phase). Image acquisition of the basal membrane was done by dSTORM (A) with standard settings and analyzed using a DBSCAN algorithm with $\epsilon = 20$ nm and MinPts = 3. The receptor density is shown in the boxplots for CD28 and CD69 (B). Each dot represents a single cell. Scale bars: 2 μm .

Ripley's h-function showed a random distribution for CD69 under all three conditions with a localization cluster size of ~ 20 nm (Figure 17 A) as seen from the monomers and homodimers before (Figure 14). However, a clear clustering for CD28 control cells with a localization cluster size of ~ 100 nm was observed, while hydroxyurea-treated cells showed a random distribution with a localization cluster size of ~ 20 nm. For FCS-starved cells a slightly increased localization cluster size of ~ 40 nm was

observed. These changes are also reflected in the “blinking” statistics of CD28 (Figure 17 B). The control cells containing clearly visible clusters showed similar localizations per cluster as the FCS-starved cells with localizations of 25 and above being present. In contrast, the hydroxyurea-treated cells showed no clusters with such high quantities of localizations. For CD69 FCS-starved cells, an increased localization cluster size of ~100 nm (Figure 17 A) and slightly increased mean localizations per cluster were visible compared to the CD69 control cells (Figure 17 B). Still the trend resembles the dimeric curves seen in Figure 15 B for both conditions. However, treatment with hydroxyurea strongly decreased the CD69 population and only few localizations were detected (Figure 17 B). These few binding events are insufficient to analyze even though they appeared dimeric (Figure 17 B). Also the mean value for the localizations per cluster \pm standard error (s.e.) shown in Table 12 demonstrate a big difference between CD28 control and CD28 FCS-starved cells with 19.1 ± 0.9 (s.e.) and 18.5 ± 0.7 (s.e.) localizations per cluster compared to hydroxyurea-treated cells with 8.8 ± 0.2 (s.e.) localizations per cluster. For CD69 no significant differences were observed with localization values ranging from 14.4 ± 0.4 (s.e.) to 17.1 ± 1.3 (s.e.) localizations per cluster.

Table 12 - Mean localizations per cluster with standard error for CD28 and CD69 on Jurkat T cells treated under different conditions.

	Mean localizations per cluster \pm standard error		
Receptor	Control	Hydroxyurea	FCS starved
CD28	19.1 ± 0.9	8.8 ± 0.2	18.5 ± 0.7
CD69	14.4 ± 0.4	16.1 ± 0.9	17.1 ± 1.3

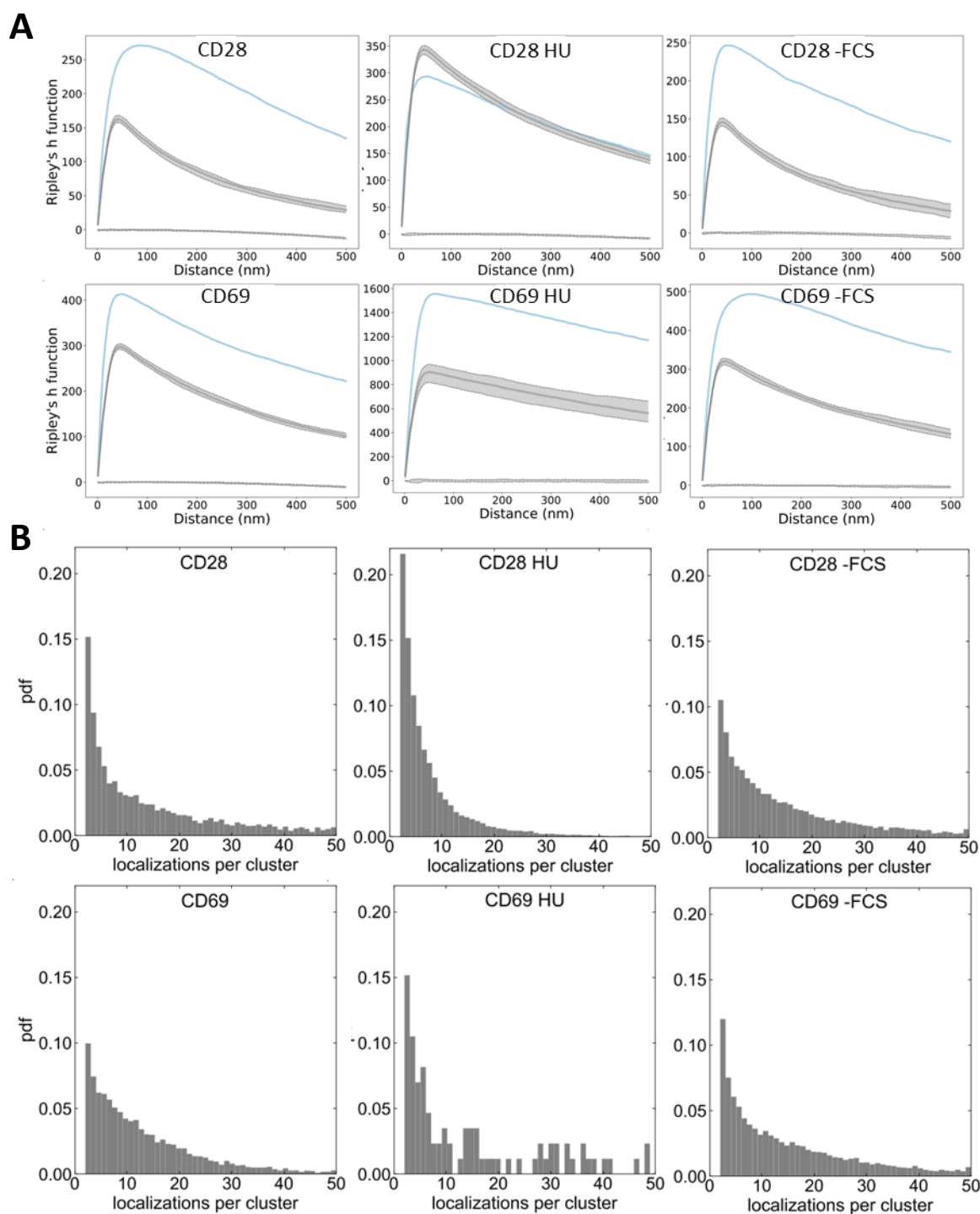


Figure 17 - Ripley's h (A) and probability density function (PDF) (B) for CD28 and CD69 on Jurkat T cells treated with different cell phase synchronizing chemicals. A non-random cluster formation of ~100 nm for CD28 on control cells was confirmed by Ripley's h-function (blue curves, A) similar to the simulated data (gray curves A) and also by localization density analysis (B). For serum-starved cells a reduced localization cluster size of ~40 nm was observed and a random distribution with ~20 nm localization cluster size for hydroxyurea-treated cells. Additionally, localization density of FCS-starved cells was higher compared to hydroxyurea-treated cells. Analysis of CD69 showed a random distributed localization cluster size of ~20 nm for control and an increased cluster size of ~100 nm for FCS-starved cells (A), whereas localization density of these cells suggests a dimeric population present (B). For hydroxyurea-treated cells the amount of detected CD69 antibodies was insufficient to get reliable statistics. Analysis was done using a DBSCAN algorithm with $\epsilon = 20$ nm and MinPts = 3.

3.2 The Treg receptome

The immune system is a quite complex machinery with regulation and inhibition of immune responses causing a proper reaction to healthy or aberrant cells or infections. Regulatory T cells (Treg) represent only around 6% of all T cells but maintain balance between T cell resting and killing. In this chapter, various important receptors on primary mouse regulatory T cells ($CD4^+ CD25^{\text{high}} FoxP3^+$) were quantified before and after activation. Purification was done by Dr. Julia Delgado-Tascon (Beilhack group) from the Department of Medicine II & Pediatrics University Hospital Würzburg. Cell staining and *d*STORM measurements were performed together with Dr. Ralph Götz from our department. As this project was performed before the protocol mentioned in 3.1 had been established, receptor quantities were estimated by dividing the localizations per μm^2 by 7 as it was thought to represent the blinking event of one single antibody at this time.

Primary mouse regulatory T cells were investigated for their receptor expression before and after activation of TNFR2 by **Selective TNF-based Agonist of Receptor 2 (STAR2)**. Cells were stained according to the live cell staining protocol prior to fixation with 4% paraformaldehyde on ice for 30 minutes. Additionally, to maintain a sufficient basal attachment to the PDL-coated Lab-Teks, Tregs were centrifuged at 400x g with de-acceleration set to 5. The expression profiles of natural Treg receptors (CD3, CD4 and CD25 shown in Figure 18), co-inhibitory molecules (CD279), activation molecules (CD103, CD134, GARP, GITR) as well as TNFRSF co-stimulatory receptors (CD120b, CD137, DR3) were checked before and after activation (Figures 18-20). No significant differences in receptor densities (receptors/ μm^2) or clustering between STAR2-activated and native Tregs were observed for CD3 (33.9 ± 2.5 (s.e.) $n=15$ compared to 36.2 ± 1.8 (s.e.) receptors/ μm^2 $n=33$). Receptor densities \pm standard error were slightly increased on STAR2-activated cells for CD4 (39.3 ± 2.0 (s.e.) $n=15$) and for CD25 (43.7 ± 4.8 (s.e.) receptors/ μm^2 $n=11$) compared to the native cells (CD4: 35.8 ± 2.2 (s.e.) $n=26$, CD25: 35.0 ± 2.8 receptors/ μm^2 (s.e.) $n=37$). Nevertheless, the variance between the cells is very high on activated Tregs with receptor densities varying between 22.0 and 65.9 CD25 receptors per μm^2 for instance (Figure 21 A). Additionally, no clustering of any receptor was observed before and after activation.

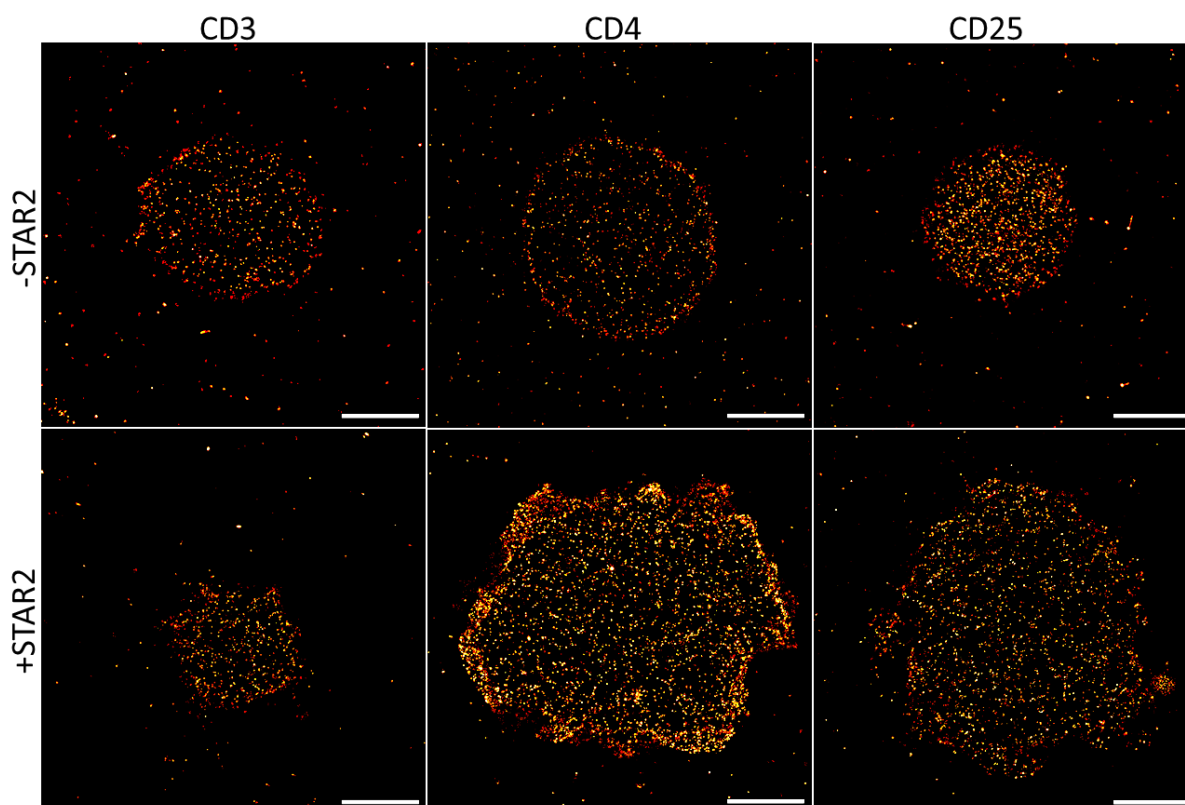


Figure 18 - Representative dSTORM images of the T regulator cell (Treg) markers CD3, CD4 and CD25 before and after STAR2 activation. All cells were stained with AF647 labeled antibodies according to the live cell staining protocol and fixed on ice for 30 min with 4% PFA. While STAR2 activation of Tregs had no influence on the CD3 expression, CD4 and CD25 showed an increased expression profile. Furthermore, all receptors under both conditions seem to be homogeneously distributed over the cell membrane. Scale bars: 2 μm .

Also for CD103, CD120b, CD134 and CD279, a homogeneous distribution without clustering is observed before and after activation with STAR2. All of the used antibodies demonstrated a clear membrane staining with low quantities of unspecific binding events to the glass surface. Additionally, all the receptors show a high expression variance on the purified Treg cell population. For CD103 the detected mean receptor density \pm standard error of 7.6 ± 0.9 (n=31) was slightly reduced to 6.2 ± 0.9 (s.e.) receptors per μm^2 (n=31) after STAR2 activation. For CD120b a nearly twofold increase to 7.2 ± 0.9 (s.e.) (n=16) was detected after activation, compared to 4.0 ± 0.5 (s.e.) receptors per μm^2 (n=27) for the native form. This was also observed for CD134 with 9.3 ± 0.6 (s.e.) (n=21) compared to 5.8 ± 1.0 (s.e.) receptors per μm^2 (n=16). In contrast, CD279 was slightly reduced after activation from 13.0 ± 1.3 (s.e.) (n=9) to 9.9 ± 2.3 (s.e.) receptors per μm^2 (n=11). Even though, detected receptor expressions were quite different within the cell population changes in receptor quantities after

activation could be observed with no visible changes in receptor distribution (Figure 19 & 21).

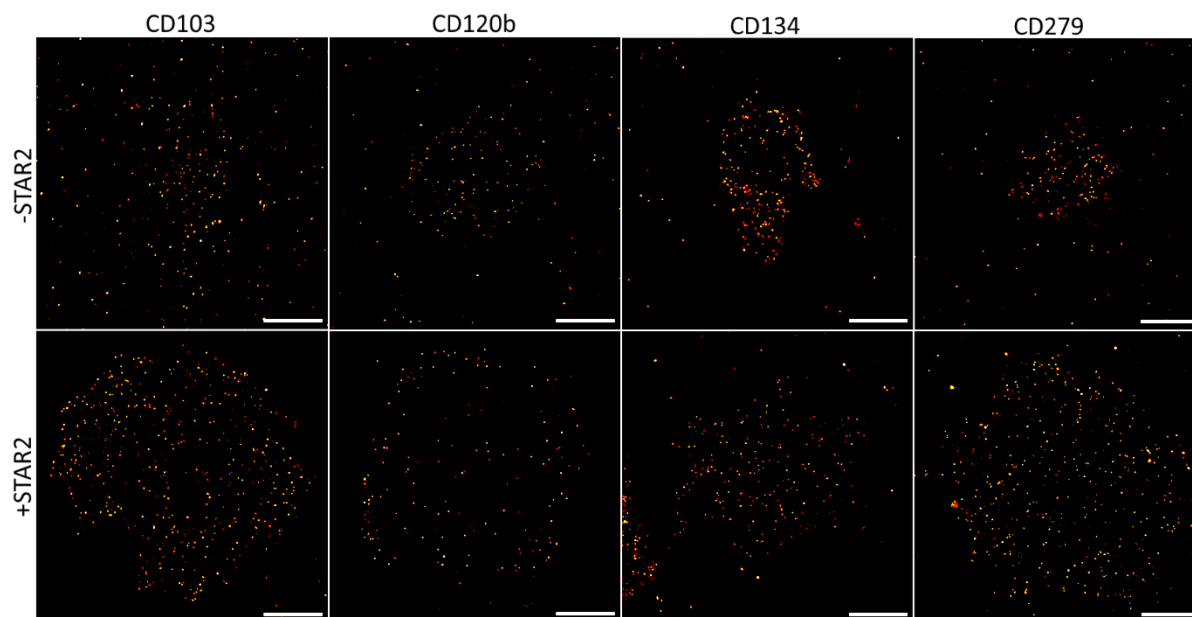


Figure 19 - Representative dSTORM images of various important T regulator cell (Treg) receptors before and after STAR2 activation. Staining of T regulator cells was done according to the live cell staining protocol with AF647 coupled antibodies. Expression of CD103 was only minor changed, while CD120b and CD134 expression was upregulated upon activation. In contrast, CD279 showed a reduced receptor expression. All receptors seem to be homogeneously distributed over the cell membrane. Scale bars: 2 μm .

In contrast to previous described receptors, CD137, DR3, GARP and GITR were analyzed only after STAR2 activation (Figure 20). While CD137 and GARP showed a rather homogeneous distribution on the surface, light clustering was visible for DR3 and, even more pronounced for GITR with clusters of $\sim 200\text{-}500\text{ nm}$. Cluster analyses resulted in mean receptor densities \pm standard error (s.e.) of 5.6 ± 0.6 (s.e.) for CD137 ($n=29$), 2.8 ± 0.2 (s.e.) for DR3 ($n=8$), 2.6 ± 0.2 (s.e.) for GARP ($n=34$) and 121.0 ± 10.6 (s.e.) receptors per μm^2 for GITR ($n=28$) (Figure 21).

Most of the addressed receptors showed similar expression quantities ranging between 2-10 detected receptors/ μm^2 , with only Treg specific receptors and GITR being highly abundant. For each receptor, single cells are shown as dots in the representative box plots in Figure 21.

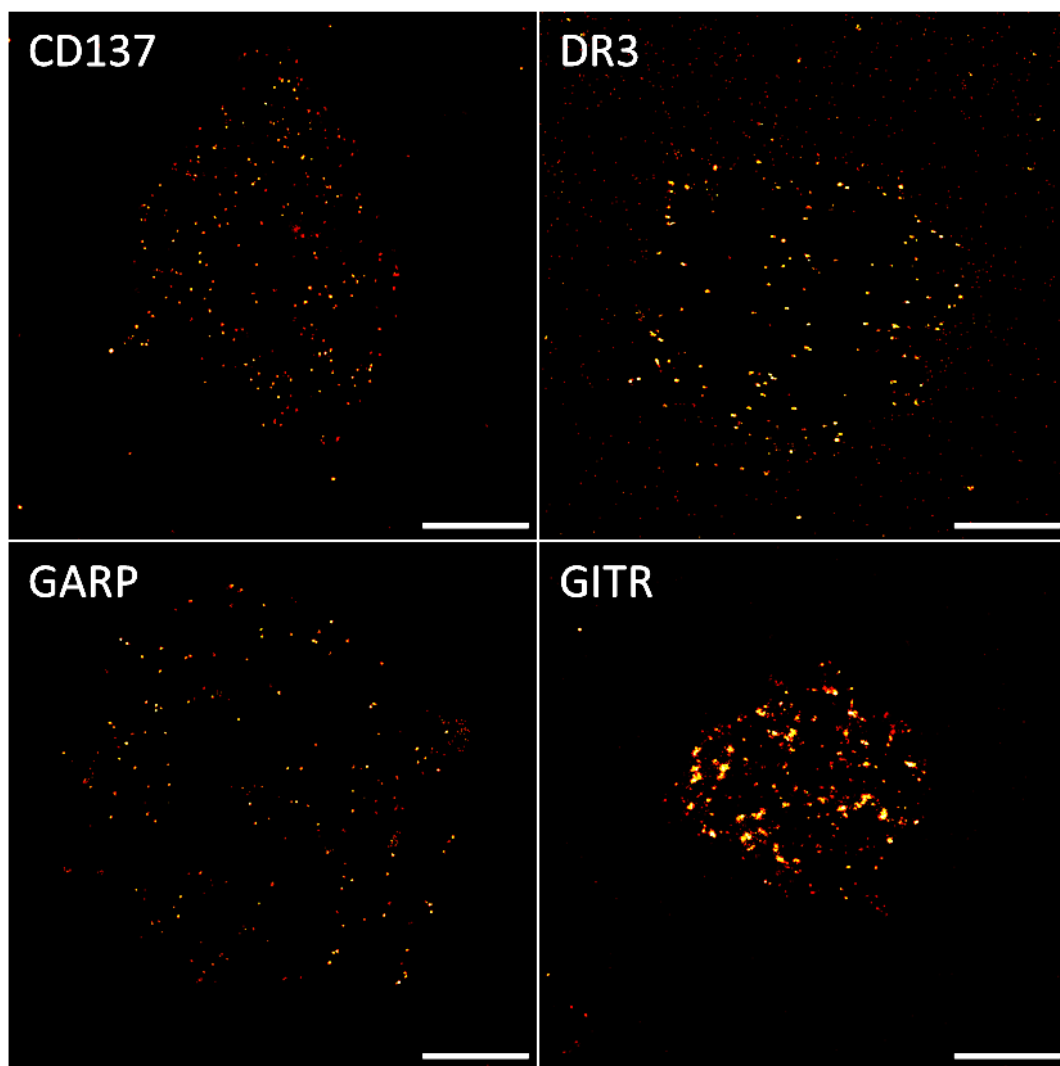


Figure 20 - Representative dSTORM images of the basal membrane of Tregs stained for either CD137, DR3, GARP or GITR after STAR2 activation. Staining of T regulator cells was done according to the live cell staining protocol with AF647 coupled antibodies. For all targets, a specific membrane staining with no antibodies bound to the glass surface was observed. Additionally, all receptors seem to be homogeneously distributed except for GITR, which formed clusters. Scale bars: 2 μm .

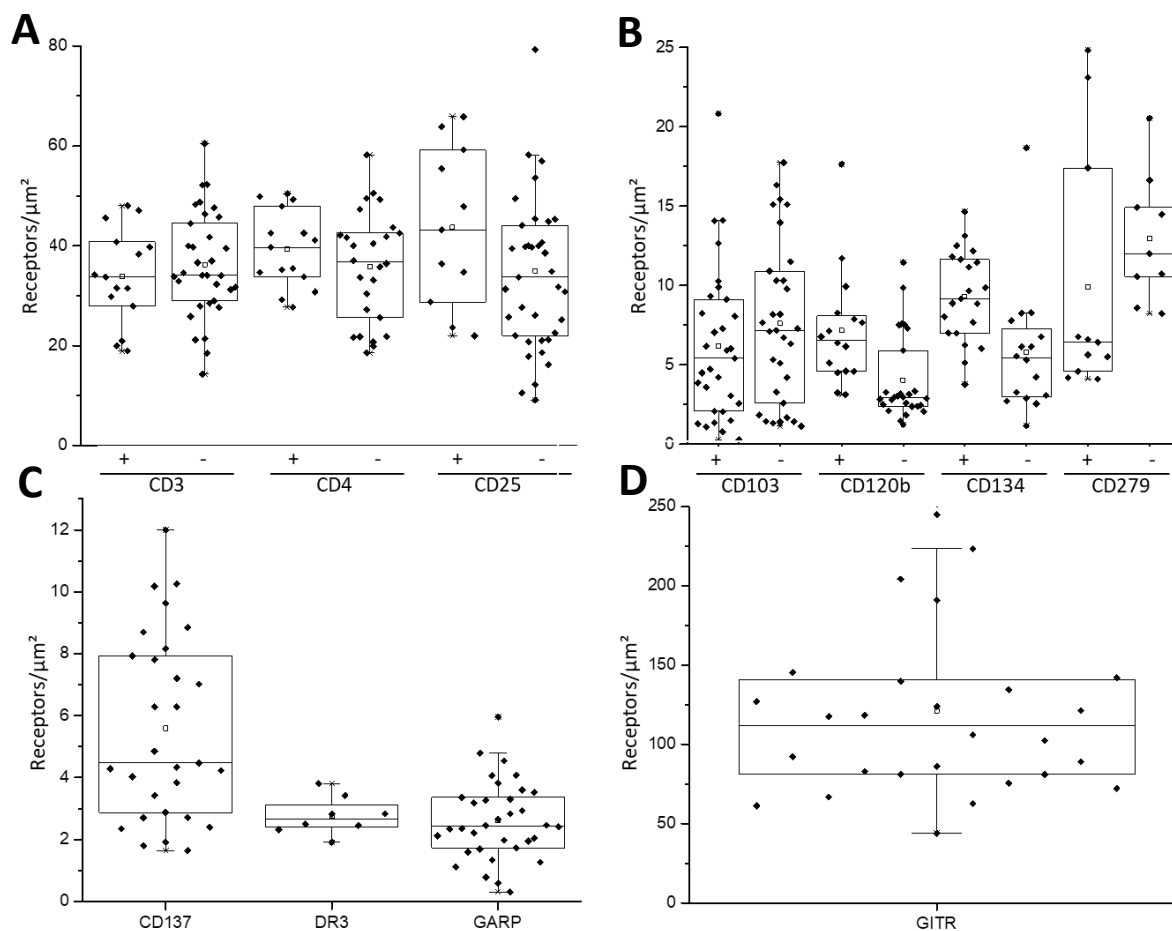


Figure 21 - Quantitative analyses of different receptors before (-) and after (+) STAR2 activation (A and B) and after activation only (C and D) on regulatory T cells. Analyses was done using a DBSCAN algorithm with $\epsilon = 20$ nm and MinPts = 3. Each dot represents a single cell.

3.3 Multiple myeloma

In this chapter, quantification of receptors, particularly of the receptor CD38 which is relevant in multiple myeloma, but also for several other clinically important targets, is described. Quantification was performed on various cell lines as well as on primary multiple myeloma cells from patients in collaboration with Prof. Dr. Martin Kortüm from the Department of Internal Medicine II of the University Hospital Würzburg

3.3.1 CD38 detection on multiple myeloma cells

On multiple myeloma cells, CD38 is highly abundant and can be addressed by the monoclonal antibody daratumumab for immunotherapy. For reliable quantification of

patient samples, it is therefore important to have the ability to detect all CD38 molecules, even though daratumumab has already been preceded as treatment. Two different antibodies were assessed on their ability to detect CD38 in the absence or presence of this drug. MM.1S cells were treated with or without 15 µg/ml daratumumab for 90 minutes at 37°C before being stained on ice with either the monoclonal anti-CD38-AF647 (HIT2) antibody or the polyclonal anti-CD38-AF647 (ME) antibody prior to fixation. Cells were checked for signal at the CLSM with the standard settings applied and detected signal was adjusted in Fiji to 0-1500 ADC. MM.1S cells stained with both the monoclonal and polyclonal antibodies showed a clear membrane staining in the absence of daratumumab (Figure 22, upper panel). However, incubation with daratumumab results in little to no CD38 being detected by the monoclonal antibody anymore, while the detected signal of the polyclonal CD38 antibody remained almost the same (Figure 22, lower panel). Therefore, the polyclonal CD38 antibody was used for following quantification experiments to ensure comparable results between individual patients before and after daratumumab treatment.

As a next step, CD38 expression was quantified on the basal layer of three different primary myeloma samples via *d*STORM. Representative *d*STORM images of MM cells of patient 225 (A), patient 379 (B) and patient 394 (C) as well as quantification statistics of all three patients (D) are shown in Figure 23. All three patients had been treated with daratumumab prior microscopy (Table 2), but the disease still progressed in patients 225 and 394, with only patient 379 showing a regressive trend under this medication. All patients' cells show differently sized membrane attachment areas as well as a clear CD38-expression, detected by the polyclonal CD38 (ME) antibody. Additionally, the unspecific binding of the antibody to the glass surface is highest for the lowest CD38-expressing myeloma cells of patient 225. Quantification of CD38 with the software Locan and the implemented DBSCAN algorithm with $\epsilon = 20$ nm and MinPts = 3 (Figure 23 D) showed mean cluster densities \pm standard error (s.e.) of 20.8 ± 1.6 (s.e.) for patient 225 (n=8), 23.3 ± 2.1 (s.e.) for patient 379 (n=6) and 47.4 ± 2.9 (s.e.) clusters per μm^2 for patient 394 (n=9). Interestingly, the investigated cells of the progressive patient 225 and the responding patient 379 demonstrated rather identical expression quantities of CD38 on their surface. Unfortunately, the disease was also advancing for patient 394 even though CD38 is highly abundant and daratumumab has been administered in 2019.

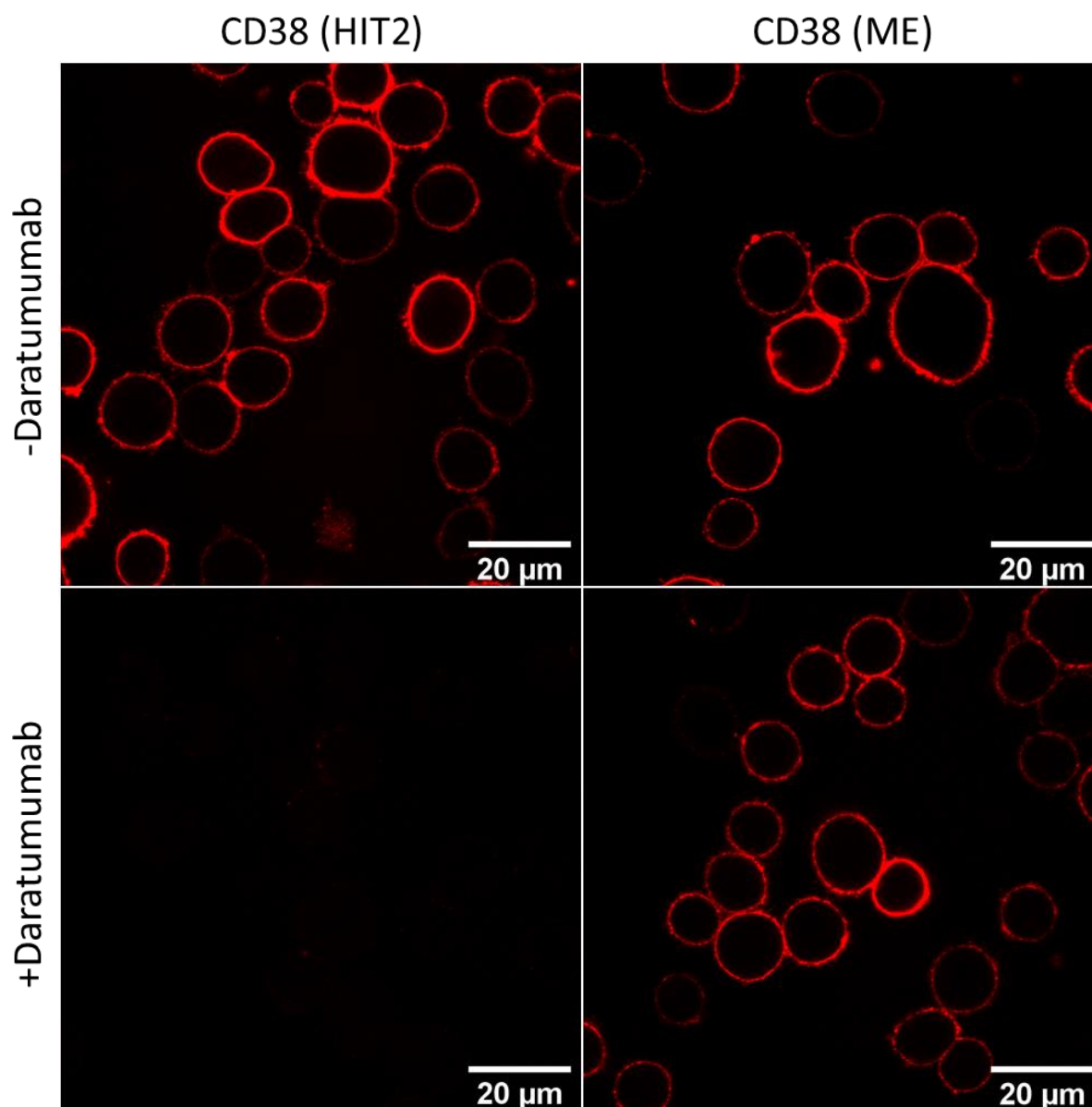


Figure 22 - Confocal laser scanning microscope images of MM.1S cells stained with CD38 (HIT2) and CD38 (ME) Alexa Fluor 647 coupled antibodies in the absence and presence of 15 µg/ml daratumumab. Imaging was performed under standard settings and signal adjusted to 1-1500 ADC. No signal was detected for anti-CD38 (HIT2) when preincubated with daratumumab suggesting blocking of this epitope. This effect was not visible for the polyclonal anti-CD38 (ME) antibody.

However, due to the gain of chromosome 1 (1q) and the translocations of t(14;16) and t(14;20) patient 394 is considered to be a high-risk patient for early relapse, having a poor prognosis compared to patient 379 with translocation of t(11;14) (Rajkumar 2020) (Table 2). Additionally, the localizations per cluster of both patients stained with the polyclonal CD38-AF647 (ME) antibody were analyzed and compared to patient 2023 stained with the monoclonal CD38-AF647 antibody (Figure 24). While patients 379 and 394 show a dimeric trend for their localization statistics (localizations/cluster), the

localization statistic of patient 2023 suggest a monomeric trend as seen in Figure 15 in chapter 3.1.

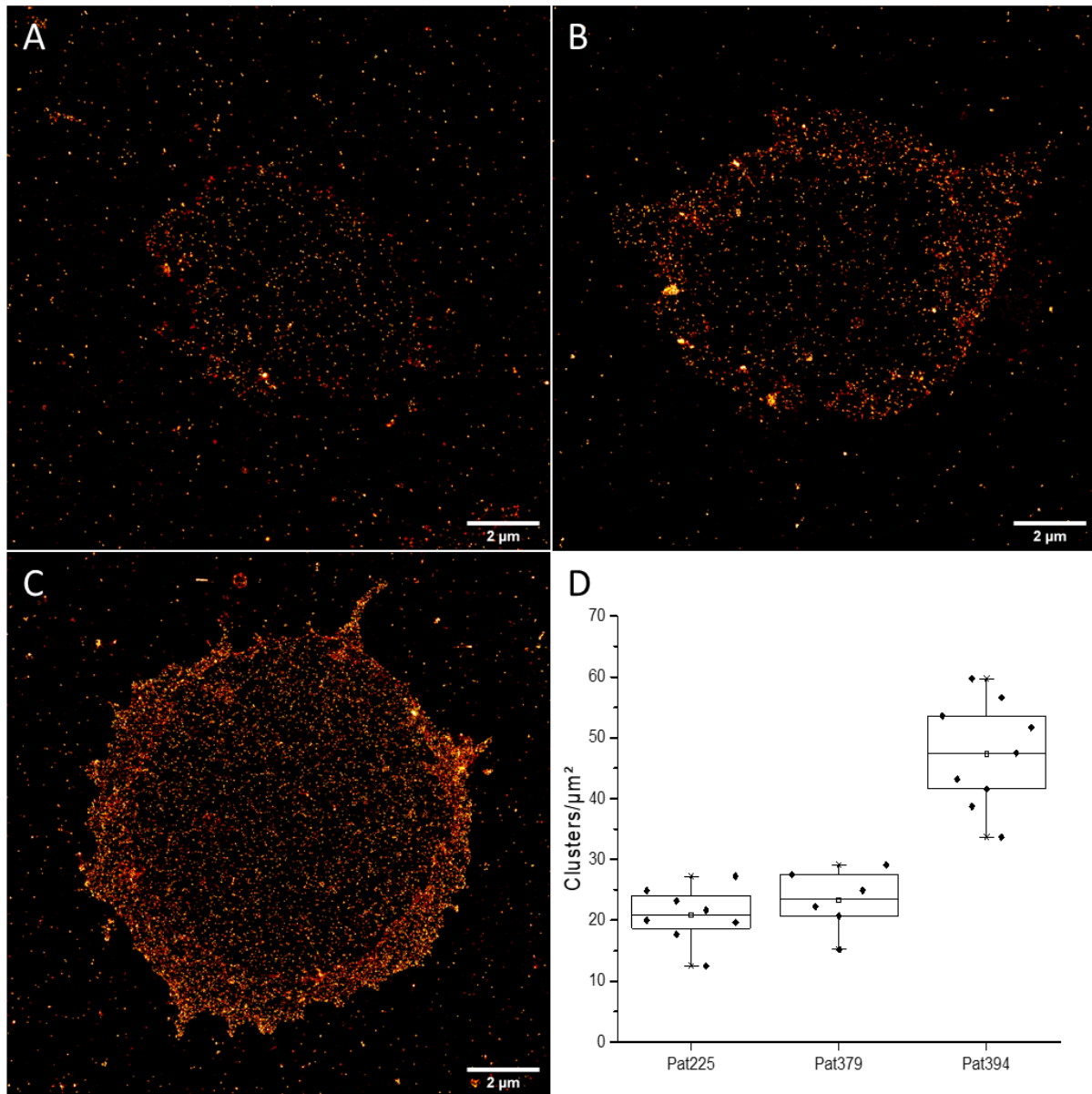


Figure 23 - Representative dSTORM images of the basal membrane of primary multiple myeloma cells stained with anti-CD38-AF647 (ME). All cells were stained according to the live cell staining protocol with 7.5 μg/ml anti-CD38-AF647 (ME). Quantitative analyses with Locan and the implemented DBSCAN algorithm with $\epsilon = 20$ nm and MinPts = 3 of patient 225 (A), patient 379 (B) and patient 394 (C) are shown in the boxplots (D) with each dot representing a single cell. Scale bars: 2 μm.

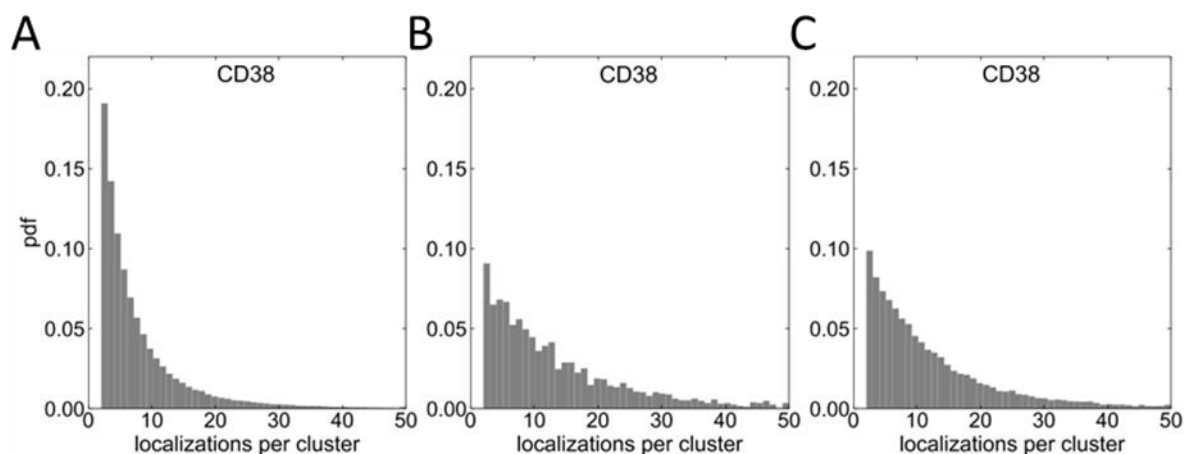


Figure 24 - Probability density functions (PDF) of the localizations per cluster for patient 2023 stained with the monoclonal antibody CD38-AF647 (HIT2) (A) and patient 379 (B) and patient 394 (C) stained with the polyclonal antibody CD38-AF647 (ME). While the PDF of the monoclonal CD38 antibody showed a rather monomeric distribution the PDF of cells stained with the polyclonal CD38 antibody suggest a dimeric population present.

3.3.2 Promising targets for multiple myeloma

Although daratumumab is the standard treatment for most multiple myeloma patients, the aim persists to find novel targets for cancer therapy. This is particularly important since most patients will develop a relapsing/refractory multiple myeloma (RRMM) with no further response to CD38 mAbs.

Therefore, the patients 379 and 394 were further analyzed for their receptor expression of CD138, BCMA, SLAMF7, CD19 and CD20. The staining, imaging and quantification was performed the same way as described in 3.1. Representative *d*STORM images (Figure 27) and their respective quantification are shown in Figure 26. Patient 379 shows not only a high variability of cluster/ μm^2 with the exception of BCMA, but also a completely different expression profile compared to patient 394. Additionally, cell populations of both patients showed a differing cell morphology with a mean cell diameter \pm standard deviation of $8.1 \pm 0.7 \mu\text{m}$ (s.d.) ($n=10$) for patient 379 compared to $12.3 \pm 3.7 \mu\text{m}$ (s.d.) ($n=10$) for patient 394 (Figure 25).

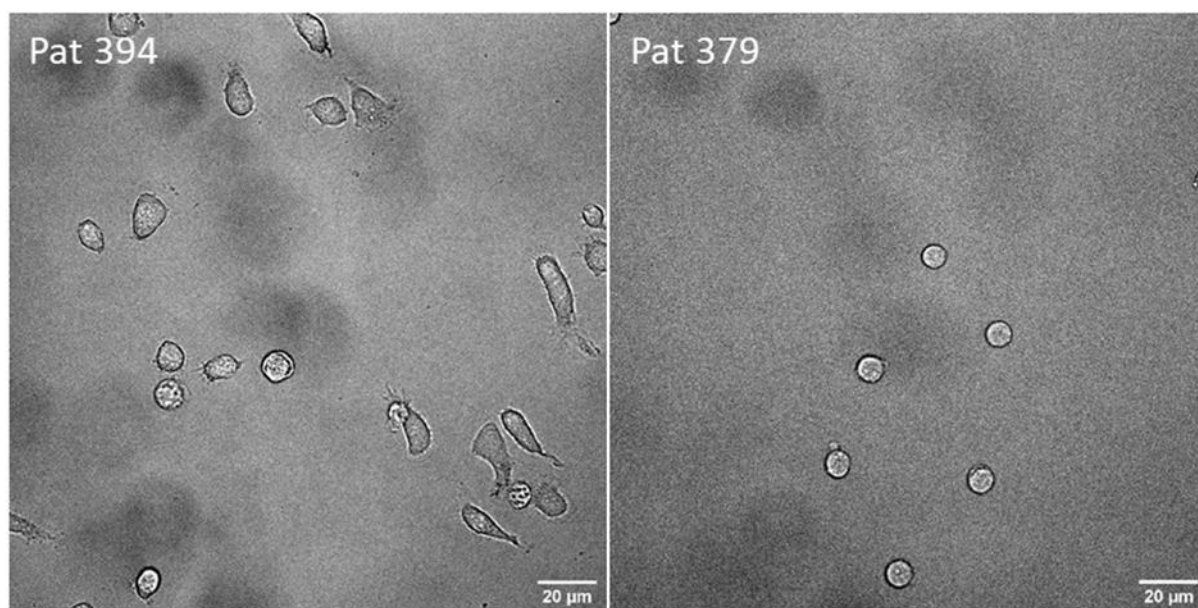


Figure 25 - Bright-field image of multiple myeloma cells of patient 394 and patient 379. For patient 394 most of the cells showed an elongated cell morphology with an average diameter $12.3 \pm 3.7 \mu\text{m}$ (s.d.) (n=10) while most of patient 379 myeloma cells were round with an average diameter of $8.1 \pm 0.7 \mu\text{m}$ (s.d.) (n=10).

Quantification of the different receptors (Figure 26) resulted in a mean cluster density \pm standard error (s.e.) of 19.0 ± 3.4 (s.e.) for patient 379 (n=6) and 16.4 ± 4.0 (s.e.) cluster per μm^2 for patient 394 (n=9) for CD138. Only the homogeneously distributed basal area in the middle of the cell was used for analysis. Additionally, a high variability in CD138 expression was observed for patient 394 ranging between 5.4 and 44.4 clusters per μm^2 . BCMA expression was slightly reduced for patient 379 with 2.1 ± 0.2 (s.e.) (n=5) compared to 3.7 ± 0.6 (s.e.) cluster/ μm^2 for patient 394 (n=14). In contrast, patient 379 showed an increased SLAMF7 expression with high variance in cluster density compared to patient 394 (7.2 ± 2.1 (s.e.) (n=7) and 3.3 ± 0.4 (s.e.) (n=9), respectively). Also, while all myeloma cells of patient 379 were CD19 positive with 10.6 ± 2.8 (s.e.) (n=11) cluster/ μm^2 , the cells of patient 394 (n=6) could not be separated from unspecifically-bound background signal with 1.0 ± 0.1 (s.e.) cluster/ μm^2 . All cells of patient 379 were highly positive for CD20 with cluster densities of 41.8 ± 8.6 (s.e.) (n=8) while only some small percentage of patient 394-cells were positive and included in the statistics (6.6 ± 2.6 (s.e.) cluster/ μm^2 (n=8)). Therefore, at least two cell populations, being CD20⁺ and CD20⁻, were assumed for patient 394.

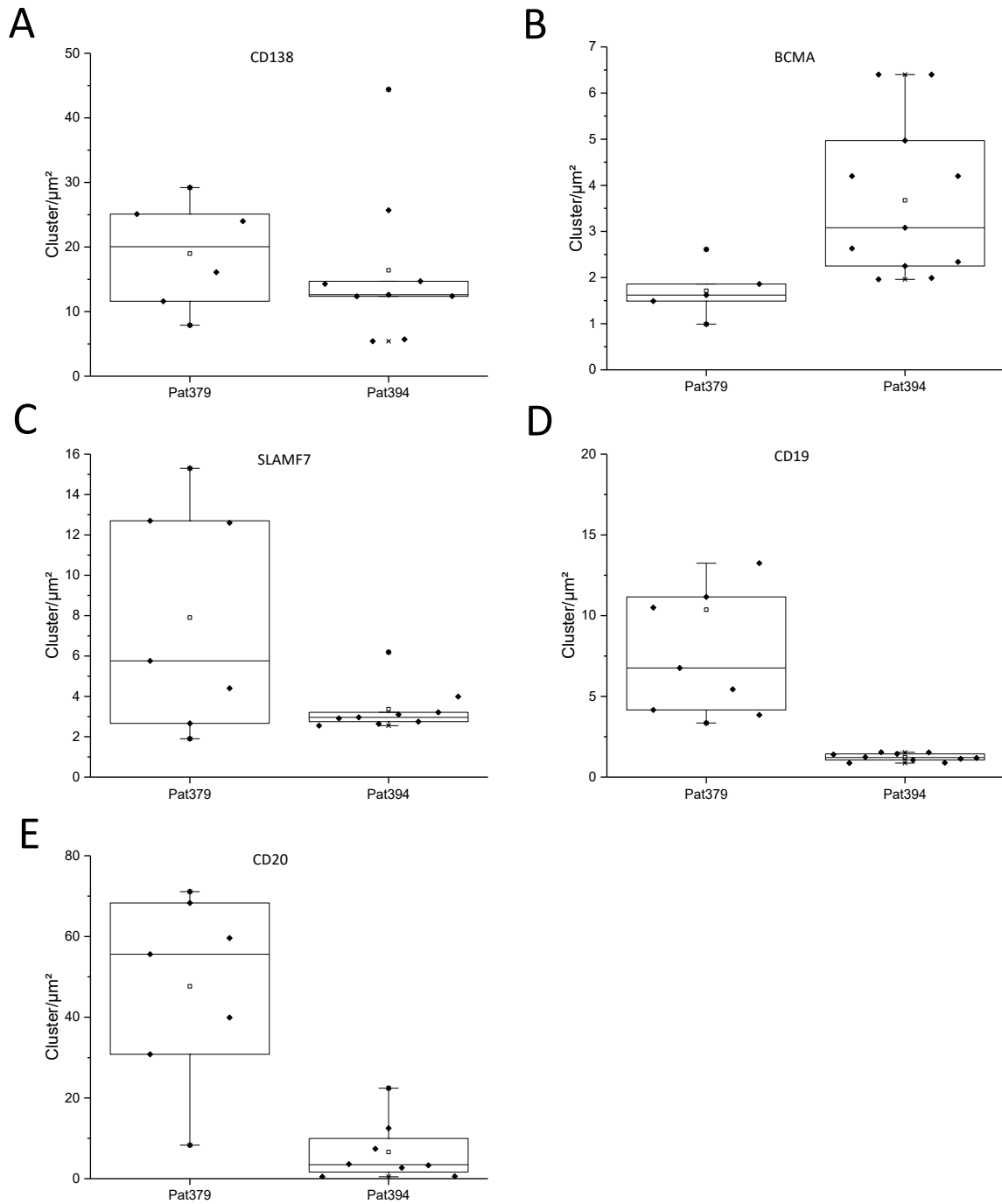


Figure 26 - Quantitative analysis of CD138 (A), BCMA (B), SLAMF7 (C), CD19 (D) and CD20 (E) on multiple myeloma cells of patient 379 and 394. Quantification was performed with Locan with $\epsilon = 20$ nm and MinPts = 3. Each boxplot represents the clusters per μm^2 of one individual antibody with each dot representing a single analyzed cell.

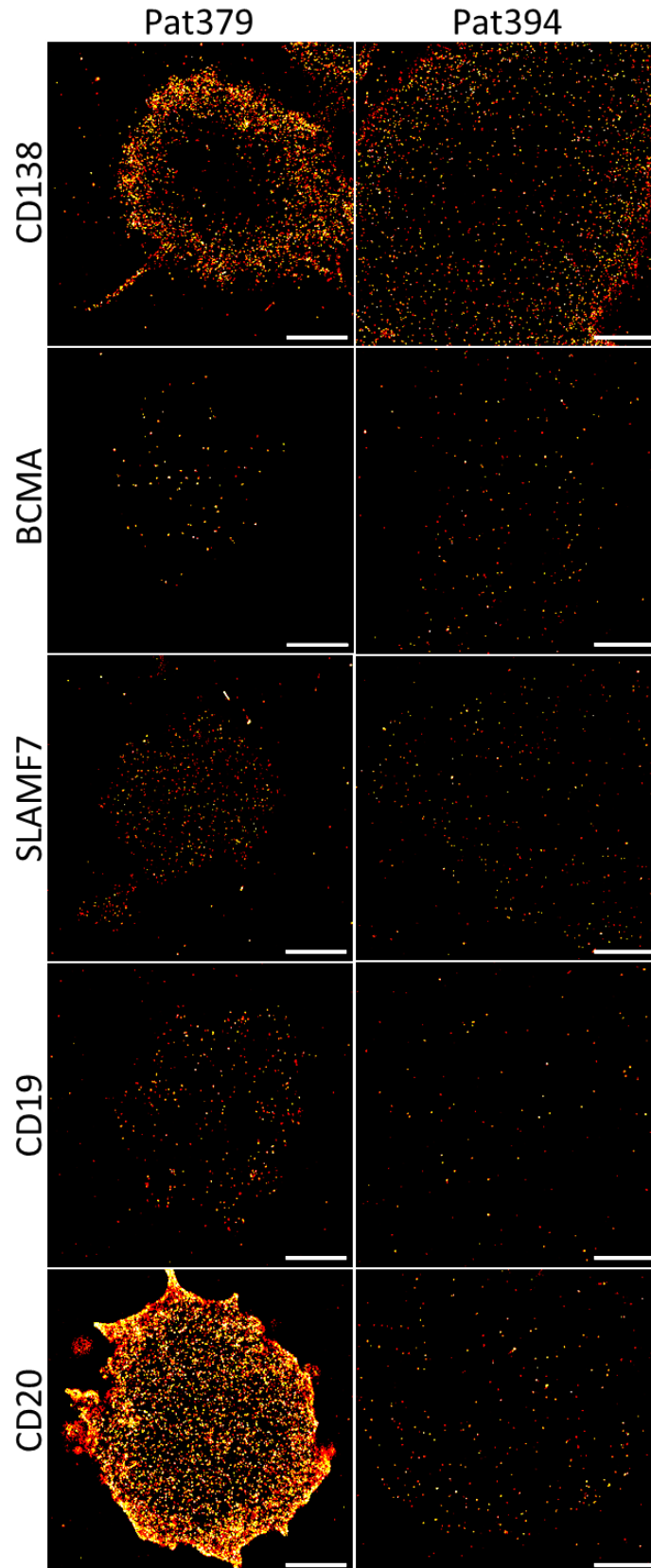


Figure 27 - Representative *d*STORM images of the basal membrane of multiple myeloma cells for patient 379 and 394 stained with different antibodies. Cells were stained according to the live cell staining protocol for either CD138, BCMA, SLAMF7, CD19 or CD20 before the basal membrane was imaged via *d*STORM. Scale bars: 2 μm.

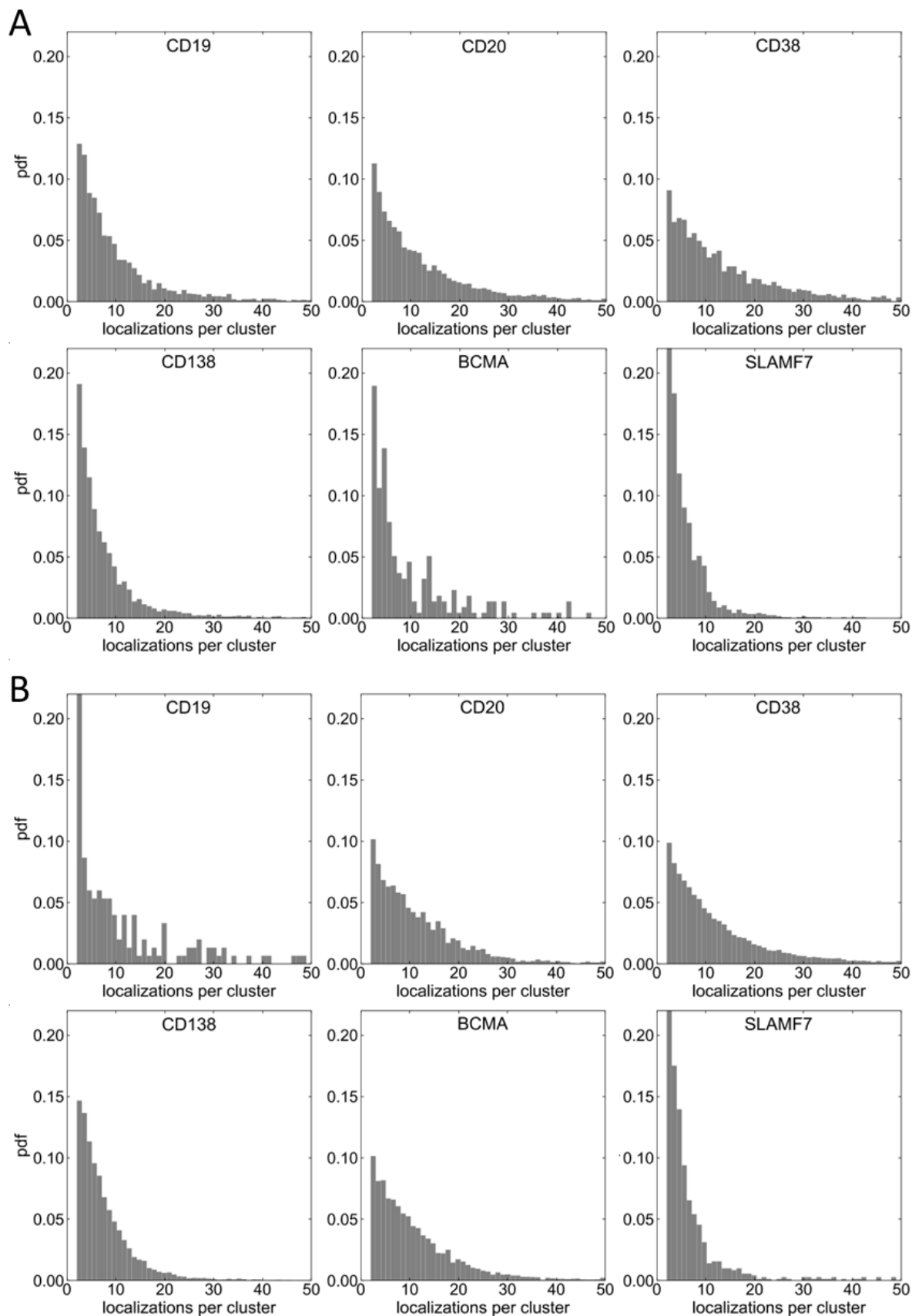


Figure 28 - Probability density functions (PDF) of the localizations per cluster for CD19, CD20, BCMA and SLAMF7 on multiple myeloma cells for patient 379 (A) and patient 394 (B). While CD20 and CD38 indicate a dimeric distribution of the receptor for both patients, a dimeric trend for BCMA is only apparent for patient 394 and for CD19 only for patient 379. For SLAMF7 and CD138 both patients demonstrate a monomeric receptor distribution.

Comparing the PDF of the localizations per cluster for patient 379 (Figure 28 A) and patient 394 (Figure 28 B) indicate a predominantly monomeric distribution for SLAMF7 and CD138. For CD20 and CD38 a dimeric distribution for both patients is hypothesized, while BCMA showed a dimeric distribution for patient 394 and a monomeric distribution for patient 379 respectively. For CD19 a mixture of monomeric and dimeric receptors was observed for patient 379 while patient 394 demonstrated a strongly fluctuating trend, possibly caused by low binding events and the missing statistics. The representative mean localizations per cluster are listed in Table 13.

Table 13 - Mean localizations per cluster \pm standard error for different analyzed receptors of multiple myeloma cells of patient 379 and 394.

Patient	Mean localizations per cluster \pm standard error					
	CD19	CD20	CD38	CD138	BCMA	SLAMF7
379	10.6 \pm 0.8	12.1 \pm 1.3	15.7 \pm 1.0	8.1 \pm 0.6	12.6 \pm 1.2	6.6 \pm 0.4
394	18.8 \pm 1.9	11.8 \pm 1.0	13.3 \pm 0.9	8.9 \pm 0.3	13.4 \pm 0.5	7.8 \pm 0.4

3.3.3 Influence of knock-out and point mutations on the receptor expression of multiple myeloma cells

Multiple Myeloma is a quite diverse disease with various subpopulations that exhibit different genomic alterations. Genomic analyses demonstrate that specific mutations in the *TP53* and *KRAS* genes are most prevalent and result in loss of cell proliferation inhibition. In this part, two different wild type and three different modified cell lines were compared for their expression profiles of clinically crucial receptors. The cells were provided and stained according to the live cell staining protocol by Cornelia Vogt of the Internal Medicine II of the University Hospital Würzburg.

The wild type AMO1 multiple myeloma cell line was compared to UMC901, a CRISPR/Cas9 engineered AMO1 cell line that harbors bi-allelic alterations to *TP53*: *TP53* del/mut (Munawar et al. 2019). Representative *d*STORM images of CD38, CD138, BCMA and SLAMF7 are shown in Figure 30 and their respective quantification is listed in the boxplots (Figure 29 A-D). UMC901 showed a clear increase in CD38 with mean cluster densities \pm standard error (s.e.) of 51.5 \pm 5.7 (s.e.) (n=15) compared to 36.4 \pm 4.2 (s.e.) cluster/ μm^2 for AMO1 wild type (n=11). Additionally, the mutant

demonstrated greater variances in receptor expression compared to the wild type. Highly accumulated CD138 at the outer basal attachment area is visible for both cell lines. However, long stress fibers highly enriched with CD138 are more prominent in the *TP53* mutant. Therefore, due to the difficult comparability between these fibers, only the homogeneously attached region was used for quantification of CD138 as described in 3.3.2. Quantification of these receptors demonstrated a slightly higher cluster density of 15.5 ± 2.4 (s.e.) for UMC901 (n=7) compared to 9.8 ± 1.3 (s.e.) cluster/ μm^2 for AMO1 (n=9). In contrast, BCMA showed a slightly reduced cluster density for UMC901 (0.6 ± 0.1 (s.e.)) (n=7) compared to AMO1 (1.1 ± 0.1 (s.e.)) cluster/ μm^2 (n=6), which is much less than observed for CD38 and CD138, but was clearly higher on the basal cell surface compared to the glass surface. No real difference in cluster densities was observed for SLAMF7 (UMC901: 5.7 ± 0.8 (s.e.) (n=8) and AMO1: 5.0 ± 0.6 (s.e.) cluster/ μm^2 (n=5)). The knock-out of the tumor suppressor gene *TP53* resulted in altered receptor quantity for most receptors and additionally changed cell morphology, which was indicated by elongated stress fibers enriched with CD138.

Additionally, two single point mutations of the OPM2 myeloma cell line were investigated. Both point mutations are located in the KRAS protein important for cell growth and survival. The point mutation, termed LG8, contains an alanine at position 12 instead of glycine (G12A), resulting in a constitutive activation of the growth signal. LG9 has a threonine at position 146 instead of alanine (A146T) causing conformational changes of the protein (Poulin et al. 2019). The expression of CD38, CD138, BCMA and SLAMF7 was again imaged via dSTORM (Figure 31), quantified and compared with wild type OPM2 (Figure 32).

CD38 expression on wild type OPM2 cells (Figure 31 A) with mean cluster densities \pm standard error (s.e.) of 17.9 ± 1.6 (s.e.) (n=12) was slightly reduced compared to LG9 cells with 24.8 ± 2.5 (s.e.) (n=15), but greater than for LG8 with 12.2 ± 1.5 (s.e.) cluster/ μm^2 (n=16). Due to the unequal expression of CD138 (Figure 31), again only the homogeneously distributed basal membrane was used for the quantification. No significant change in CD138 receptor expression was observed, even though LG9 showed a higher variability of the expression pattern (Figure 32 B). With cluster densities of 6.6 ± 0.5 (s.e.) for the OPM2 wild type (n=11), 6.7 ± 0.4 (s.e.) for LG8 (n=10) and 9.4 ± 1.1 (s.e.) cluster/ μm^2 for LG9 (n=11), CD138 seemed to be less

present on multiple myeloma cells than e.g. CD38. However, a lot of CD138 is accumulated in the filopodia, therefore falsifying the amount of detected CD138. In contrast, a reduction of BCMA expression of nearly 50% was observed for LG8 cells with cluster densities of 5.9 ± 0.3 (s.e.) (n=11) compared to 10.8 ± 1.2 (s.e.) (n=8) and 10.3 ± 1.3 (s.e.) cluster/ μm^2 (n=7) of the wildtype and LG9 cells, respectively (Figure 32 C). For SLAMF7 (Figure 32 D), a visible reduction is indicated on LG8 cells with a cluster density of 6.0 ± 0.8 (s.e.) (n=8) as well as for LG9 with 8.8 ± 1.6 (s.e.) (n=8) compared to the OPM2 wild type with 11.8 ± 0.8 (s.e.) cluster/ μm^2 (n=11).

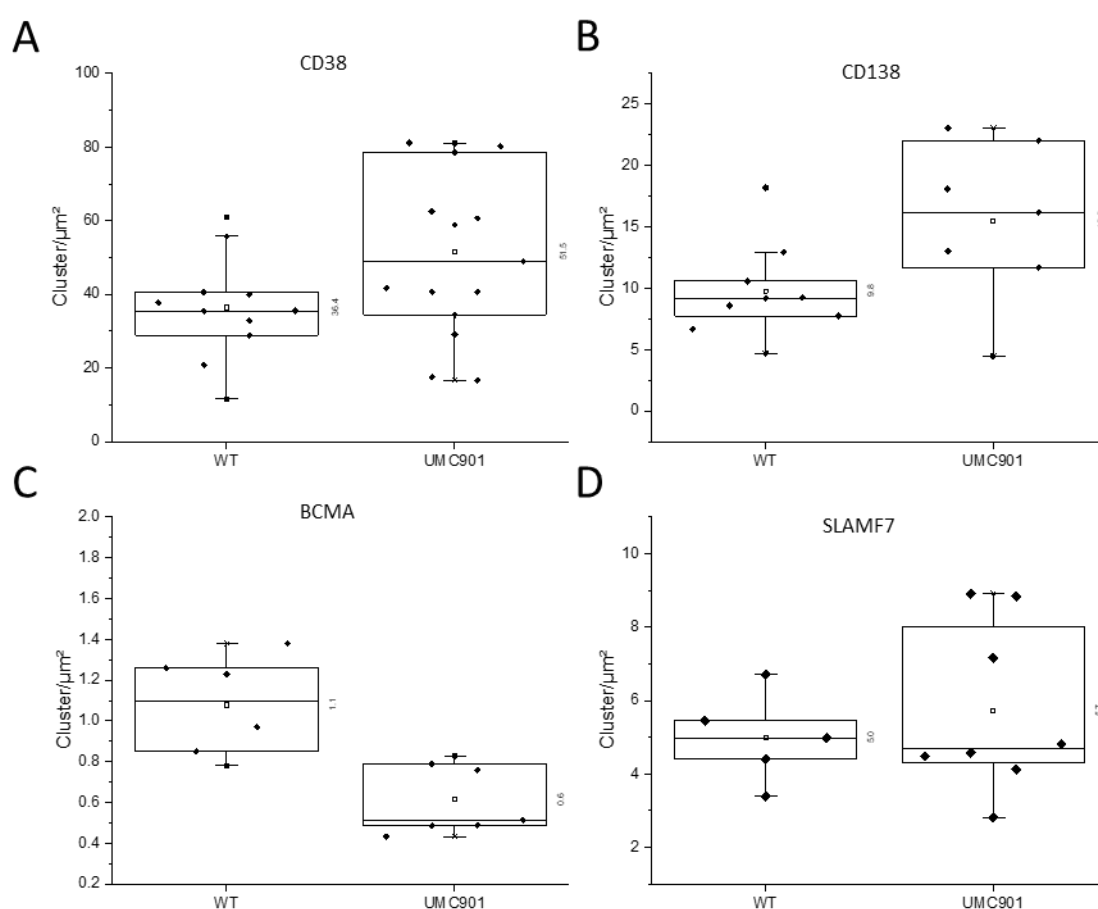


Figure 29 - Quantification of CD38 (A), CD138 (B), BCMA (C) and SLAMF7 (D) receptor expression for AMO1 WT and CRISPR/Cas9 *TP53* deleted AMO1 (UMC901) cells. Quantification was performed with Locan with $\epsilon = 20$ nm and MinPts = 3. Each boxplot represents the clusters per μm^2 of one individual antibody with each dot representing a single analyzed cell.

Both point mutations demonstrated different cluster quantities, although the same protein was affected. LG9 revealed increased CD38 expression while other receptors seemed to be mostly unaffected. In contrast, the G12A KRAS mutation in LG8 had a much greater impact, leading simultaneously to altered CD38, BCMA, and SLAMF7 expression.

Most importantly, an altered CD38 expression was observed for the two mutants of OPM2 as well as for the AMO1 mutant, while CD138, BCMA and SLAMF7 were only affected in some cases.

As in patients 379 and 394, the mean localizations per cluster for CD38 ranged from 16.6 to 22.6, suggesting multiple antibodies bound to a single receptor (Table 14). For CD138 mean localizations per cluster showed equal amounts within the same cell lines. However, with ~22 localizations per cluster OPM2 cell lines demonstrated higher quantities than AMO1 cell lines ranging between 13.4 and 15.6 localizations per cluster. BCMA showed the highest mean localizations per cluster \pm standard error (s.e.) for the OPM2 WT with 20.1 ± 0.3 (s.e.) and for LG9 with 15.6 ± 0.2 (s.e.) localizations per cluster. The AMO1 cell lines again demonstrated lower localizations per cluster with 12.5 ± 0.6 (s.e.) for the WT and 15.4 ± 0.8 (s.e.) for UMC901. A monomeric trend is observed for SLAMF7 for AMO1 WT (8.5 ± 0.2 (s.e.)) and UMC901 (10.4 ± 0.3 (s.e.)) cells, with no apparent difference between both cell lines. In contrast, twice as many localizations per cluster were detected for OPM2 WT compared to LG8 (12.2 ± 0.1 (s.e.) to 6.8 ± 0.2 (s.e.)), which was quite similar to LG9 (8.4 ± 0.1 (s.e.))

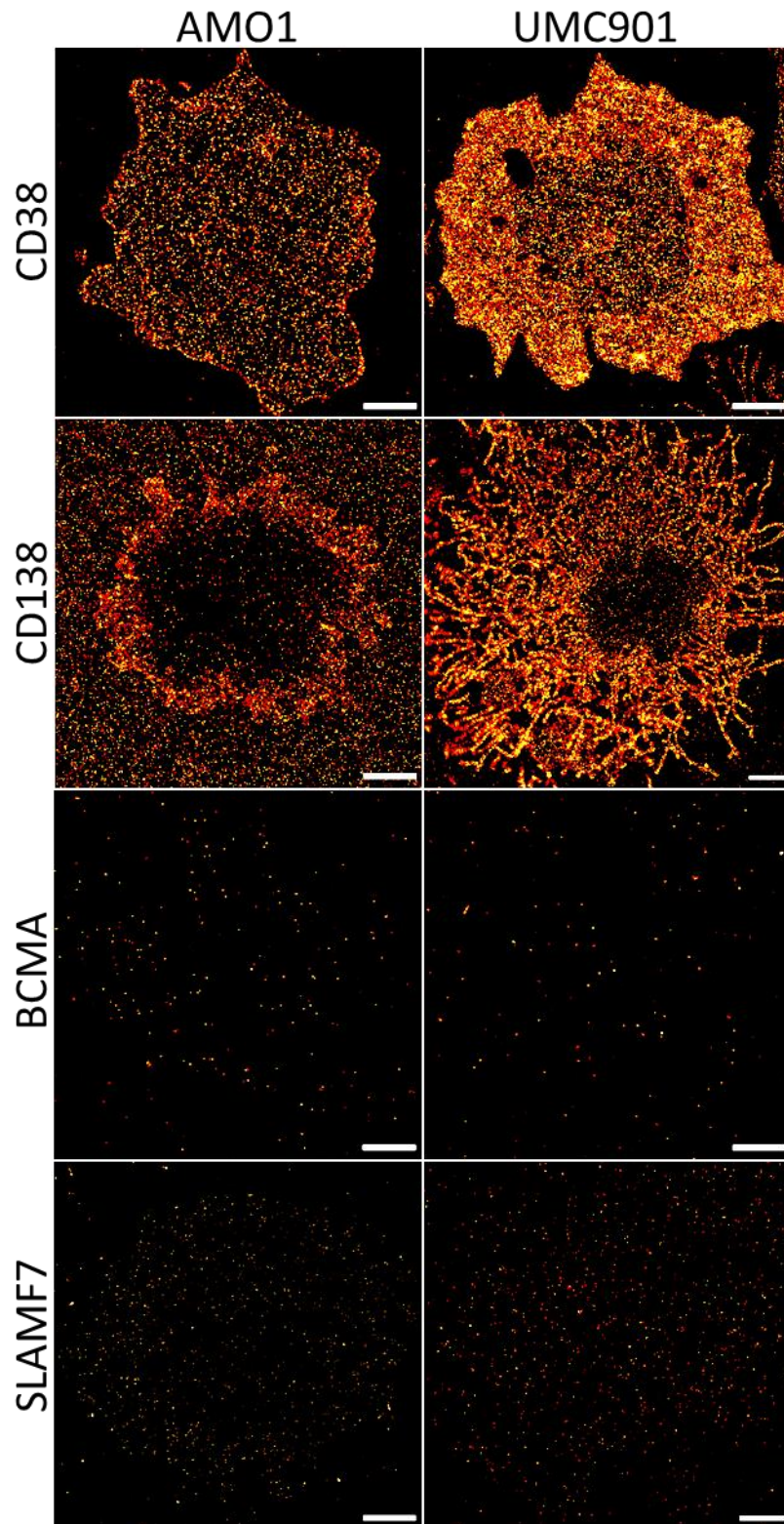


Figure 30 - Representative dSTORM images of the basal membrane of AMO1 and CRISPR/Cas9 *TP53* deleted AMO1 (UMC901) cells stained with different AF647 coupled antibodies. Cells were stained according to the live cell staining protocol for either CD38, CD138, BCMA or SLAMF7 before the basal membrane was imaged via dSTORM. Scale bars: 2 μ m.

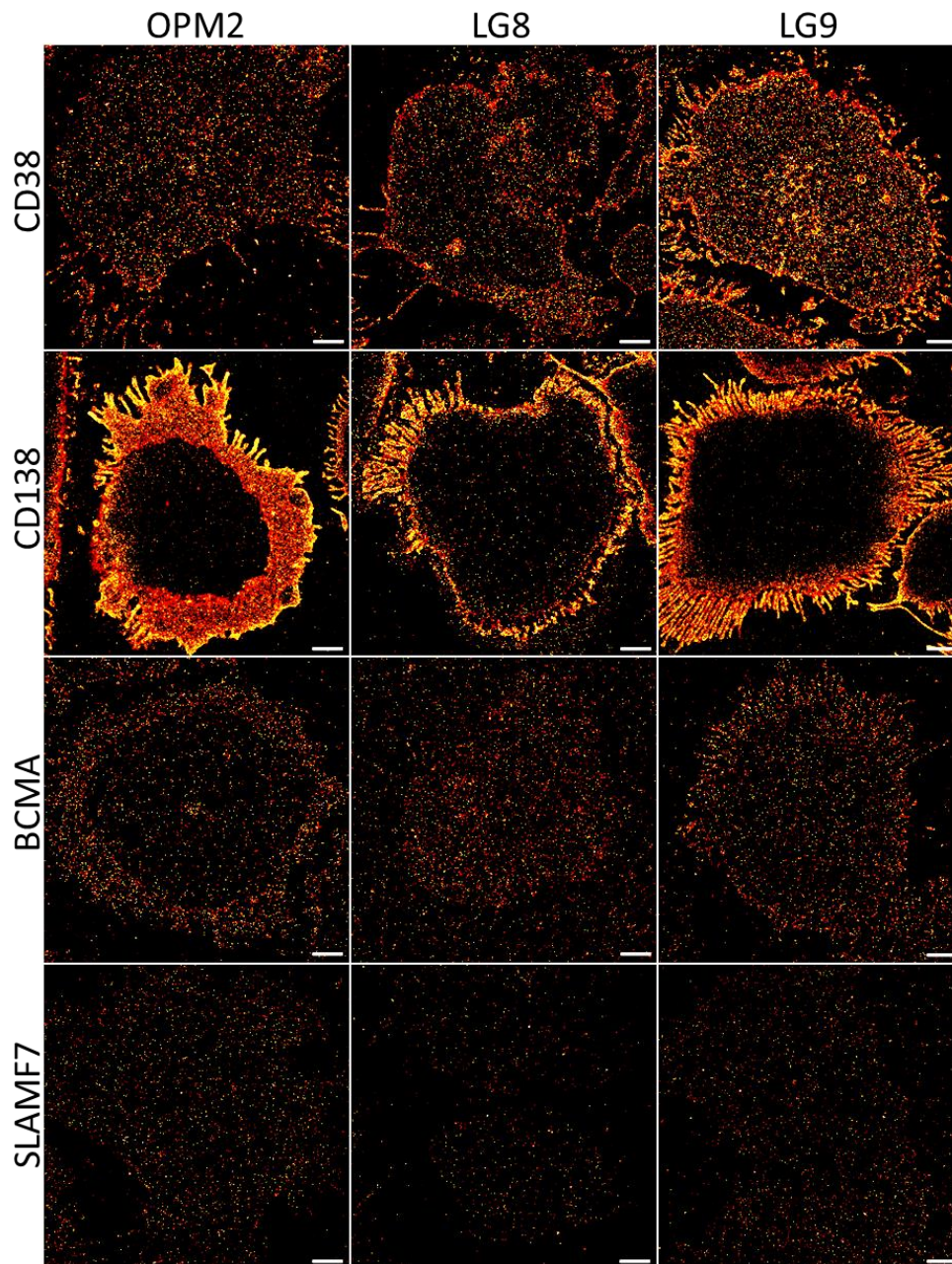


Figure 31 - Representative dSTORM images of the basal membrane of OPM2 (WT) and point mutated KRAS OPM2 cells, LG8 and LG9, stained with different AF647 coupled antibodies. Cells were stained according to the live cell staining protocol for either CD38, CD138, BCMA or SLAMF7 before the basal membrane was imaged via dSTORM. Scale bars: 2 μ m.

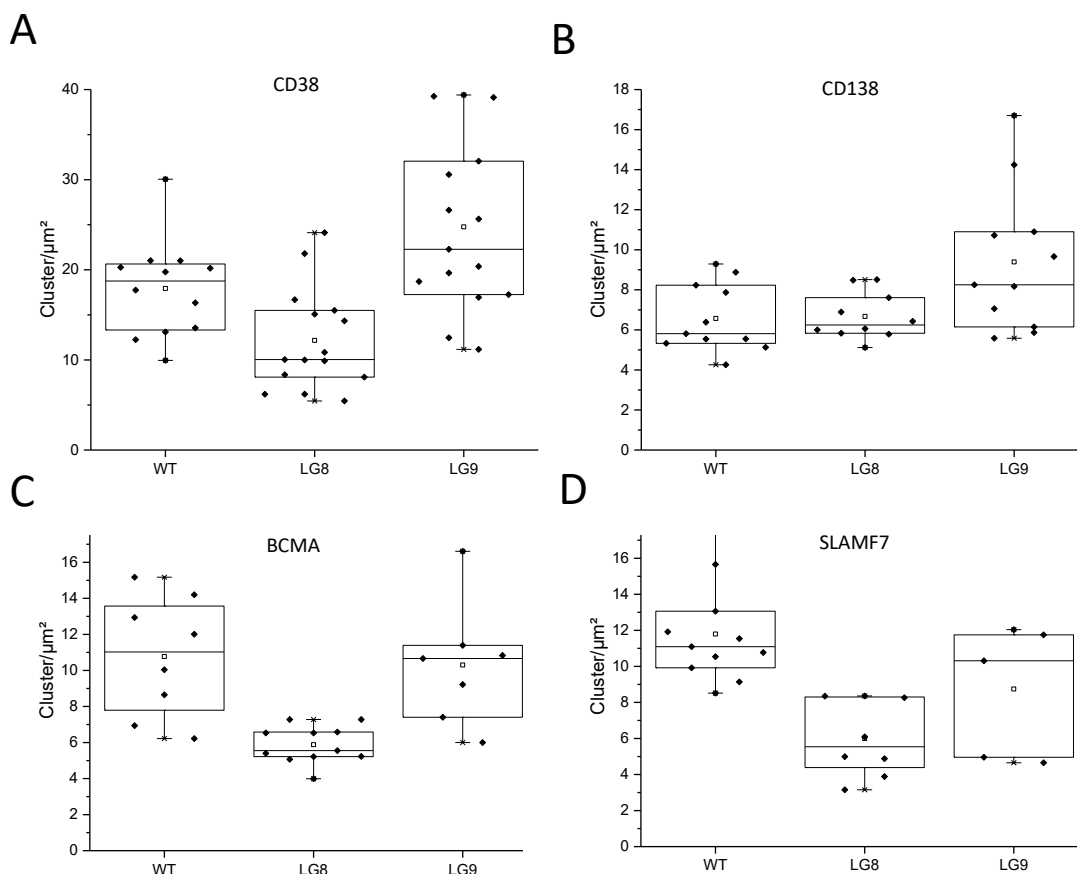


Figure 32 - Quantification of CD38 (A), CD138 (B), BCMA (C) and SLAMF7 (D) receptor expression on OPM2 (WT) and point mutated KRAS OPM2 cells, LG8 and LG9. Quantification was performed with Locan with $\epsilon = 20$ nm and MinPts = 3. Each boxplot represents the clusters per μm^2 of one individual antibody with each dot representing a single analyzed cell.

Table 14 - Mean localizations per cluster \pm standard error for different analyzed receptors of OPM2 and AMO1 wild type (WT) and their respective mutated cell lines.

	AMO1		OPM2		
	WT	UMC901	WT	LG8	LG9
CD38	19.9 ± 0.2	16.6 ± 0.2	17.8 ± 0.1	22.6 ± 0.2	20.9 ± 0.2
CD138	15.6 ± 0.3	13.4 ± 0.2	20.4 ± 0.4	22.0 ± 0.3	22.3 ± 0.4
BCMA	12.5 ± 0.6	15.4 ± 0.8	20.1 ± 0.3	18.4 ± 0.2	15.6 ± 0.2
SLAMF7	8.5 ± 0.2	10.4 ± 0.3	12.2 ± 0.1	6.8 ± 0.2	8.4 ± 0.1

3.4 Quantification of FLT3 on cell lines and primary patient cells

As second clinical example, analysis of FLT3, a receptor often mutated in AML, was performed. Quantification was done on MV4-11 midostaurin-resistant (MID⁺) and -sensitive (MID⁻) cell lines as well as on MOLM-13 MID⁺ and MID⁻ cell lines, and on a primary AML sample, which were kindly provided by Dr. med. Sabrina Kraus and Andoni Garitano-Trojaola from the Center for allogeneic stem cell therapy of the University Hospital Würzburg. MID⁺ cell lines MV4-11 and MOLM-13 were generated by cultivating cells with serially increasing concentrations of midostaurin by 10 nM weekly to 50 nM. Cells were harvested and adjusted to 1×10^6 cells/ml until a sufficient MID⁺ cell number was reached. Based on receptor aggregation visible on all cell lines, receptor quantities were estimated by dividing the localizations density (localizations/ μm^2) by 9, as described in chapter 3.1.

In initial experiments, MV4-11 MID⁺ and MID⁻ as well as MOLM-13 MID⁺ and MID⁻ cells were used to establish protocols and to determine whether there are fundamental differences in FLT3 expression or distribution between cell lines that are resistant and sensitive to the tyrosine-kinase-inhibitor midostaurin. Staining with an FLT3-AF647 antibody was performed according to the live cell staining protocol to preserve epitopes and possibly identify oligomers via dSTORM image acquisition. For MOLM-13 MID⁺ cells FLT3 clusters were visible and some FLT3 aggregations for MV4-11 MID⁺ cells (Figure 33 A). Although the MOLM-13 MID⁻ cells showed a more homogeneous distribution and thus distinct changes to MID⁺ cells, this difference was not so obvious for the MV4-11 MID⁺ and MID⁻ cells (Figure 33 A). However, MV4-11 and MOLM-13 cell lines showed different receptor oligomerization states between MID⁺ and MID⁻ types, with receptor densities remaining the same for MV4-11 cells, but not for MOLM-13 MID⁻ cells, which were greatly reduced (Figure 33 B). Cluster analysis using DBSCAN algorithm with $\epsilon = 20$ nm and MinPts = 3 showed mean estimated receptor densities \pm a standard error (s.e.) of 23.3 ± 3.6 (s.e.) (n=5) and 7.1 ± 2.1 (s.e.) (n=6) receptors/ μm^2 for MOLM-13 MID⁺ and MID⁻ cells, respectively (Figure 33 B). For MV4-11 MID⁺ and MID⁻ cells mean receptor densities \pm standard error of 14.5 ± 1.9 (s.e.) (n=9) and 17.1 ± 2.4 (s.e.) (n=9) receptors/ μm^2 were observed. Additional stoichiometric analysis of the localizations per cluster confirmed the observed FLT3 aggregations for MOLM-13 MID⁺ cells compared to MID⁻ (Figure 33 C blue and light blue line), which could not be validated for MV4-11 MID⁺ cells (Figure 33 C black line). For MV4-11 MID⁺ only a second dimeric population is observed at 11 localizations per

cluster (Figure 33 C, black line), whereas MV4-11 MID⁻ cells (Figure 33 C, gray line) demonstrated FLT3 clustering as for the MOLM-13 MID⁺ cells (Figure 33 C, blue line).

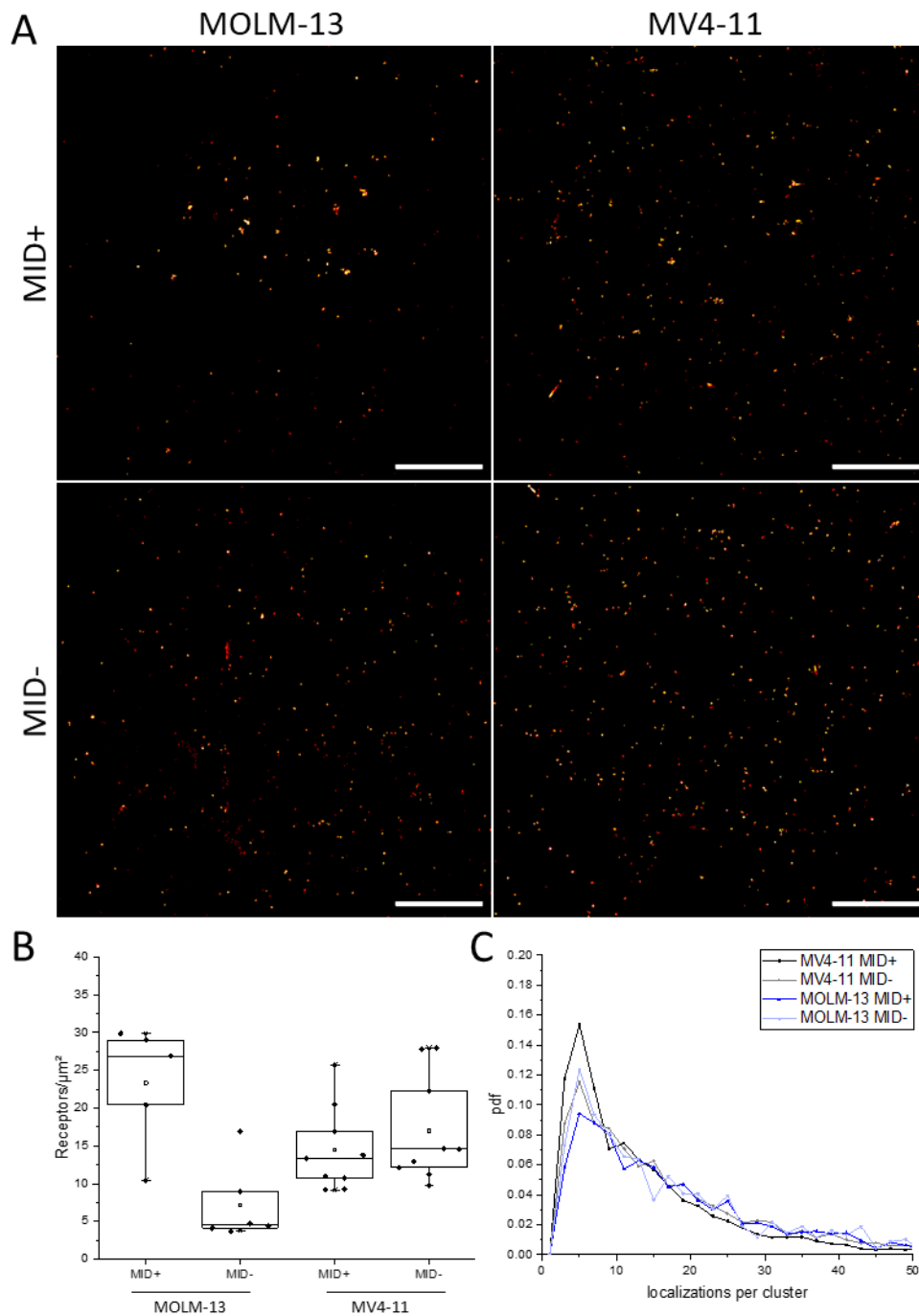


Figure 33 - Representative dSTORM images of anti-FLT3-AF647 on MV4-11 and MOLM-13 midostaurin resistant (MID⁺) and sensitive (MID⁻) cells, the respective receptor densities (A) and localization densities per cluster (B). For both cell lines clear differences between MID⁺ and MID⁻ cells either in relation to their FLT3 receptor expression (MOLM-13) or assembly (MV4-11) were observed. Scale bars: 2 μm .

Interestingly, the localizations per cluster are for MV4-11 MID⁺ cells in contrast to the clearly observed clustering of antibodies on the basal membrane. Furthermore, a

dimeric subpopulation can be suspected for all four cell types, which is evident from a peak in the pdf at ~ 10 localizations per cluster as observed previously (Figure 15 B).

Next, primary AML cells from a patient being MID⁺ for FLT3 expression were analyzed (Figure 34 A). Most of the cells demonstrated high autofluorescence complicating the quantification approach (Figure 34 A white arrow). In this case, FLT3 expression was

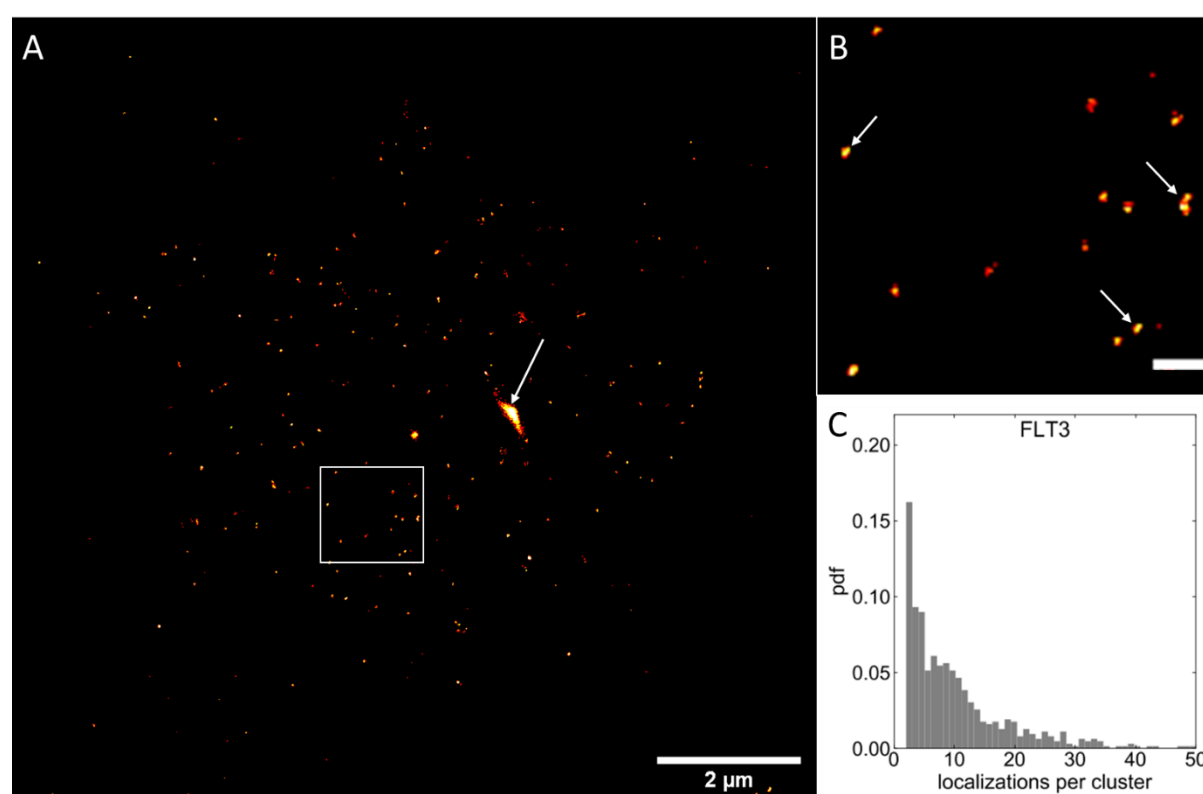


Figure 34 - Representative *d*STORM image of FLT3 detected on a primary AML-cell of a patient being resistant to midostaurin (A) and the corresponding localizations per cluster (C). Most of these cells demonstrated strong autofluorescence, visible in the reconstructed image (A). Magnification of the stained cells (B) showed antibodies being in proximity suggesting a present monomeric and dimeric receptor population, which is confirmed by a second population being visible at ~ 10 localizations per cluster (C). Scale Bar magnification: 200 nm.

homogeneously distributed with antibodies being in close proximity, suggesting a dimeric FLT3 population present (Figure 34 B white arrows). This was also confirmed by stoichiometric analysis, indicating a second population with about twice as many blinking events as for the monomers, showing a distribution equivalent to the dimeric receptors analyzed in chapter 3.1 at ~ 10 localizations per cluster (Figure 34 C). Compared to the MV4-11 and MOLM-13 MID⁺ and MID⁻ cell lines the mean receptor density \pm standard error was with 4.4 ± 0.7 (s.e.) ($n=9$) receptors per μm^2 strongly reduced for FLT3 on the primary patient cells.

4 Discussion

4.1 Stoichiometric receptor quantification on cell lines

In the first part of this thesis, a single molecule-sensitive quantification protocol for dSTORM on Jurkat T cells was established, which was applied for all quantitative analysis later on. Firstly, self-labeled monoclonal antibodies were used to ensure a degree of labelling ranging between 2-4. Detecting specific antibody binding events, especially when they are sparse, is one of the most limiting steps for stoichiometric and quantitative analysis. Poorly labeled antibody populations (< 1.5 dyes per protein on average) will reduce the amount of detected receptors on the surface as not every antibody will carry a fluorophore and therefore only block the epitope. However, when an antibody carries too many fluorophores, unspecificity is increased due to charges or blocked binding sites. This will not only drastically enhance unspecific binding to the glass surface but also to the cell membrane being fatal for low or non-expressed targets. In addition, small nanocluster subpopulations may not be detected because either unlabeled antibodies block them or unspecific antibodies increase the detected monomeric population. Titration of each antibody for different staining protocols is an important first step to ensure saturation of all free binding epitopes and to minimize unspecific binding events by using adequate amounts of antibody as shown by Ralph Götz from our department (Götz 2020). Epitope accessibility is another limitation for precise quantification. Due to the size of antibodies of approximately 10-15 nm, close epitopes won't be accessible for protein binding (Reth 2013). Testing different antibody clones that have higher affinity to a specific binding epitope or bind to more accessible epitopes, e.g., further from the plasma membrane, can improve stoichiometric information. Typically, most antibodies used in clinical approaches like flow cytometry perform best and show only few unspecific binding events as they are well characterized as their production is tightly controlled. It should also be considered that, mainly due to accessibility issues, only a subset of the addressed receptors could be detected. However, this is no drawback for quantification of membrane receptors in case of personalized immunotherapy as these receptor numbers demonstrate the targetable molecules for monoclonal antibody therapy, when the same antibody clone is used or the therapy is directed against the same epitope.

The various analyzed receptors (Figure 10) showed predominantly homogeneous distribution on the cell surface, with strong clustering visible only for CD3 on the basal

membrane. CD3 is a T cell marker and important for activation of T cells. When activated, different CD3 subunits form a complex together with the T cell receptor (TCR) resulting in an aggregation of CD3 molecules. On primary T cells, a homogeneous distribution is typical with clusters occurring upon activation (Rossboth et al. 2018). The Jurkat cell line is an immortalized T cell line self-producing IL-2, an important cytokine for the activation of T cells causing Jurkat T cells to be at least partially activated and CD3 clusters appearing (Pawelec et al. 1982). Besides a homogeneous distribution and strong clustering, small oligomers in the range of 10-50 nm are challenging to detect and distinguish on the cell membrane. Small clusters consisting of two anti-CD69 antibodies lead to the assumption that antibodies have the ability to bind adjacent molecules despite their size (Figure 10). Here, the linkage error of ~10 nm per antibody may play a beneficial role helping to detect two nearby antigens by their binding epitopes with labeled antibodies via super-resolution techniques.

To prove this theory, two-color *d*STORM was applied due to its high sensitivity and resolution. Using the same antibody but coupled to two different dyes in a 50:50 ratio should lead to co-localization of ~50% of the total population under optimal conditions. Nevertheless, it is known that only AF647 gives reliable quantitative information for receptor analysis compared to AF532 ((Götz 2020)). In addition, the localization precision of the second color (in this case AF532) is often worse, more nonspecific binding events are detected, and the switching behavior is usually not satisfactory within the same buffer system (Table 10). The amount of co-localization under optimal conditions was investigated by using a simplified system in which cells were labeled with an anti-CD45-AF647 antibody additionally stained with a secondary gam-AF532. Due to the high mobility of the cell membrane of living cells, artificial clusters were induced by the secondary antibody for incubation times greater than 15 minutes even though incubation was done on ice (Figure 12). Despite the low incubation time of the secondary F(ab)₂ antibody, primary antibodies with secondary antibodies, as well as secondary antibodies without a primary binding partner and vice versa, could be observed reducing the MOC to ~0.5. Fixing cells prior to staining will drastically reduce detected receptors on the surface due to cross linking of proteins and was therefore avoided. Analysis of these two-color images lead to a MOC of ~50% of all detected antibodies. This low coefficient could be explained by unspecific binding of the secondary antibody, some antibodies statistically having no dye, destruction of the fluorophore due to high laser powers, or the not perfectly suited switching buffer for

both dyes. Furthermore, these results are consistent with PALM measurements, which also detect only about 60% of the total receptor population (Durisic et al. 2014). Here it's assumed that some of the fluorescent protein mEos2 is not photo-converted or gets destroyed upon irradiation with the 405 nm laser. Considering that under these idealized conditions only half of the antibodies demonstrated overlapping primary and secondary antibody signals, a 100% homodimeric receptor may show overlap for only 25% of the bound antibodies. Assuming oligomeric receptors existing in a background of monomers, an average Manders overlap coefficient of 0.21 (Figure 13 B) for CD69 is close to the idealized conditions (Sharma et al. 2004). Due to the heterogeneity of the cells, the mean Manders coefficient of CD69 is slightly lower at 0.14 (Table 9). However, the monomeric receptor CD11a, with similar expression densities on Jurkat T cells, did not show any co-localization, which indicates the presence of multimeric CD69. The heterodimeric receptor LFA-1 (CD11a/CD18) showed a mean MOC of 0.26, which is 50% lower than expected when compared to the experiment where the maximum achievable Manders coefficient was determined (Figure 12 & Table 9). Since the binding epitopes of the two antibodies are only 5 nm apart, steric hindrance of the antibodies is possible (Sen et al. 2018). However, minding all these limiting factors, detection of adjacent binding sites is possible for a huge number of molecules. Using Ripley's h-function to detect non-randomly distributed clustering effects (Figure 14) worked well for larger clusters such as CD3, which are also clearly visible in the images. However, when it comes to small oligomers, especially dimers, no difference to a randomly distributed localization cluster size is apparent. This is caused by the ratio of present monomeric and dimeric receptors on the one hand and by small oligomers still being below the resolution limit of *d*STORM on the other hand. Therefore, the localization cluster size for monomers and small oligomers is identical in most cases and Ripley's h-function not suited for detection of those. In contrast to this resolution issue, localization data gathered from *d*STORM image acquisition contains coordinates of all detected single "blinking" events. Due to stochastic photoswitching of AF647, detection of multiple localizations for one antibody occurs before the fluorophore is irretrievably destroyed. By using clustering algorithms like DBSCAN, these multiple localizations can be grouped and treated as a single antibody when compared to a monomeric reference. Additionally, variances of the degree of labelling are negligible for DOLs between 1 and 4 as previously described (Helmerich, Beliu, and Sauer 2020). For all the analyzed receptors self-labeled antibodies with a

DOL ranging between 2 and 4 have been used, resulting in mean blinking events of ~ 9 localizations per cluster for the monomeric receptors (Table 11). However, due to stochastic photoswitching, instead of a single population of localizations per cluster, several normally distributed clusters are obtained, as can be seen in the probability density functions in Figure 15 A. For all of the monomeric receptors, 3 localizations per cluster started with a value of 0.15 and above and showed only few events over 25 localizations per cluster. In contrast to monomers, dimeric populations showed an increased mean of ~ 16 localizations per cluster (Table 11), also visible by the more widely distributed localization events per cluster (Figure 15 B). Comparison of the blinking statistics revealed differences between monomers and dimers that were not visible by Ripley's h-function. Nevertheless, the probability density functions must be interpreted carefully to decide whether different stoichiometric populations are present or whether the increased localizations per cluster are caused by noise or insufficient photoswitching. The major drawback of antibodies being relatively huge compared to the detected epitopes is an advantage for this approach, as it also avoids quenching FRET effects that typically occur in the 1-10 nm range (Bader et al. 2009; Bajar et al. 2016)

However, the comparison of the receptors analyzed in this part is a simplified model system to establish stoichiometric analysis, since most of these receptor populations should theoretically exist only as monomers or dimers. When only a small subset is oligomerizing or stoichiometrically different oligomers are present, these distinct populations might vanish, not only due to stochastic fluctuations of the blinking statistics but also because of epitope accessibility issues for the antibodies used. This is also visible by the characteristics of the localization density curve. CD69 e.g. should mainly be present as homodimer; still the curve is a mixture of a huge monomeric peak at 5 localizations per cluster and a second peak belonging to the dimeric population at 10 localizations per cluster (Figure 15 B). Nevertheless, especially when comparing the same receptor on cells as it was done for cell cycle synchronization (Figure 16), small changes in receptor assembly are easier to detect and are more reliable.

Compared to primary cells, which are a heterogenic population, cell lines like the used Jurkat T cell line derive from the same subtypes and should therefore be a homogenous population. However, strong fluctuations in receptor expression were detected for all receptors. However, addressed receptors on the apical surface show higher quantities compared to the basal layer caused by the greater accessibility

(Waldchen et al. 2020). Tighter attachment of the cell to the glass surface possibly further lowers the accessibility of the antibody for some cells. Additionally, no cell cycle synchronization was performed prior to staining, resulting in cells being in different cell phases. As seen in Figure 16, the receptor expression profiles vary strongly, and clustering effects are also depending on the cell cycle phase. However, even when synchronized to the S or G0/G1 phase, expression amounts vary. Of note, it was clearly shown that especially activation markers like CD69 show completely different expression quantities depending on the cell cycle phase, whereas the co-stimulatory molecule CD28 was either homogeneously distributed or clustered depending on the phase (Figure 16). This clustering effects are also clearly visible in Ripley's h-function for CD28 control and serum-starved cells with localization cluster sizes of ~60 nm and ~40 nm, respectively, (Figure 17 A) but also in the probability density functions (Figure 17 B) following a more widely distributed trend similar to CD3 (Figure 15 C). For early activation markers like CD69 an upregulation at the beginning of the cell cycle was seen for serum-starved cells as previously described (Naniche, Reed, and Oldstone 1999). Therefore, detecting no CD69 during S-Phase is consistent to an early activation marker as it is not important for late cell cycle phases. The CD28 receptor, on the other hand, is both a co-stimulatory molecule, as well as being important for binding to antigen-presenting cells, making it an essential molecule expressed at all stages of the cell cycle. In addition, observed aggregations of CD69 on FCS-starved cells possibly cause increased activating signals (Figure 17). As seen in both examples, receptor expression and aggregation varied strongly. Therefore, for a better comparability, cell cycle synchronization prior to staining should be considered in future experiments, in particular when using cell lines.

4.2 The Treg receptome

To date, T regulatory cells (Tregs) are poorly understood and quantitative data on receptors or changes in receptor arrangement upon activation are largely missing. During this project, the standard activation with CD3 and an excessive additional CD28 was not applied to investigate changes in receptor expression or assembly, instead the activation with STAR2, an agonist against TNFR2, was chosen due to the additional possibility of *in vivo* expansion of Tregs (Hombach et al. 2007; Chopra et al. 2016).

Main task of the T regulator cells is the suppression of the immune system when activated maintaining a balance between self-tolerance and deleterious activities by immune cells (Corthay 2009). This is also achieved, among other things, by altered receptor expressions. Thus, activated Tregs showed increased CD25 expression (Figure 18), which helps to reduce IL-2 present in solution and thus avoid activation of T cells by this chemokine, as previously reported (Togashi, Shitara, and Nishikawa 2019). In contrast to classical CD3/28 activation, no clustering of CD3 was observed after activation, suggesting an alternative activation mechanism by the STAR2 ligand. CD103 was only slightly reduced during STAR2 activation (Figure 21 B), possibly because of its importance for adhesion to epithelial tissue and cell homing to the intestinal sites. Little is known about the main tasks of this receptor for immune suppression but CD103⁺ Tregs seem to have a strong immunosuppressive activity and tumor infiltrating capabilities (Anz et al. 2011; Chang et al. 2012). However, when CD103 upregulation occurs instead this may also be a byproduct caused by TGF- β highly concentrated in tumor microenvironment (Anz et al. 2011) and help malignancies to proliferate and survive. Upregulation of CD120b and CD134 expression on Tregs is a sign for activation as seen in Figure 19, confirming the successful stimulation by STAR2 (Nagar et al. 2010). Additionally, CD25⁺ CD120b⁺ Tregs have better suppressive capabilities than low or non-expressing Tregs (Chen et al. 2010), whereas CD134 is an important co-stimulatory molecule, which signaling results in reversed suppressive function of Tregs (Kitamura et al. 2009). Additionally, CD134 signaling enables proliferation and survival of Tcons (Kitamura et al. 2009). Therefore, the visible increase in CD134 expression may act as a safety switch to allow an enhanced response to antitumor vaccination (Tay, Richardson, and Toh 2021). Upregulating these receptors will help on the one hand to suppress immune responses but at the same time being able to be turned off by chemokines present in the microenvironment. In addition, CD137 was expressed on STAR2 activated Tregs (Figure 20), which helps cells proliferate and increase their immunosuppressive function (Zhang et al. 2007). Additionally, it was shown that under certain circumstances Tregs could gain effector functions after agonist binding having anti-tumoral effects (Akhmetzyanova et al. 2016). CD279 (or PD-1), which is known as a negative regulatory molecule and an important checkpoint inhibitor by causing reduced immune suppression and proliferation, was lower expressed on activated cells compared to native Tregs, suggesting higher suppressive capabilities on activated

Treg cells (Daraei et al. 2019). Of note, death receptor 3 (DR3) is preferential expressed on activated cells (Figure 20) and can be used to stimulate Treg expansion from their initial 2-10% of the whole CD4⁺ T cell population to 30-35% of all CD4⁺ T cells within 4 days and is therefore a very important receptor to maintain a strong immune suppression (Schreiber et al. 2010). Glycoprotein A Repetitions Predominant (GARP) is also expressed on active T regulator cells (Figure 20) possibly helping to increase their suppressive capability. The possibility to bind TGF- β promotes secretion and activation of this cytokine which has suppressive functions towards effector cells (Tran et al. 2009). GITR in contrast was the only receptor highly expressed and accumulated in big clusters on the cell surface. Its important suppressive function was first discovered when experimental elimination of GITR led to the rapid onset of autoimmune reactions and blocking of the receptor abrogated suppression (Shimizu et al. 2002; Ermann and Fathman 2003). Therefore, GITR works similar to CD134 and CD137 terminating suppressive function if necessary.

Comparing all the different expression profiles clearly showed changes in receptor quantities upon STAR2 activation. Additionally, an efficient activation of regulatory T cells by STAR2 binding to TNFR2 (CD120b) was confirmed. Most importantly, many of these receptors help maintain a suppressive function of the Treg population, while some others may serve as an emergency mechanism to restore an adequate immune response to infected or malignant cells.

4.3 Multiple myeloma

4.3.1 CD38 detection on multiple myeloma

Detection of CD38 on the myeloma cell line MM.1S worked as intended for CD38 (HIT2) and CD38 (ME) with no visible difference for both antibody stainings by confocal microscopy (Figure 22). However, preincubation with daratumumab blocked the epitope recognized by the monoclonal antibody CD38 (HIT2), while the polyclonal antibody still had the ability to detect CD38. Monoclonal antibodies are derived from a single cell lineage and have only one specific binding site. If this binding site is blocked or slightly changed, monoclonal antibodies will not detect the target molecule anymore. However, for therapeutic use monoclonal antibodies are often used due to their purity, the known initial efficacy and their predefined known effects on certain receptor types i.e. agonistic. In comparison, polyclonal antibodies are less expensive and show better

long-term efficacy due to their recognition of multiple binding sites (Berry 2018). In addition, polyclonal antibodies are better at detecting low-expressed molecules and most of the entire molecule population, especially when a particular binding site is sterically hard to reach. For stoichiometric analysis, binding of multiple polyclonal antibodies to one single receptor can be misinterpreted as receptor aggregation, therefore hindering their use for stoichiometric analysis. This was also observed by the localization statistics for CD38 (ME) for both patients showing localizations per cluster comparable to dimeric receptors (Figure 24 B and C). In contrast, no dimerization was observed for this receptor with the monoclonal antibody on multiple myeloma cells of patient 2023 (Figure 24 A). In addition, most of the antibodies used as therapeutics are monoclonal antibodies, which must be used to better compare the targeted receptors (Lu et al. 2020).

Quantification of three different patients showed highly abundant CD38 expression (Figure 23) and different cell morphologies (Figure 25). Even though patient 394 showed the highest amount of targetable molecules by CD38-ME, disease still progressed under daratumumab treatment. This resistance is either caused by unreachable binding sites or may be a result of genetic alterations (off-target mutations) caused by the gain of chromosome 1 or by the translocation of t(14;16) and t(14;20) of patient 394. Additionally, even though patient 225 and patient 379 showed the same amount of CD38, only patient 379's disease was regressive. Maybe the genetic change compared to patient 225 (Table 2) results in a better killing efficacy caused by the drug, or apoptotic signaling cascades are still working. These genetically diverse patients demonstrate the importance of combining receptor quantification with genetic analysis to determine whether targeted receptors are present in principle and, if so, whether treatment could lead to cell apoptosis. Additionally, it demonstrates that highly expressed receptors are not always a sign for drug response and that a more complex analysis for multiple myeloma and other malignant diseases is needed for successful individual therapy.

4.3.2 Promising targets for multiple myeloma

As shown in chapter 4.3.1, response to daratumumab is limited and depending on many factors. To improve therapeutic success for relapsed patients scientists are always in search for novel targetable molecules. For optimal treatment and minimal

side effects, these molecules should only be expressed on the target cells or at least only sparsely on healthy cells. Some of these promising targets were analyzed on two of the three patients with known genetic disorder of chromosome 14 (Table 2). It is of interest that rearrangements of the 14q32 region are the most frequent translocation mutations and were observed in 73% of MMs at diagnosis or relapse (Avet-Loiseau et al. 2002). As multiple myeloma is a highly heterogeneous disease it is very unlikely that different patients show the same myeloma clones and respond to identical therapy (de Mel et al. 2014). As expected, both patients showed completely different expression profiles with the biggest differences for CD19 and CD20. While CD19 was clearly detectable on myeloma cells of patient 379, patient 394 showed no CD19 expression at all (Figure 27). CD19 is an important B cell marker, which is typically lost during differentiation into plasma cells. However, recent reports showed not only clear expression of CD19 on multiple myeloma cells but also ultralow expression detectable only by *d*STORM, which is sufficient for lysis by highly specific CAR-T cells (Nerreter et al. 2019). Additionally, being a positive and a negative regulator of proliferation, CD19 expression seems to lead to growth inhibition and reduced tumorigenicity on myeloma cells (Ishikawa et al. 2002). The gene coding for CD19 is located on chromosome 16. The translocation mutation t(14;16) of patient 394 maybe silenced this gene or leads to a nonfunctional receptor. In contrast, high expression of CD20, whose gene is located on chromosome 11, is observed on the cells for patient 379. Possibly the t(11;14) mutation this patient is carrying results in a gain of function increasing the CD20 receptor expression on the surface. Previous studies also showed the strong correlation of CD20 expression on myeloma cells and t(11;14) (An et al. 2013). Additionally, those cells often show a small mature cell morphology that is also the case for this patient with mean cell diameters of 8.5 μm compared to 12 μm for patient 394 lacking this mutation as seen in Figure 25 (Kong et al. 2018; Robillard et al. 2003). For patient 394 also only a small subset of the MM cells showed a weak CD20 expression, suggesting a heterogeneity of myeloma cells present, probably complicating the therapy of this patient. SLAMF7 in contrast was present on both patients as reported for most multiple myeloma cells. Even though expression levels fluctuated strongly, overall detection of these receptors was greater for patient 379. It is known that SLAMF7 is highly expressed on malignant plasma cells and only sparsely distributed on immune cells (Einsele and Schreder 2016). Also, a soluble form of SLAMF7 (sSLAMF7) can be found in the plasma of ill patients acting as a regulator of

immune response when two different immune cells communicate with each other. For myeloma, the high amounts have an immune-suppressive function helping the malignant cells to proliferate and thrive (Kikuchi et al. 2020). However, due to the high abundance of this molecule, usage of the monoclonal antibody elotuzumab directed against SLAMF7, BiTEs or specific modified CAR-T cells, which are currently under investigation in the CARAMBA study, are promising therapy approaches, especially for patients, who are progressive under belantamab treatment, like patient 394. Belantamab is directed against BCMA, a molecule almost exclusively expressed on myeloma cells and normal plasma cells. Interestingly, expression of BCMA was clearly detectable by *d*STORM for both patients and was even higher on the progressive patient 394 (Figure 27). Resistance to this drug is either caused by an escape mechanism in which binding to the molecule does not induce apoptosis, or the amount of BCMA is too low to induce sufficient killing. In this case, using CAR-T cells instead of monoclonal antibodies should be considered, as it is more efficient.

CD138, which is highly abundant and one of the most important myeloma markers, was enriched mainly in the filopodia and at attachment points. CD138 functions as an important molecule for cell migration and cell-matrix interactions, which explains the accumulation at contact sites. Despite the high expression, in particular on myeloma cells, no treatment with monoclonal antibodies has yet been approved (Lonial et al. 2016; Schonfeld et al. 2017; Yu et al. 2020). Additionally, for patient 394 localization data suggests CD20 as well as BCMA to be at least partially present as a dimer (Figure 28 B), which is consistent to data described previously (Rouge et al. 2020; Bossen and Schneider 2006). For patient 379 localizations per cluster for BCMA are not showing a standard distribution caused by the sparse expression (Figure 28 A). Occurring unspecific binding events which will be detected as monomers will definitely cause problems in detecting dimeric receptors. This is also observed for the unspecific binding events of the CD19 antibody for patient 394. Most detected fluorophores have a rather low amount of less than 8 localizations per clusters. However, this can also be seen as proof of blinking events for a typical single antibody being below 10 localizations.

By quantifying all these new targets and comparing them with therapeutic approaches, it became clear that the presence of a specific receptor does not always guarantee a promising therapy. It remains important to know whether a specific receptor quantity is

required for response to a particular monoclonal or bispecific antibody or whether underlying off-target mutations reduce the efficacy of certain drugs used. For low-expressed receptors, CAR-T cell therapy is often the better choice due to its higher efficiency and should be considered when monoclonal antibody therapy does not have the desired effect. Though “the off-tumor on-target” effects need to be considered, especially by receptors highly expressed on healthy cells. Often autologous stem cell transplants are inevitable because most receptors are also present on other healthy hematologic cells (Soekojo and Kumar 2019). Due to the high level of diversity, myeloma cell therapy is a challenging task. The combination of microscopy methods to study the amount of addressable receptors and the analysis of known genetic risk factors are powerful tools to gain a better understanding of the disease and will help to improve future therapies.

However, even though chromosomal mutations can lead to changes in receptor expression, epigenetic changes such as point mutations or even cell cycle phases can also have an influence and lead to constitutively activating or inhibiting signaling cascades that help cells evade the immune response and proliferate.

4.3.3 Influence of knock-out and point mutations on the receptor expression of multiple myeloma cells

Besides genomic alterations, the influence of epigenetic mutations on receptor expression of *TP53*-deletion mutants was analyzed. *TP53* is one of the most altered genes in tumor cells and also has an important role in myeloma cells. *TP53* codes for the transcription factor p53 acting as a tumor-suppressor protein. When accumulated p53 induces production of p21. This causes further inhibiting effects, stopping the cell cycle and buying time for repair mechanisms to run. Apoptosis is initiated by activating genes of the BCL2 family, when p21 gets accumulated (Bunz et al. 1998). Of note, the *TP53*-deletion mutant UMC901 showed strongly increased CD38 expression compared to the wild type AMO1 cell line. CD38 is a multifunctional protein triggering proliferation and differentiation (Karimi-Busheri et al. 2011; Liao et al. 2014). Additionally, it contributes to heterotypic cell adhesion. Increased amounts of this receptor may indicate an amplified activity and better migration efficacy (Glaria and Valledor 2020). However, higher expression may also help targeting the cells by daratumumab as upregulation of CD38 by different drugs e.g. ricolinostat increased

killing efficacy for this monoclonal antibody (Garcia-Guerrero et al. 2017; Garcia-Guerrero et al. 2021). It also became obvious that cell attachment changed for UMC901. As seen for the two analyzed patients, CD138 is always accumulated at attachment areas or filopodia (Figure 30). For *TP53*-deletion mutants extremely aberrant cell morphology was observed as all of the cells displayed very long filopodia strongly enriched with CD138, confirming an increased adherence strength compared to the wild type. Due to the non-uniform distribution of the molecule, a quantification is not possible, especially due to the strong accumulation in filopodia. For SLAMF7 no real difference between both cell lines was observed, possibly being not influenced by the mutation at all.

In contrast to the three previously described receptors, BCMA expression was slightly decreased on *TP53*-deleterious mutants. This small change most likely has no significant influence on cell behavior or treatment effectiveness by belantamab or other BCMA targeted treatments.

Changes of the tumor suppressor gene *TP53* severely changed cell morphology and expression of receptors important for cell proliferation and migration, while some others were unaffected. Even though only ~5% of all patients show a *TP53* mutation at the beginning of their diagnosis, the amount of *TP53* mutation strongly increases for each relapse, thus indicating it to be an important factor for drug resistance (Jovanovic et al. 2018). In contrast to *TP53*, mutations of *KRAS*, a proto-oncogene also important for cell growth, survival and differentiation, are quite common in early multiple myeloma. The LG8 mutant had a point mutation at G12A, which is also common in other tumors like lung cancer or colorectal cancer and associated with a poor prognosis (Fiala et al. 2016). Maybe the exchange of the most flexible amino acid glycine to a more rigid amino acid causes a constitutive activation of this protein. LG9 instead has a *KRAS* A146T mutation known as a weakly activating mutation that promotes nucleotide exchange in the absence of guanine nucleotide exchange factor (Poulin et al. 2019). Comparison of receptor expression clearly showed differences for both mutations. However, LG8 cells showed an overall reduction of CD38, BCMA and SLAMF7, possibly reducing the addressability for monoclonal antibodies or BiTEs (Figure 32). Of note, the LG8 cells have a point mutation, which is associated with a poor prognosis and an early relapse in different types of cancer. Maybe this poor outcome is associated with the completely changed “receptome” on the cell surface. The A146T

mutant in contrast only showed a slightly increased CD38 expression, while the other three receptor quantities stayed mostly unaffected, even though the KRAS structure changed drastically (Poulin et al. 2019). Comparing localization data of the different cell lines showed no significant change within the AMO1 cell lines, with SLAMF7 having a monomeric and CD38, CD138 and BCMA showing a rather dimeric mean value of the localizations per cluster (Table 14). For OPM2 cell lines the localizations per cluster were highest for the WT cell line, suggesting less multimeric receptors for both mutants. Additionally, SLAMF7 had significantly more localizations per cluster on WT cells compared to both of the mutants, suggesting at least a partial aggregation of SLAMF7 receptors. Since SLAMF7 protein is only sold by companies as a homodimer, it can at least be assumed that the receptor can possibly dimerize.

Furthermore, it is of interest that even though the structure of KRAS was affected by both of the point mutations, the expression profile of the investigated receptors differed. Knowing more about KRAS protein behavior and the influence of a specific mutant on receptor expression might help increasing therapy effectiveness. For this, patient samples with underlying *TP53* and KRAS mutations need to be analyzed and compared to unaffected patients in future experiments.

4.4 Quantification of FLT3 on AML cell lines and primary cells

Acute myeloid leukemia is a malignancy of stem cell precursors of the myeloid lineage and associated with a poor prognosis. For decades, high-dose chemotherapy was the standard therapy with survival rates stagnating until very recently. Understanding of the genetic alterations and novel FDA-approved drugs increased overall survival rates and improved therapy efficiency (Pelcovits and Niroula 2020; Swaminathan and Wang 2020). One of the most frequently mutated genes observed in AML is coding for the tyrosine-kinase FLT3, which is important for cell survival, proliferation and differentiation. Nowadays, tyrosine-kinase inhibitors like midostaurin are broadly used to block the signaling through these receptors which increases the overall survival rate of patients with underlying FLT3 mutation. However, similar to multiple myeloma, a certain percentage of the malignant cells will become resistant to the applied drug by on- or off-target mutations, making therapy inefficient. This is also validated by the fact that cultivating MV4-11 or MOLM-13 cell lines with a pre-defined midostaurin dose, which was increased weekly, resulted in a midostaurin-resistant (MID⁺) population of

the respective cell line. Staining cells according to the live cell protocol demonstrated highly specific antibody binding events with only sparse unspecific binding to the glass surface. For MOLM-13 midostaurin-sensitive (MID⁻) cells the lowest FLT3 expression with a rather homogeneous distribution and only some small oligomeric populations compared to the other cell lines was observed (Figure 33). In contrast, MOLM-13 MID⁺ cells are strongly clustered and more FLT3 can be observed. As signaling through FLT3 typically is induced by bridging two FLT3 molecules by the corresponding FLT3 ligand, present homodimers suggest greater tumor proliferation and survival (Figure 33 C). Dense clusters of FLT3 may contribute to midostaurin binding sites being less accessible or increased signaling through the receptor. Additionally, high FLT3 expression is considered as a risk factor with reduced survival rates which is an additional hint for off-target mutations in *NRAS*, *AXL* and *PIM1* present (Cheng et al. 2018). In contrast, MV4-11 MID⁺ and MID⁻ cells showed identical expression quantities of FLT3 and no obvious clustering of this receptor (Figure 33 B and C). However, both types demonstrated a clear homodimeric subpopulation present. Resistance may also be caused by off-target mutations that bypass or reinforce FLT3 signaling (Eguchi et al. 2020). Both cell lines have an underlying FLT3 inter-tandem-duplication (ITD), which is one of the most highly occurring mutations in AML. For the cell line MV4-11 both alleles are affected while MOLM-13 cells still have one WT allele left (Quentmeier et al. 2003). Since inter-tandem-duplications are also associated with increased protein levels, the expression difference between MV4-11 and MOLM-13 could be explained by the number of alleles affected (Xing et al. 2019). Additionally, FLT3-ITD affect the area coding for the juxtamembrane, causing dimerization and a constitutive activation through auto-phosphorylation (Kiyoi and Naoe 2002). Both cell lines showed either different receptor assemblies or quantities between MID⁺ and MID⁻ cells which was not visible from the diffraction-limited images, but became obvious from the super-resolved images (Figure 33). Note that treating these cell lines with midostaurin to achieve resistance caused clearly visible differences, either in regard of receptor assembly (Figure 33 A) or receptor amount (Figure 33 B). However, this does not allow any conclusion to be drawn about present off-target mutations, but rather demonstrates the high importance of super-resolution techniques in clinical context. The primary cells showed - besides monomeric receptor trends - the clear presence of a homodimeric population at ~ 10 localizations/cluster, suggesting bridged FLT3 receptors and therefore activating signals (Figure 34 B & C) (Griffith et al. 2004; Grafone et al. 2012).

However, to confirm these assumptions, intracellular FLT3 phosphorylation needs to be checked, as dimerization is only the first activation step in this signaling cascade (Grafone et al. 2012 226). The FLT3 receptor expression, on the other hand, was rather low compared to all cell lines. Maybe present MID⁺ cells are a subpopulation with different off-target mutations causing constitutive proliferation of the cells.

5 Conclusion and Outlook

During this work, it was possible to demonstrate a significant benefit of super-resolution microscopy for analysis of small structures or molecule assemblies. Stoichiometric changes of specific receptors that especially occur during disease are an important indication of underlying activating or inhibitory effects and may contribute to therapeutic decisions in the future. Although information about present monomeric, dimeric or clustering receptors was obtained, it is still complicated to estimate the real percentage of these population. Therefore, it would be helpful to determine mathematical functions that underlie monomeric, dimeric or trimeric populations to gain better estimations of the present oligomerization states. Additionally, DBSCAN reliability suffers from the user-defined input parameters, in particular the pre-defined maximal distance ϵ of a localization cluster. This can be avoided by using an HDBSCAN, which automatically varies the value for the maximum distance and selects the ϵ with highest stability for all present clusters. Here, only the minimum localizations per cluster (MinPts) is required as an input parameter, which likely makes it more robust for clustering data with variable densities, such as heterogeneous clusters of receptors like CD3, where no defined differences from dimeric receptors have been observed (Malzer 2019). PALM microscopy is another method of choice for gathering stoichiometric information of membrane receptors as shown previously (Fricke et al. 2015; Lehmann et al. 2021), but also suffers from different drawbacks like a long acquisition time, detection of intracellular molecules that are close to the plasma-membrane and also relies on the calibration with known monomeric and dimeric receptors. Combining *d*STORM with PALM-like dyes, e.g. Cy3B or Cy5B, may be a promising combination for the future, especially when only a subpopulation of the receptor oligomerizes as the blinking occurrence of Cy5B is less fluctuating compared to typical used dyes. In addition, the high quantum yield of Cy5B leads to an increased localization precision (Figure 35), thereby possibly improving the separability of two adjacent spots. Finding dyes that are photoswitching more reliably is of high interest, especially when used as a second or even third color for *d*STORM where it needs to be compatible with the same buffer system. To date, most of the used dyes in the yellow or green absorbance spectrum suffer from low signal-to-noise ratio, increased unspecific binding or lower detection quantities and dyes in the blue to ultraviolet range are performing even worse and therefore are mainly avoided. This will become a tremendous issue when interactions by co-localization of two or more molecules should be obtained. However, as an

addition two-color *d*STORM is an important tool to verify existing oligomers by determining the amount of co-localization, even though stoichiometric information can also be gathered by blinking statistics of AF647 on its own.

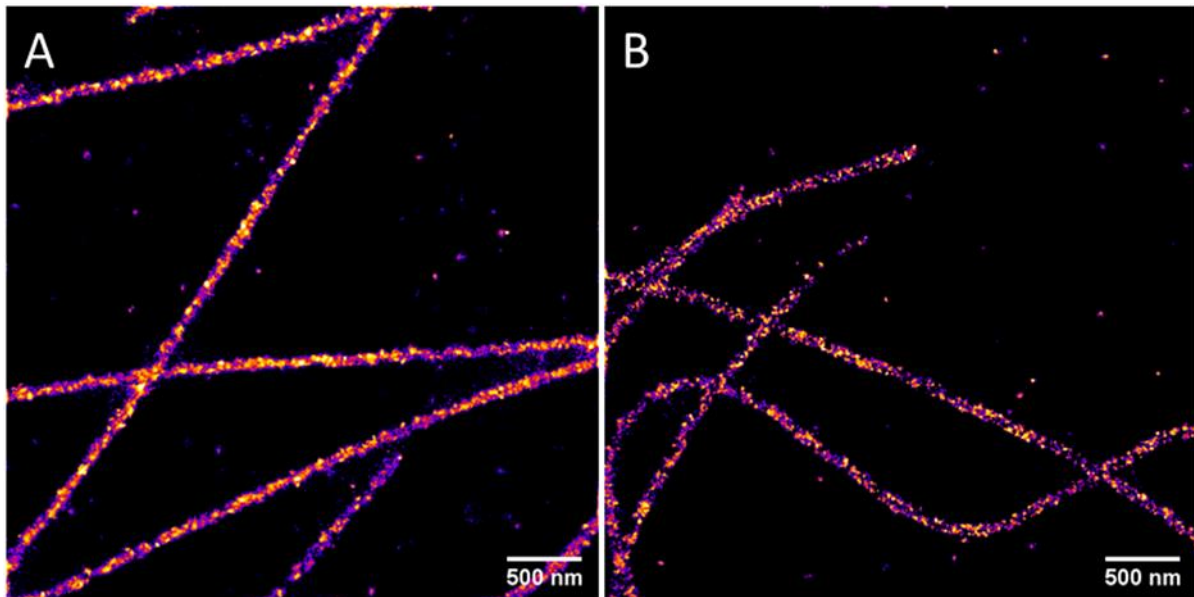


Figure 35 - Representative *d*STORM images of α -tubulin stained with Cy5 (A) and Cy5B (B) in COS-7 cells. Images were acquired over 120,000 frames with an exposure time of 5 ms and reconstructed with 5 nm/px. Mean localization precision was slightly better for Cy5B with 6.58 \pm 3.26 (s.d.) and 6.47 \pm 3.29 (s.d.) compared to Cy5 with 8.44 \pm 4.33 (s.d.) and 8.27 \pm 4.40 (s.d.) for x- and y-direction, respectively.

Of note, localization statistics could also provide information about interactions when two or more different molecules come in proximity as seen for LFA-1 with cluster densities staying almost the same while more blinking events were detected. However, the reliability will always suffer from epitope accessibility, especially for trimers or higher oligomers. To overcome the issue of epitope availability due to the size of antibodies, nanobodies could be of interest and help detecting most of the true receptor population on the surface. Alternatively, peptides or toxins that are smaller in size might also be an option. Being in proximity however could obliterate the effects seen by antibodies to observe two separated spots and in worst case result in homo-FRET making detection of oligomers impossible. Also, the use of different antibody clones against epitopes further away from the cell surface may improve quantitative and stoichiometric examination and lead to more reliable results. Usage of directly-labeled monoclonal antibodies is therefore crucial, because polyclonal antibodies can detect the same receptor multiple times but on different epitopes, causing artificial clustering effects. Instead of using stochastic photoswitching, DNA-PAINT approaches might be

of interest for stoichiometric analysis, either by modifying the target of interest with a small nucleotide sequence to which imager strands can bind or by using DNA-conjugated ligands. Since the modification of targets with nucleotide sequences requires transfection for primary cells only DNA-conjugated ligands or antibodies are applicable. Compared to *d*STORM a better resolution can be achieved, but at the cost of image acquisition time. Besides using SMLM approaches, expansion microscopy (ExM) might possibly help detecting small oligomers, especially when binding epitopes are preserved. However, only the ExM protocols with labeling after expansion are suited to make adjacent epitopes accessible and are of interest. By combining 10x ExM with Lattice SIM microscopy, structures of ~7-10 nm could be resolved and the issue of sterically hindrances would be overcome. Additionally, the usage of 10x ExM with postlabeled structures together with *d*STORM (U-ExM) is able to achieve a resolution of about ~2-5 nm (Gambarotto et al. 2019). To address the issue of label efficiency of antibodies, click chemistry could be helpful. Here the protein of interest needs a site-directed mutagenesis to introduce an amber stop codon, which has to be transfected together with an unnatural tRNA-synthetase. The unnatural amino acid is then effectively incorporated into the modified protein and can then be “clicked” by addition of tetrazine-modified dyes, leading to the smallest possible linkage error (Beliu et al. 2019). This is helpful to study basic receptor assemblies and their oligomerization states, but to analyze primary patient cells the receptors would need to be modified with the TCO by knock-in CRISPR or nucleofection which is highly complex and therefore results are possibly not reliable. This is also the fact for cell lines as no endogenous receptors but only overexpressed receptors are analyzed. This may also change assembly or stoichiometry of the overexpressed receptor.

Analyzing primary murine T regulator cells made it possible to obtain quantitative data and underlying differences between naive and activated cells. However, most of the receptor changes were expected and showed no stoichiometric differences during the activation. Still the alternative activation with the ligand TNFR2 was confirmed making it easier to expand Tregs *in-vivo* instead of the more complicated *ex-vivo* expansion by CD3/CD28. To see if there are fundamental changes between CD3/CD28 activation and TNFR2-stimulated activation, receptor expression has to be compared for both activation methods. Combining co-localization experiments of promising receptors (like CD120b with different receptors mentioned in 3.2) may help to understand ongoing

processes, whereas treatment of Tregs with certain cytokines or specific blocking of different receptors may help to understand the underlying suppressive mechanisms.

Finding novel therapeutic targets is one important part of improving therapy efficacy and survival rates of different malignancies, like the multiple myeloma. Quantification of primary patient cells and comparison of the cell morphologies showed clear differences between all myeloma populations. Even within one patient different subtypes of myeloma cells could be identified. From previous studies, high receptor expression is often related to a good response to the corresponding monoclonal antibody. Screening the myeloma population for novel and unique receptors that are most likely expressed on the surface may help to find an overexpressed target or a target which is mainly expressed on malignant cells, which could then be used for drug application. Unfortunately, when heavily treated, most myeloma cells show a variety of escape mechanisms and tumor progression will occur under the applied treatment. This is either caused by a loss or downregulation of the receptor or by molecular mechanisms that are not visible by antigen screening, e.g. daratumumab resistance of patient 394, even though high levels of CD38 were expressed. As stated, for a high-risk patient a combination of receptor quantification and genomic sequencing can help to define specific treatment strategies. For this, a lot more statistics has to be done and patients need to be analyzed before therapy and after each relapse to understand better the escape mechanism of these cells and how the genetic changes influence the response to certain drugs. In addition, upregulation of certain receptors by different drugs may help to maintain a sufficient amount for effective killing or, when quantities are too low, using CAR-T cells that are known to be extremely sensitive. Additionally, when certain drugs are getting ineffective due to off-target mutations, radionuclide-coupled monoclonal antibodies could help to clear tumors still expressing the targeted receptors like for patient 394 who expressed high amounts of CD38. In contrast to certain toxins or drugs, radionuclides do not have to be internalized to cause lysis of the targeted cells as binding to the receptor is the only requirement (Kozak et al. 1986). As radioimmunotherapy is more effective than just mAbs, side effects have to be considered and stem cell transplantation may be required (Goldenberg 2007). In contrast to hematopoietic malignancies, radioimmunotherapy can be an excellent choice for solid tumors when applied locally (Goldenberg 2007). The amount of present targetable receptors is therefore helpful to decide which kind of immune therapy is most promising and which receptors are addressable at all. Comparing existing

receptor quantities on malignant cells with healthy tissue will also help to minimize side effects because therapy can be adjusted to be less sensitive if needed.

In addition, fundamental changes were observed by eliminating or mutating certain oncogenes or tumor suppressor genes showing the relevance of genetic alterations on receptor expression. For future experiments, it would be beneficial to know if these deletions or point mutations always lead to the same increase or decrease of receptor expression, in particular when occurring in patients' malignancies. Furthermore, stoichiometric analysis can help to detect activation processes caused by accumulation of certain receptors as seen for FLT3, whose activation is preceded by dimerization. As seen for all tumor cells altered expression profiles of certain receptors and their unrestrained cell proliferation are mainly caused by underlying failed repair and safety mechanisms.

In summary, even cells with low expression levels of membrane receptors can be targeted by various available immunotherapies to induce cell apoptosis. However, it must be considered that "off-target" mutations or the tumor microenvironment will impede therapy effectiveness and make combination therapy inevitable.

Membrane receptors however, are also important entry points for different pathogens and viruses, which are exploiting them as a docking site to infect the cell. Because of COVID-19 appearing in early 2020, attention was drawn to the ACE2 receptor to which the spike protein of SARS-COV2 binds. It is thought that high expression is beneficial and increases the chance of entry and infection by the virus (Ciaglia, Vecchione, and Puca 2020). First quantitative experiments with ACE2-expressing cells and pseudoviruses showed that infections occur more frequently for cells expressing high levels, still low levels of ACE2 were sufficient for successful infection. In theory, presenting one addressable receptor is enough for a highly specific virus to bind and infect a cell, showing the importance of highly specific antibodies for research but also the need for highly specific detection methods like *d*STORM.

Although receptors are prominent targets and easy to address, more information about whole-cell changes need to be generated. For example, it is known that 95% of all cancer cells show an increased amount of glycocalyx. However, little is known about its role for cell adhesion and how it possibly influences tumor survival (Kanyo et al. 2020). Overexpression of the sialylated monosaccharide N-Acetylgalactosamine (GalNAc) is observed in most cancers and missing in healthy cells and leads to

increased cell proliferation, migration, invasion, and decreased cell adhesion (Kang et al. 2018). Therefore, targeting this specific saccharide could be a promising target with only low or even no side effects. Even though a lot more statistics needs to be done to correlate specific risk factors, genetic alterations and chromosomal changes to receptor expression and effective treatment possibilities, great progress has been made in recent years as novel targets for immunotherapy or specific binding sites of pathogens have been identified. However, the high sensitivity of e.g. CAR-T cell therapies as well as the high binding specificity of microorganisms increasingly demonstrate the need for highly specific methods like *d*STORM for medical applications in the future and surely will continue to drive the field forward.

6 Bibliography

- Abbe, E. 1873. 'Beiträge zur Theorie des Mikroskops und der mikroskopischen Wahrnehmung', *Archiv für Mikroskopische Anatomie*, 9: 413-68.
- Adams, G. P., and L. M. Weiner. 2005. 'Monoclonal antibody therapy of cancer', *Nat Biotechnol*, 23: 1147-57.
- Akhmetzyanova, I., M. J. McCarron, S. Parekh, M. Chesi, P. L. Bergsagel, and D. R. Fooksman. 2020. 'Dynamic CD138 surface expression regulates switch between myeloma growth and dissemination', *Leukemia*, 34: 245-56.
- Akhmetzyanova, I., G. Zelinskyy, E. Littwitz-Salomon, A. Malyshkina, K. K. Dietze, H. Streeck, S. Brandau, and U. Dittmer. 2016. 'CD137 Agonist Therapy Can Reprogram Regulatory T Cells into Cytotoxic CD4+ T Cells with Antitumor Activity', *J Immunol*, 196: 484-92.
- Alberts, B., D. Bray, K. Hopkin, A.D. Johnson, J. Lewis, M. Raff, K. Roberts, and P. Walter. 2015. *Essential Cell Biology* (CRC Press).
- An, G., Y. Xu, L. Shi, D. Zou, S. Deng, W. Sui, Z. Xie, M. Hao, H. Chang, and L. Qiu. 2013. 't(11;14) multiple myeloma: a subtype associated with distinct immunological features, immunophenotypic characteristics but divergent outcome', *Leuk Res*, 37: 1251-7.
- Anz, D., W. Mueller, M. Golic, W. G. Kunz, M. Rapp, V. H. Koelzer, J. Ellermeier, J. W. Ellwart, M. Schnurr, C. Bourquin, and S. Endres. 2011. 'CD103 is a hallmark of tumor-infiltrating regulatory T cells', *Int J Cancer*, 129: 2417-26.
- Atanackovic, D., S. V. Radhakrishnan, N. Bhardwaj, and T. Luetkens. 2016. 'Chimeric Antigen Receptor (CAR) therapy for multiple myeloma', *Br J Haematol*, 172: 685-98.
- Avet-Loiseau, H., T. Facon, B. Grosbois, F. Magrangeas, M. J. Rapp, J. L. Harousseau, S. Minvielle, R. Bataille, and Myelome Intergroupe Francophone du. 2002. 'Oncogenesis of multiple myeloma: 14q32 and 13q chromosomal abnormalities are not randomly distributed, but correlate with natural history, immunological features, and clinical presentation', *Blood*, 99: 2185-91.
- Bader, A. N., E. G. Hofman, J. Voortman, P. M. en Henegouwen, and H. C. Gerritsen. 2009. 'Homo-FRET imaging enables quantification of protein cluster sizes with subcellular resolution', *Biophys J*, 97: 2613-22.
- Bajar, B. T., E. S. Wang, S. Zhang, M. Z. Lin, and J. Chu. 2016. 'A Guide to Fluorescent Protein FRET Pairs', *Sensors (Basel)*, 16.
- Beliu, G., A. J. Kurz, A. C. Kuhlemann, L. Behringer-Pliess, M. Meub, N. Wolf, J. Seibel, Z. D. Shi, M. Schnermann, J. B. Grimm, L. D. Lavis, S. Doose, and M. Sauer. 2019. 'Bioorthogonal labeling with tetrazine-dyes for super-resolution microscopy', *Commun Biol*, 2: 261.
- Berry, C. M. 2018. 'Antibody immunoprophylaxis and immunotherapy for influenza virus infection: Utilization of monoclonal or polyclonal antibodies?', *Hum Vaccin Immunother*, 14: 796-99.
- Blom, H., and J. Widengren. 2017. 'Stimulated Emission Depletion Microscopy', *Chem Rev*, 117: 7377-427.
- Bossen, C., and P. Schneider. 2006. 'BAFF, APRIL and their receptors: structure, function and signaling', *Semin Immunol*, 18: 263-75.
- Bunz, F., A. Dutriaux, C. Lengauer, T. Waldman, S. Zhou, J. P. Brown, J. M. Sedivy, K. W. Kinzler, and B. Vogelstein. 1998. 'Requirement for p53 and p21 to sustain G2 arrest after DNA damage', *Science*, 282: 1497-501.
- Buss, N. A., S. J. Henderson, M. McFarlane, J. M. Shenton, and L. de Haan. 2012. 'Monoclonal antibody therapeutics: history and future', *Curr Opin Pharmacol*, 12: 615-22.
- Campbell, K. S., A. D. Cohen, and T. Pazina. 2018. 'Mechanisms of NK Cell Activation and Clinical Activity of the Therapeutic SLAMF7 Antibody, Elotuzumab in Multiple Myeloma', *Front Immunol*, 9: 2551.
- Carter, J. L., K. Hege, J. Yang, H. A. Kalpage, Y. Su, H. Edwards, M. Huttemann, J. W. Taub, and Y. Ge. 2020. 'Targeting multiple signaling pathways: the new approach to acute myeloid leukemia therapy', *Signal Transduct Target Ther*, 5: 288.

- Chang, L. Y., Y. C. Lin, C. W. Kang, C. Y. Hsu, Y. Y. Chu, C. T. Huang, Y. J. Day, T. C. Chen, C. T. Yeh, and C. Y. Lin. 2012. 'The indispensable role of CCR5 for in vivo suppressor function of tumor-derived CD103+ effector/memory regulatory T cells', *J Immunol*, 189: 567-74.
- Chen, X., J. J. Subleski, R. Hamano, O. M. Howard, R. H. Wiltrott, and J. J. Oppenheim. 2010. 'Co-expression of TNFR2 and CD25 identifies more of the functional CD4+FOXP3+ regulatory T cells in human peripheral blood', *Eur J Immunol*, 40: 1099-106.
- Cheng, J., L. Qu, J. Wang, L. Cheng, and Y. Wang. 2018. 'High expression of FLT3 is a risk factor in leukemia', *Mol Med Rep*, 17: 2885-92.
- Cho, S. F., K. C. Anderson, and Y. T. Tai. 2018. 'Targeting B Cell Maturation Antigen (BCMA) in Multiple Myeloma: Potential Uses of BCMA-Based Immunotherapy', *Front Immunol*, 9: 1821.
- Chopra, M., M. Biehl, T. Steinfatt, A. Brandl, J. Kums, J. Amich, M. Vaeth, J. Kuen, R. Holtappels, J. Podlech, A. Mottok, S. Kraus, A. L. Jordan-Garrote, C. A. Bauerlein, C. Brede, E. Ribechini, A. Fick, A. Seher, J. Polz, K. J. Ottmuller, J. Baker, H. Nishikii, M. Ritz, K. Mattenheimer, S. Schwinn, T. Winter, V. Schafer, S. Krappmann, H. Einsele, T. D. Muller, M. J. Reddehase, M. B. Lutz, D. N. Mannel, F. Berberich-Siebelt, H. Wajant, and A. Beilhack. 2016. 'Exogenous TNFR2 activation protects from acute GvHD via host T reg cell expansion', *J Exp Med*, 213: 1881-900.
- Ciaglia, E., C. Vecchione, and A. A. Puca. 2020. 'COVID-19 Infection and Circulating ACE2 Levels: Protective Role in Women and Children', *Front Pediatr*, 8: 206.
- Coombes, J. L., K. R. Siddiqui, C. V. Arancibia-Carcamo, J. Hall, C. M. Sun, Y. Belkaid, and F. Powrie. 2007. 'A functionally specialized population of mucosal CD103+ DCs induces Foxp3+ regulatory T cells via a TGF-beta and retinoic acid-dependent mechanism', *J Exp Med*, 204: 1757-64.
- Corthay, A. 2009. 'How do regulatory T cells work?', *Scand J Immunol*, 70: 326-36.
- Daraei, N., M. Ghafourian, A. Ghadiri, A. Amari, M. Najafian, and S. Rokhafrooz. 2019. 'Evaluation of Exhausted Regulatory T Cells in Preeclampsia', *Iran J Immunol*, 16: 163-69.
- Daver, N., R. F. Schlenk, N. H. Russell, and M. J. Levis. 2019. 'Targeting FLT3 mutations in AML: review of current knowledge and evidence', *Leukemia*, 33: 299-312.
- De Kouchkovsky, I., and M. Abdul-Hay. 2016. "Acute myeloid leukemia: a comprehensive review and 2016 update", *Blood Cancer J*, 6: e441.
- de Mel, S., S. H. Lim, M. L. Tung, and W. J. Chng. 2014. 'Implications of heterogeneity in multiple myeloma', *Biomed Res Int*, 2014: 232546.
- Dohner, H., E. Estey, D. Grimwade, S. Amadori, F. R. Appelbaum, T. Buchner, H. Dombret, B. L. Ebert, P. Fenaux, R. A. Larson, R. L. Levine, F. Lo-Coco, T. Naoe, D. Niederwieser, G. J. Ossenkoppele, M. Sanz, J. Sierra, M. S. Tallman, H. F. Tien, A. H. Wei, B. Lowenberg, and C. D. Bloomfield. 2017. 'Diagnosis and management of AML in adults: 2017 ELN recommendations from an international expert panel', *Blood*, 129: 424-47.
- Dransfield, I., C. Cabanas, A. Craig, and N. Hogg. 1992. 'Divalent cation regulation of the function of the leukocyte integrin LFA-1', *J Cell Biol*, 116: 219-26.
- Durisic, N., L. Laparra-Cuervo, A. Sandoval-Alvarez, J. S. Borbely, and M. Lakadamyali. 2014. 'Single-molecule evaluation of fluorescent protein photoactivation efficiency using an in vivo nanotemplate', *Nat Methods*, 11: 156-62.
- Eggenhuizen, P. J., B. H. Ng, and J. D. Ooi. 2020. 'Treg Enhancing Therapies to Treat Autoimmune Diseases', *Int J Mol Sci*, 21.
- Eguchi, M., Y. Minami, A. Kuzume, and S. Chi. 2020. 'Mechanisms Underlying Resistance to FLT3 Inhibitors in Acute Myeloid Leukemia', *Biomedicines*, 8.
- Einsele, H., and M. Schreder. 2016. 'Treatment of multiple myeloma with the immunostimulatory SLAMF7 antibody elotuzumab', *Ther Adv Hematol*, 7: 288-301.
- Engel, P., L. Boumsell, R. Balderas, A. Bensussan, V. Gattei, V. Horejsi, B. Q. Jin, F. Malavasi, F. Mortari, R. Schwartz-Albiez, H. Stockinger, M. C. van Zelm, H. Zola, and G. Clark. 2015. 'CD Nomenclature 2015: Human Leukocyte Differentiation Antigen Workshops as a Driving Force in Immunology', *J Immunol*, 195: 4555-63.

- Ermann, J., and C. G. Fathman. 2003. 'Costimulatory signals controlling regulatory T cells', *Proc Natl Acad Sci U S A*, 100: 15292-3.
- Eslick, R., and D. Talaulikar. 2013. 'Multiple myeloma: from diagnosis to treatment', *Aust Fam Physician*, 42: 684-8.
- Espagnolle, N., D. Depoil, R. Zaru, C. Demeur, E. Champagne, M. Guiraud, and S. Valitutti. 2007. 'CD2 and TCR synergize for the activation of phospholipase Cgamma1/calcium pathway at the immunological synapse', *Int Immunol*, 19: 239-48.
- Ester, Martin, Hans-Peter Kriegel, Jörg Sander, and Xiaowei Xu. 1996. "A density-based algorithm for discovering clusters in large spatial databases with noise." In *Proceedings of the Second International Conference on Knowledge Discovery and Data Mining*, 226–31. Portland, Oregon: AAAI Press.
- Estey, E. H. 2018. 'Acute myeloid leukemia: 2019 update on risk-stratification and management', *Am J Hematol*, 93: 1267-91.
- Etoh, T. G., A. Q. Nguyen, Y. Kamakura, K. Shimonomura, T. Y. Le, and N. Mori. 2017. 'The Theoretical Highest Frame Rate of Silicon Image Sensors', *Sensors (Basel)*, 17.
- Feng, H., X. Wang, Z. Xu, X. Zhang, and Y. Gao. 2018. 'Super-Resolution Fluorescence Microscopy for Single Cell Imaging', *Adv Exp Med Biol*, 1068: 59-71.
- Fiala, O., T. Buchler, B. Mohelnikova-Duchonova, B. Melichar, V. M. Matejka, L. Holubec, J. Kulhankova, Z. Bortlicek, M. Bartouskova, V. Liska, O. Topolcan, M. Sedivcova, and J. Finek. 2016. 'G12V and G12A KRAS mutations are associated with poor outcome in patients with metastatic colorectal cancer treated with bevacizumab', *Tumour Biol*, 37: 6823-30.
- Fricke, F., J. Beaudouin, R. Eils, and M. Heilemann. 2015. 'One, two or three? Probing the stoichiometry of membrane proteins by single-molecule localization microscopy', *Sci Rep*, 5: 14072.
- Gambarotto, D., F. U. Zwettler, M. Le Guennec, M. Schmidt-Cernohorska, D. Fortun, S. Borgers, J. Heine, J. G. Schloetel, M. Reuss, M. Unser, E. S. Boyden, M. Sauer, V. Hamel, and P. Guichard. 2019. 'Imaging cellular ultrastructures using expansion microscopy (U-ExM)', *Nat Methods*, 16: 71-74.
- Garcia-Guerrero, E., T. Gogishvili, S. Danhof, M. Schreder, C. Pallaud, J. A. Perez-Simon, H. Einsele, and M. Hudecek. 2017. 'Panobinostat induces CD38 upregulation and augments the antimyeloma efficacy of daratumumab', *Blood*, 129: 3386-88.
- Garcia-Guerrero, E., R. Gotz, S. Doose, M. Sauer, A. Rodriguez-Gil, T. Nerreter, K. M. Kortum, J. A. Perez-Simon, H. Einsele, M. Hudecek, and S. Danhof. 2021. 'Upregulation of CD38 expression on multiple myeloma cells by novel HDAC6 inhibitors is a class effect and augments the efficacy of daratumumab', *Leukemia*, 35: 201-14.
- Ghoreschi, K., A. Laurence, X. P. Yang, K. Hirahara, and J. J. O'Shea. 2011. 'T helper 17 cell heterogeneity and pathogenicity in autoimmune disease', *Trends Immunol*, 32: 395-401.
- Giancetti, E., and A. Fierabracci. 2018. 'Inhibitory Receptors and Pathways of Lymphocytes: The Role of PD-1 in Treg Development and Their Involvement in Autoimmunity Onset and Cancer Progression', *Front Immunol*, 9: 2374.
- Glaria, E., and A. F. Valledor. 2020. 'Roles of CD38 in the Immune Response to Infection', *Cells*, 9.
- Gogishvili, T., S. Danhof, S. Prommersberger, J. Rydzek, M. Schreder, C. Brede, H. Einsele, and M. Hudecek. 2017. 'SLAMF7-CAR T cells eliminate myeloma and confer selective fratricide of SLAMF7(+) normal lymphocytes', *Blood*, 130: 2838-47.
- Gol-Ara, M., F. Jadidi-Niaragh, R. Sadria, G. Azizi, and A. Mirshafiey. 2012. 'The role of different subsets of regulatory T cells in immunopathogenesis of rheumatoid arthritis', *Arthritis*, 2012: 805875.
- Goldenberg, D. M. 2007. 'Radiolabelled monoclonal antibodies in the treatment of metastatic cancer', *Curr Oncol*, 14: 39-42.
- Götz, Ralph. 2020. 'Super-resolution microscopy of plasma membrane receptors and intracellular pathogens', *Universität Würzburg*.

- Grafone, T., M. Palmisano, C. Nicci, and S. Storti. 2012. 'An overview on the role of FLT3-tyrosine kinase receptor in acute myeloid leukemia: biology and treatment', *Oncol Rev*, 6: e8.
- Griffith, J., J. Black, C. Faerman, L. Swenson, M. Wynn, F. Lu, J. Lippke, and K. Saxena. 2004. 'The structural basis for autoinhibition of FLT3 by the juxtamembrane domain', *Mol Cell*, 13: 169-78.
- Gun, S. Y., S. W. L. Lee, J. L. Sieow, and S. C. Wong. 2019. 'Targeting immune cells for cancer therapy', *Redox Biol*, 25: 101174.
- Heilemann, M., S. van de Linde, A. Mukherjee, and M. Sauer. 2009. 'Super-resolution imaging with small organic fluorophores', *Angew Chem Int Ed Engl*, 48: 6903-8.
- Heldin, C. H., B. Lu, R. Evans, and J. S. Gutkind. 2016. 'Signals and Receptors', *Cold Spring Harb Perspect Biol*, 8: a005900.
- Helmerich, D. A., G. Beliu, and M. Sauer. 2020. 'Multiple-Labeled Antibodies Behave Like Single Emitters in Photoswitching Buffer', *ACS Nano*, 14: 12629-41.
- Herold, N. C., and P. Mitra. 2021. 'Immunophenotyping.' in, *StatPearls* (Treasure Island (FL)).
- Hilger, D., M. Masureel, and B. K. Kobilka. 2018. 'Structure and dynamics of GPCR signaling complexes', *Nat Struct Mol Biol*, 25: 4-12.
- Hombach, A. A., D. Kofler, A. Hombach, G. Rappl, and H. Abken. 2007. 'Effective proliferation of human regulatory T cells requires a strong costimulatory CD28 signal that cannot be substituted by IL-2', *J Immunol*, 179: 7924-31.
- Hsi, E. D., R. Steinle, B. Balasa, S. Szmania, A. Draksharapu, B. P. Shum, M. Huseni, D. Powers, A. Nanisetti, Y. Zhang, A. G. Rice, A. van Abbema, M. Wong, G. Liu, F. Zhan, M. Dillon, S. Chen, S. Rhodes, F. Fuh, N. Tsurushita, S. Kumar, V. Vexler, J. D. Shaughnessy, Jr., B. Barlogie, F. van Rhee, M. Hussein, D. E. Afar, and M. B. Williams. 2008. 'CS1, a potential new therapeutic antibody target for the treatment of multiple myeloma', *Clin Cancer Res*, 14: 2775-84.
- Huang, H. W., C. H. Chen, C. H. Lin, C. H. Wong, and K. I. Lin. 2013. 'B-cell maturation antigen is modified by a single N-glycan chain that modulates ligand binding and surface retention', *Proc Natl Acad Sci U S A*, 110: 10928-33.
- Ishikawa, H., N. Tsuyama, M. S. Mahmoud, R. Fujii, S. Abroun, S. Liu, F. J. Li, and M. M. Kawano. 2002. 'CD19 expression and growth inhibition of tumours in human multiple myeloma', *Leuk Lymphoma*, 43: 613-6.
- Iwasaki, H., and K. Akashi. 2007. 'Myeloid lineage commitment from the hematopoietic stem cell', *Immunity*, 26: 726-40.
- Joshua, D. E., C. Bryant, C. Dix, J. Gibson, and J. Ho. 2019. 'Biology and therapy of multiple myeloma', *Med J Aust*, 210: 375-80.
- Jovanovic, K. K., G. Escure, J. Demonchy, A. Willaume, Z. Van de Wyngaert, M. Farhat, P. Chauvet, T. Facon, B. Quesnel, and S. Manier. 2018. 'Deregulation and Targeting of TP53 Pathway in Multiple Myeloma', *Front Oncol*, 8: 665.
- Juliusson, G., and R. Hough. 2016. 'Leukemia', *Prog Tumor Res*, 43: 87-100.
- Kang, H., Q. Wu, A. Sun, X. Liu, Y. Fan, and X. Deng. 2018. 'Cancer Cell Glycocalyx and Its Significance in Cancer Progression', *Int J Mol Sci*, 19.
- Kanyo, N., K. D. Kovacs, A. Saftics, I. Szekacs, B. Peter, A. R. Santa-Maria, F. R. Walter, A. Der, M. A. Deli, and R. Horvath. 2020. 'Glycocalyx regulates the strength and kinetics of cancer cell adhesion revealed by biophysical models based on high resolution label-free optical data', *Sci Rep*, 10: 22422.
- Karimi-Busheri, F., V. Zadorozhny, T. Li, H. Lin, D. L. Shawler, and H. Fakhrai. 2011. 'Pivotal role of CD38 biomarker in combination with CD24, EpCAM, and ALDH for identification of H460 derived lung cancer stem cells', *J Stem Cells*, 6: 9-20.
- Kazandjian, D. 2016. 'Multiple myeloma epidemiology and survival: A unique malignancy', *Semin Oncol*, 43: 676-81.
- Khater, I. M., I. R. Nabi, and G. Hamarneh. 2020. 'A Review of Super-Resolution Single-Molecule Localization Microscopy Cluster Analysis and Quantification Methods', *Patterns (N Y)*, 1: 100038.
- Kikuchi, J., M. Hori, H. Iha, N. Toyama-Sorimachi, S. Hagiwara, Y. Kuroda, D. Koyama, T. Izumi, H. Yasui, A. Suzuki, and Y. Furukawa. 2020. 'Soluble SLAMF7 promotes the

- growth of myeloma cells via homophilic interaction with surface SLAMF7', *Leukemia*, 34: 180-95.
- Kiskowski, M. A., J. F. Hancock, and A. K. Kenworthy. 2009. 'On the use of Ripley's K-function and its derivatives to analyze domain size', *Biophys J*, 97: 1095-103.
- Kitamura, N., S. Murata, T. Ueki, E. Mekata, R. T. Reilly, E. M. Jaffee, and T. Tani. 2009. 'OX40 costimulation can abrogate Foxp3+ regulatory T cell-mediated suppression of antitumor immunity', *Int J Cancer*, 125: 630-8.
- Kiyoi, H., N. Kawashima, and Y. Ishikawa. 2020. 'FLT3 mutations in acute myeloid leukemia: Therapeutic paradigm beyond inhibitor development', *Cancer Sci*, 111: 312-22.
- Kiyoi, H., and T. Naoe. 2002. 'FLT3 in human hematologic malignancies', *Leuk Lymphoma*, 43: 1541-7.
- Kondelkova, K., D. Vokurkova, J. Krejsek, L. Borska, Z. Fiala, and A. Ctirad. 2010. 'Regulatory T cells (TREG) and their roles in immune system with respect to immunopathological disorders', *Acta Medica (Hradec Kralove)*, 53: 73-7.
- Kong, S. Y., W. K. Lam, K. S. Li, K. P. Yeung, C. Y. Ha, H. K. Lai, H. N. Chan, Y. M. Yeung, and S. F. Yip. 2018. 'Diagnostic and treatment hurdles in plasma cell myeloma with t(11;14) translocation: A case report', *Mol Clin Oncol*, 8: 757-59.
- Kozak, R. W., R. W. Atcher, O. A. Gansow, A. M. Friedman, J. J. Hines, and T. A. Waldmann. 1986. 'Bismuth-212-labeled anti-Tac monoclonal antibody: alpha-particle-emitting radionuclides as modalities for radioimmunotherapy', *Proc Natl Acad Sci U S A*, 83: 474-8.
- Kriss, T. C., and V. M. Kriss. 1998. 'History of the operating microscope: from magnifying glass to microneurosurgery', *Neurosurgery*, 42: 899-907; discussion 07-8.
- Lagunas-Rangel, F. A., and V. Chavez-Valencia. 2017. 'FLT3-ITD and its current role in acute myeloid leukaemia', *Med Oncol*, 34: 114.
- Lakowicz, J.R. 2013. *Principles of Fluorescence Spectroscopy* (Springer US).
- Lee, S. H., J. Y. Shin, A. Lee, and C. Bustamante. 2012. 'Counting single photoactivatable fluorescent molecules by photoactivated localization microscopy (PALM)', *Proc Natl Acad Sci U S A*, 109: 17436-41.
- Lehmann, J., M. E. Jorgensen, S. Fratz, H. M. Muller, J. Kusch, S. Scherzer, C. Navarro-Retamal, D. Mayer, J. Bohm, K. R. Konrad, U. Terpitz, I. Dreyer, T. D. Mueller, M. Sauer, R. Hedrich, D. Geiger, and T. Maierhofer. 2021. 'Acidosis-induced activation of anion channel SLAH3 in the flooding-related stress response of Arabidopsis', *Curr Biol*.
- Li, X., Y. Ding, M. Zi, L. Sun, W. Zhang, S. Chen, and Y. Xu. 2017. 'CD19, from bench to bedside', *Immunol Lett*, 183: 86-95.
- Liao, S., S. Xiao, G. Zhu, D. Zheng, J. He, Z. Pei, G. Li, and Y. Zhou. 2014. 'CD38 is highly expressed and affects the PI3K/Akt signaling pathway in cervical cancer', *Oncol Rep*, 32: 2703-9.
- Liu, X. L., H. Q. Liu, J. Li, C. Y. Mao, J. T. He, and X. Zhao. 2020. 'Role of epigenetic in leukemia: From mechanism to therapy', *Chem Biol Interact*, 317: 108963.
- Lonial, S., B. Durie, A. Palumbo, and J. San-Miguel. 2016. 'Monoclonal antibodies in the treatment of multiple myeloma: current status and future perspectives', *Leukemia*, 30: 526-35.
- Lu, R. M., Y. C. Hwang, I. J. Liu, C. C. Lee, H. Z. Tsai, H. J. Li, and H. C. Wu. 2020. 'Development of therapeutic antibodies for the treatment of diseases', *J Biomed Sci*, 27: 1.
- Luo, L., R. M. Lucas, L. Liu, and J. L. Stow. 2019. 'Signalling, sorting and scaffolding adaptors for Toll-like receptors', *J Cell Sci*, 133.
- Malzer, C., & Baum, M. 2019. 'A Hybrid Approach To Hierarchical Density-based Cluster Selection.', *arxiv preprint*.
- Munawar, U., L. Rasche, N. Muller, C. Vogt, M. Da-Via, L. Haertle, P. Arampatzi, S. Dietrich, M. Roth, A. Garitano-Trojaola, M. J. Steinhardt, S. Striffler, M. Gallardo, J. Martinez-Lopez, R. C. Bargou, T. Heckel, H. Einsele, T. Stuhmer, K. M. Kortum, and S. Barrio. 2019. 'Hierarchy of mono- and biallelic TP53 alterations in multiple myeloma cell fitness', *Blood*, 134: 836-40.

- Murray, A. J., S. J. Lewis, A. N. Barclay, and R. L. Brady. 1995. 'One sequence, two folds: a metastable structure of CD2', *Proc Natl Acad Sci U S A*, 92: 7337-41.
- Nagar, M., J. Jacob-Hirsch, H. Vernitsky, Y. Berkun, S. Ben-Horin, N. Amariglio, I. Bank, Y. Kloog, G. Rechavi, and I. Goldstein. 2010. 'TNF activates a NF-kappaB-regulated cellular program in human CD45RA- regulatory T cells that modulates their suppressive function', *J Immunol*, 184: 3570-81.
- Naniche, D., S. I. Reed, and M. B. Oldstone. 1999. 'Cell cycle arrest during measles virus infection: a G0-like block leads to suppression of retinoblastoma protein expression', *J Virol*, 73: 1894-901.
- Nerreter, T., S. Letschert, R. Gotz, S. Doose, S. Danhof, H. Einsele, M. Sauer, and M. Hudecek. 2019. 'Super-resolution microscopy reveals ultra-low CD19 expression on myeloma cells that triggers elimination by CD19 CAR-T', *Nat Commun*, 10: 3137.
- Niedzwiecki, M., O. Budzilo, E. Adamkiewicz-Drozynska, D. Pawlik-Gwozdecka, M. Zielinski, L. Maciejka-Kemblowska, T. Szczepanski, and P. Trzonkowski. 2019. 'CD4(+)CD25(high)CD127(low/-)FoxP3 (+) Regulatory T-Cell Population in Acute Leukemias: A Review of the Literature', *J Immunol Res*, 2019: 2816498.
- Niu, H. Q., X. C. Zhao, W. Li, J. F. Xie, X. Q. Liu, J. Luo, W. P. Zhao, and X. F. Li. 2020. 'Characteristics and reference ranges of CD4(+)T cell subpopulations among healthy adult Han Chinese in Shanxi Province, North China', *BMC Immunol*, 21: 44.
- O'Connell, P., Y. Pepelyayeva, M. K. Blake, S. Hyslop, R. B. Crawford, M. D. Rizzo, C. Pereira-Hicks, S. Godbehere, L. Dale, P. Gulick, N. E. Kaminski, A. Amalfitano, and Y. A. Aldhamen. 2019. 'SLAMF7 Is a Critical Negative Regulator of IFN-alpha-Mediated CXCL10 Production in Chronic HIV Infection', *J Immunol*, 202: 228-38.
- Ohue, Y., and H. Nishikawa. 2019. 'Regulatory T (Treg) cells in cancer: Can Treg cells be a new therapeutic target?', *Cancer Sci*, 110: 2080-89.
- Pageon, S. V., T. Tabarin, Y. Yamamoto, Y. Ma, P. R. Nicovich, J. S. Bridgeman, A. Cohnen, C. Benzing, Y. Gao, M. D. Crowther, K. Tungatt, G. Dolton, A. K. Sewell, D. A. Price, O. Acuto, R. G. Parton, J. J. Gooding, J. Rossy, J. Rossjohn, and K. Gaus. 2016. 'Functional role of T-cell receptor nanoclusters in signal initiation and antigen discrimination', *Proc Natl Acad Sci U S A*, 113: E5454-63.
- Palaiologou, M., I. Delladetsima, and D. Tiniakos. 2014. 'CD138 (syndecan-1) expression in health and disease', *Histol Histopathol*, 29: 177-89.
- Panaroni, C., A. J. Yee, and N. S. Raje. 2017. 'Myeloma and Bone Disease', *Curr Osteoporos Rep*, 15: 483-98.
- Pasqualon, T., J. Pruessmeyer, V. Jankowski, A. Babendreyer, E. Groth, J. Schumacher, A. Koenen, S. Weidenfeld, N. Schwarz, B. Denecke, H. Jahr, D. Dreymueller, J. Jankowski, and A. Ludwig. 2015. 'A cytoplasmic C-terminal fragment of Syndecan-1 is generated by sequential proteolysis and antagonizes Syndecan-1 dependent lung tumor cell migration', *Oncotarget*, 6: 31295-312.
- Patnaik, M. M. 2018. 'The importance of FLT3 mutational analysis in acute myeloid leukemia', *Leuk Lymphoma*, 59: 2273-86.
- Patterson, G. H. 2009. 'Fluorescence microscopy below the diffraction limit', *Semin Cell Dev Biol*, 20: 886-93.
- Pavlasova, G., and M. Mraz. 2020. 'The regulation and function of CD20: an "enigma" of B-cell biology and targeted therapy', *Haematologica*, 105: 1494-506.
- Pawelec, G., A. Borowitz, P. H. Krammer, and P. Wernet. 1982. 'Constitutive interleukin 2 production by the JURKAT human leukemic T cell line', *Eur J Immunol*, 12: 387-92.
- Pelcovits, A., and R. Niroula. 2020. 'Acute Myeloid Leukemia: A Review', *R I Med J (2013)*, 103: 38-40.
- Petersen, C. T., and G. Krenciute. 2019. 'Next Generation CAR T Cells for the Immunotherapy of High-Grade Glioma', *Front Oncol*, 9: 69.
- Pocsik, E., R. Mihalik, M. Penzes, H. Loetscher, H. Gallati, and B. B. Aggarwal. 1995. 'Effect of cell cycle on the regulation of the cell surface and secreted forms of type I and type II human tumor necrosis factor receptors', *J Cell Biochem*, 59: 303-16.
- Poulin, E. J., A. K. Bera, J. Lu, Y. J. Lin, S. D. Strasser, J. A. Paulo, T. Q. Huang, C. Morales, W. Yan, J. Cook, J. A. Nowak, D. K. Brubaker, B. A. Joughin, C. W. Johnson, R. A.

- DeStefanis, P. C. Ghazi, S. Gondi, T. E. Wales, R. E. Iacob, L. Bogdanova, J. J. Gierut, Y. Li, J. R. Engen, P. A. Perez-Mancera, B. S. Braun, S. P. Gygi, D. A. Lauffenburger, K. D. Westover, and K. M. Haigis. 2019. 'Tissue-Specific Oncogenic Activity of KRAS(A146T)', *Cancer Discov*, 9: 738-55.
- Prada-Arismendy, J., J. C. Arroyave, and S. Rothlisberger. 2017. 'Molecular biomarkers in acute myeloid leukemia', *Blood Rev*, 31: 63-76.
- Prommersberger, S., M. Reiser, J. Beckmann, S. Danhof, M. Amberger, P. Quade-Lyssy, H. Einsele, M. Hudecek, H. Bonig, and Z. Ivics. 2021. 'CARAMBA: a first-in-human clinical trial with SLAMF7 CAR-T cells prepared by virus-free Sleeping Beauty gene transfer to treat multiple myeloma', *Gene Ther*, 28: 560-71.
- Quentmeier, H., J. Reinhardt, M. Zaborski, and H. G. Drexler. 2003. 'FLT3 mutations in acute myeloid leukemia cell lines', *Leukemia*, 17: 120-4.
- Rajkumar, S. V. 2020. 'Multiple myeloma: 2020 update on diagnosis, risk-stratification and management', *Am J Hematol*, 95: 548-67.
- Rasche, L., H. Einsele, and S. Nitschmann. 2019. '[Treatment of multiple myeloma with elotuzumab plus pomalidomide and dexamethasone]', *Internist (Berl)*, 60: 658-60.
- Reth, M. 2013. 'Matching cellular dimensions with molecular sizes', *Nat Immunol*, 14: 765-7.
- Robert, C. 2020. 'A decade of immune-checkpoint inhibitors in cancer therapy', *Nat Commun*, 11: 3801.
- Robillard, N., H. Avet-Loiseau, R. Garand, P. Moreau, D. Pineau, M. J. Rapp, J. L. Harousseau, and R. Bataille. 2003. 'CD20 is associated with a small mature plasma cell morphology and t(11;14) in multiple myeloma', *Blood*, 102: 1070-1.
- Rodriguez-Lobato, L. G., M. Ganzetti, C. Fernandez de Larrea, M. Hudecek, H. Einsele, and S. Danhof. 2020. 'CAR T-Cells in Multiple Myeloma: State of the Art and Future Directions', *Front Oncol*, 10: 1243.
- Rossboth, B., A. M. Arnold, H. Ta, R. Platzner, F. Kellner, J. B. Huppa, M. Brameshuber, F. Baumgart, and G. J. Schutz. 2018. 'TCRs are randomly distributed on the plasma membrane of resting antigen-experienced T cells', *Nat Immunol*, 19: 821-27.
- Rouge, L., N. Chiang, M. Steffek, C. Kugel, T. I. Croll, C. Tam, A. Estevez, C. P. Arthur, C. M. Koth, C. Ciferri, E. Kraft, J. Payandeh, G. Nakamura, J. T. Koerber, and A. Rohou. 2020. 'Structure of CD20 in complex with the therapeutic monoclonal antibody rituximab', *Science*, 367: 1224-30.
- Rust, M. J., M. Bates, and X. Zhuang. 2006. 'Sub-diffraction-limit imaging by stochastic optical reconstruction microscopy (STORM)', *Nat Methods*, 3: 793-5.
- Sakaguchi, S. 2011. 'Regulatory T cells: history and perspective', *Methods Mol Biol*, 707: 3-17.
- Sakaguchi, S., T. Yamaguchi, T. Nomura, and M. Ono. 2008. 'Regulatory T cells and immune tolerance', *Cell*, 133: 775-87.
- Saltarella, I., V. Desantis, A. Melaccio, A. G. Solimando, A. Lamanuzzi, R. Ria, C. T. Storlazzi, M. A. Mariggio, A. Vacca, and M. A. Frassanito. 2020. 'Mechanisms of Resistance to Anti-CD38 Daratumumab in Multiple Myeloma', *Cells*, 9.
- Sanderson, M. J., I. Smith, I. Parker, and M. D. Bootman. 2014. 'Fluorescence microscopy', *Cold Spring Harb Protoc*, 2014: pdb top071795.
- Scheuermann, R. H., and E. Racila. 1995. 'CD19 antigen in leukemia and lymphoma diagnosis and immunotherapy', *Leuk Lymphoma*, 18: 385-97.
- Schmidt, A., N. Oberle, and P. H. Krammer. 2012. 'Molecular mechanisms of treg-mediated T cell suppression', *Front Immunol*, 3: 51.
- Schonfeld, K., C. Zuber, J. Pinkas, T. Hader, K. Bernoster, and C. Uherek. 2017. 'Indatuximab ravtansine (BT062) combination treatment in multiple myeloma: pre-clinical studies', *J Hematol Oncol*, 10: 13.
- Schreiber, T. H., D. Wolf, M. S. Tsai, J. Chirinos, V. V. Deyev, L. Gonzalez, T. R. Malek, R. B. Levy, and E. R. Podack. 2010. 'Therapeutic Treg expansion in mice by TNFRSF25 prevents allergic lung inflammation', *J Clin Invest*, 120: 3629-40.
- Semrich, M., A. Smith, C. Feterowski, S. Beer, B. Engelhardt, D. H. Busch, B. Bartsch, M. Laschinger, N. Hogg, K. Pfeffer, and B. Holzmann. 2005. 'Importance of integrin LFA-1 deactivation for the generation of immune responses', *J Exp Med*, 201: 1987-98.

- Sen, M., A. C. Koksals, K. Yuki, J. Wang, and T. A. Springer. 2018. 'Ligand- and cation-induced structural alterations of the leukocyte integrin LFA-1', *J Biol Chem*, 293: 6565-77.
- Shahrabi, S., M. Ghanavat, M. M. Behzad, D. Purrahman, and N. Saki. 2020. 'CD markers polymorphisms as prognostic biomarkers in hematological malignancies', *Oncol Rev*, 14: 466.
- Sharma, P., R. Varma, R. C. Sarasij, Ira, K. Gousset, G. Krishnamoorthy, M. Rao, and S. Mayor. 2004. 'Nanoscale organization of multiple GPI-anchored proteins in living cell membranes', *Cell*, 116: 577-89.
- Shattil, S. J., C. Kim, and M. H. Ginsberg. 2010. 'The final steps of integrin activation: the end game', *Nat Rev Mol Cell Biol*, 11: 288-300.
- Shevach, E. M., and A. M. Thornton. 2014. 'tTregs, pTregs, and iTregs: similarities and differences', *Immunol Rev*, 259: 88-102.
- Shevyrev, D., and V. Tereshchenko. 2019. 'Treg Heterogeneity, Function, and Homeostasis', *Front Immunol*, 10: 3100.
- Shim, H. 2020. 'Bispecific Antibodies and Antibody-Drug Conjugates for Cancer Therapy: Technological Considerations', *Biomolecules*, 10.
- Shimizu, J., S. Yamazaki, T. Takahashi, Y. Ishida, and S. Sakaguchi. 2002. 'Stimulation of CD25(+)CD4(+) regulatory T cells through GITR breaks immunological self-tolerance', *Nat Immunol*, 3: 135-42.
- Shimomura, O. 2009. 'Discovery of green fluorescent protein (GFP) (Nobel Lecture)', *Angew Chem Int Ed Engl*, 48: 5590-602.
- Shivanandan, A., J. Unnikrishnan, and A. Radenovic. 2016. 'On characterizing protein spatial clusters with correlation approaches', *Sci Rep*, 6: 31164.
- Soekojo, C. Y., and S. K. Kumar. 2019. 'Stem-cell transplantation in multiple myeloma: how far have we come?', *Ther Adv Hematol*, 10: 2040620719888111.
- Springer, T. A., and J. H. Wang. 2004. 'The three-dimensional structure of integrins and their ligands, and conformational regulation of cell adhesion', *Adv Protein Chem*, 68: 29-63.
- Stirewalt, D. L., and J. P. Radich. 2003. 'The role of FLT3 in haematopoietic malignancies', *Nat Rev Cancer*, 3: 650-65.
- Subklewe, M., M. von Bergwelt-Baildon, and A. Humpe. 2019. 'Chimeric Antigen Receptor T Cells: A Race to Revolutionize Cancer Therapy', *Transfus Med Hemother*, 46: 15-24.
- Swaminathan, M., and E. S. Wang. 2020. 'Novel therapies for AML: a round-up for clinicians', *Expert Rev Clin Pharmacol*, 13: 1389-400.
- Szurek, E., A. Cebula, L. Wojciech, M. Pietrzak, G. Rempala, P. Kisielow, and L. Ignatowicz. 2015. 'Differences in Expression Level of Helios and Neuropilin-1 Do Not Distinguish Thymus-Derived from Extrathymically-Induced CD4+Foxp3+ Regulatory T Cells', *PLoS One*, 10: e0141161.
- Tai, Y. T., C. Acharya, G. An, M. Moschetta, M. Y. Zhong, X. Feng, M. Cea, A. Cagnetta, K. Wen, H. van Eenennaam, A. van Elsas, L. Qiu, P. Richardson, N. Munshi, and K. C. Anderson. 2016. 'APRIL and BCMA promote human multiple myeloma growth and immunosuppression in the bone marrow microenvironment', *Blood*, 127: 3225-36.
- Takada, Y., X. Ye, and S. Simon. 2007. 'The integrins', *Genome Biol*, 8: 215.
- Takeuchi, Y., and H. Nishikawa. 2016. 'Roles of regulatory T cells in cancer immunity', *Int Immunol*, 28: 401-9.
- Tay, R. E., E. K. Richardson, and H. C. Toh. 2021. 'Revisiting the role of CD4(+) T cells in cancer immunotherapy-new insights into old paradigms', *Cancer Gene Ther*, 28: 5-17.
- Thakur, A., M. Huang, and L. G. Lum. 2018. 'Bispecific antibody based therapeutics: Strengths and challenges', *Blood Rev*, 32: 339-47.
- Thalappilly, S., P. Soubeyran, J. L. Iovanna, and N. J. Dusetti. 2010. 'VAV2 regulates epidermal growth factor receptor endocytosis and degradation', *Oncogene*, 29: 2528-39.
- Thomas, A., B. A. Teicher, and R. Hassan. 2016. 'Antibody-drug conjugates for cancer therapy', *Lancet Oncol*, 17: e254-e62.
- Thornton, A. M., J. Lu, P. E. Korty, Y. C. Kim, C. Martens, P. D. Sun, and E. M. Shevach. 2019. 'Helios(+) and Helios(-) Treg subpopulations are phenotypically and functionally distinct and express dissimilar TCR repertoires', *Eur J Immunol*, 49: 398-412.

- Togashi, Y., K. Shitara, and H. Nishikawa. 2019. 'Regulatory T cells in cancer immunosuppression - implications for anticancer therapy', *Nat Rev Clin Oncol*, 16: 356-71.
- Tran, D. Q., J. Andersson, R. Wang, H. Ramsey, D. Unutmaz, and E. M. Shevach. 2009. 'GARP (LRRC32) is essential for the surface expression of latent TGF-beta on platelets and activated FOXP3+ regulatory T cells', *Proc Natl Acad Sci U S A*, 106: 13445-50.
- Traynelis, S. F., L. P. Wollmuth, C. J. McBain, F. S. Menniti, K. M. Vance, K. K. Ogden, K. B. Hansen, H. Yuan, S. J. Myers, and R. Dingledine. 2010. 'Glutamate receptor ion channels: structure, regulation, and function', *Pharmacol Rev*, 62: 405-96.
- van de Linde, S., A. Loschberger, T. Klein, M. Heidebreder, S. Wolter, M. Heilemann, and M. Sauer. 2011. 'Direct stochastic optical reconstruction microscopy with standard fluorescent probes', *Nat Protoc*, 6: 991-1009.
- Venken, Koen, Niels Hellings, Roland Liblau, and Piet Stinissen. 'Disturbed regulatory T cell homeostasis in multiple sclerosis', *Trends in Molecular Medicine*, 16: 58-68.
- Verma, A., R. Mathur, A. Farooque, V. Kaul, S. Gupta, and B. S. Dwarakanath. 2019. 'T-Regulatory Cells In Tumor Progression And Therapy', *Cancer Manag Res*, 11: 10731-47.
- Vicidomini, G., P. Bianchini, and A. Diaspro. 2018. 'STED super-resolved microscopy', *Nat Methods*, 15: 173-82.
- Waldchen, F., J. Schlegel, R. Gotz, M. Luciano, M. Schnermann, S. Doose, and M. Sauer. 2020. 'Whole-cell imaging of plasma membrane receptors by 3D lattice light-sheet dSTORM', *Nat Commun*, 11: 887.
- Wang, K., G. Wei, and D. Liu. 2012. 'CD19: a biomarker for B cell development, lymphoma diagnosis and therapy', *Exp Hematol Oncol*, 1: 36.
- Whilding, L. M., and J. Maher. 2015. 'CAR T-cell immunotherapy: The path from the by-road to the freeway?', *Mol Oncol*, 9: 1994-2018.
- White, R., F. Stanley, J. Than, A. Macnair, J. Pethick, G. Fallica, L. Hounsome, and J. Maher. 2021. 'Treatable but not curable cancer in England: a retrospective cohort study using cancer registry data and linked data sets', *BMJ Open*, 11: e040808.
- WHO. 1984. 'Nomenclature for clusters of differentiation (CD) of antigens defined on human leukocyte populations. IUIS-WHO Nomenclature Subcommittee', *Bull World Health Organ*, 62: 809-15.
- Wilschut, L. I., A. Laudisoit, N. K. Hughes, E. A. Addink, S. M. de Jong, H. A. Heesterbeek, J. Reijnders, S. Eagle, V. M. Dubyanskiy, and M. Begon. 2015. 'Spatial distribution patterns of plague hosts: point pattern analysis of the burrows of great gerbils in Kazakhstan', *J Biogeogr*, 42: 1281-92.
- Wolter, S., A. Loschberger, T. Holm, S. Aufmkolk, M. C. Dabauvalle, S. van de Linde, and M. Sauer. 2012. 'rapidSTORM: accurate, fast open-source software for localization microscopy', *Nat Methods*, 9: 1040-1.
- Wu, Y., and H. Shroff. 2019. 'Author Correction: Faster, sharper, and deeper: structured illumination microscopy for biological imaging', *Nat Methods*, 16: 205.
- Xing, R., Y. Zhou, J. Yu, Y. Yu, Y. Nie, W. Luo, C. Yang, T. Xiong, W. K. K. Wu, Z. Li, Y. Bing, S. Lin, Y. Zhang, Y. Hu, L. Li, L. Han, C. Yang, S. Huang, S. Huang, R. Zhou, J. Li, K. Wu, D. Fan, G. Tang, J. Dou, Z. Zhu, J. Ji, X. Fang, and Y. Lu. 2019. 'Whole-genome sequencing reveals novel tandem-duplication hotspots and a prognostic mutational signature in gastric cancer', *Nat Commun*, 10: 2037.
- Xu, Y. J., A. Singh, and G. M. Alter. 2016. 'Hydroxyurea Induces Cytokinesis Arrest in Cells Expressing a Mutated Sterol-14alpha-Demethylase in the Ergosterol Biosynthesis Pathway', *Genetics*, 204: 959-73.
- Yau, Chun Yip, and Ji Meng Loh. 2012. 'A GENERALIZATION OF THE NEYMAN-SCOTT PROCESS', *Statistica Sinica*, 22: 1717-36.
- Yu, T., B. Chaganty, L. Lin, L. Xing, B. Ramakrishnan, K. Wen, P. A. Hsieh, A. Wollacott, K. Viswanathan, H. Adari, S. F. Cho, Y. Li, H. Chen, W. Yang, Y. Xu, G. An, L. Qiu, N. Munshi, G. Babcock, Z. Shriver, J. R. Myette, K. C. Anderson, and Y. T. Tai. 2020. 'VIS832, a novel CD138-targeting monoclonal antibody, potently induces killing of

- human multiple myeloma and further synergizes with IMiDs or bortezomib in vitro and in vivo', *Blood Cancer J*, 10: 110.
- Zamagni, E., M. Cavo, B. Fakhri, R. Vij, and D. Roodman. 2018. 'Bones in Multiple Myeloma: Imaging and Therapy', *Am Soc Clin Oncol Educ Book*, 38: 638-46.
- Zander, H., S. Muller-Egert, M. Zwiewka, S. Gross, G. van Zandbergen, and J. Engelbergs. 2020. '[Checkpoint inhibitors for cancer therapy]', *Bundesgesundheitsblatt Gesundheitsforschung Gesundheitsschutz*, 63: 1322-30.
- Zhang, H., H. Kong, X. Zeng, L. Guo, X. Sun, and S. He. 2014. 'Subsets of regulatory T cells and their roles in allergy', *J Transl Med*, 12: 125.
- Zhang, P., F. Gao, Q. Wang, X. Wang, F. Zhu, C. Ma, W. Sun, and L. Zhang. 2007. 'Agonistic anti-4-1BB antibody promotes the expansion of natural regulatory T cells while maintaining Foxp3 expression', *Scand J Immunol*, 66: 435-40.
- Zheng, S. G., J. Wang, P. Wang, J. D. Gray, and D. A. Horwitz. 2007. 'IL-2 is essential for TGF-beta to convert naive CD4+CD25- cells to CD25+Foxp3+ regulatory T cells and for expansion of these cells', *J Immunol*, 178: 2018-27.
- Zou, F., X. Wang, X. Han, G. Rothschild, S. G. Zheng, U. Basu, and J. Sun. 2018. 'Expression and Function of Tetraspanins and Their Interacting Partners in B Cells', *Front Immunol*, 9: 1606.

List of abbreviations

<i>ADCC</i>	Antibody-dependent cell-mediated cytotoxicity
<i>AF</i>	Alexa Fluor
<i>BiTE</i>	Bi-specific T-cell engagers
<i>CAR-T cell</i>	Chimeric Antigen Receptor T cells
<i>CD</i>	Cluster of differentiation
<i>CDC</i>	complement dependent cytotoxicity
<i>CRISPR/Cas</i>	Clustered Regularly Interspaced Short Palindromic Repeats / CRISPR-associated
<i>DBSCAN</i>	Density-Based Spatial Clustering of Applications with Noise
<i>DOL</i>	Degree of labeling
<i>dSTORM</i>	<i>Direct</i> stochastic optical reconstruction microscopy
<i>FA</i>	Formaldehyde
<i>FcR</i>	fragment crystallisable region
<i>GA</i>	Glutaraldehyde
<i>gam</i>	Goat-anti-mouse
<i>gar</i>	Goat-anti-rabbit
<i>IgG</i>	Immunoglobulin G
<i>IgM</i>	Immunoglobulin M
<i>IL-2</i>	Interleukin-2
<i>KRAS</i>	Kirsten RA ^t Sarcoma
<i>mAb</i>	Monoclonal antibody
<i>MID</i>	Midostaurin
<i>MM</i>	Multiple Myeloma
<i>MOC</i>	Manders overlap coefficient
<i>NK cell</i>	Natural killer cell
<i>pAb</i>	Polyclonal antibody
<i>PALM</i>	Photoactivated Localization <i>Microscopy</i>
<i>PBS</i>	Phosphate buffered saline
<i>pdf</i>	Probability density function

<i>PDL</i>	Poly-D-lysine
<i>px</i>	pixel
<i>s.d.</i>	Standard deviation
<i>s.e.</i>	Standard error
<i>scFv</i>	Single-chain variable fragment
<i>Tcon</i>	Conventional T cell
<i>Treg</i>	Regulatory T cell
<i>WT</i>	Wild type

Acknowledgement

I want to thank all my friends, my family and all the people who accompanied me during my last years in Würzburg for their support, but also the time spent. Without you, none of this would be possible. I am grateful for all of you!

First of all, I would like to thank Prof. Dr. Markus Sauer for giving me the opportunity to perform my master and PhD thesis within his group. It was exciting to work on so many different projects and especially so closely with clinical applications, but also to contribute my own ideas to this rather new field. Thank you Markus, for all your support during the last years!

I would also like to thank PD Dr. Sören Doose for his support during my PhD thesis and the help with the cluster analysis and all the time spent to discuss the massive pile of data.

I also want to thank all my collaboration partners from the University Hospital in Würzburg. First of all to Martin Kortüm and Cornelia Vogt who introduced me to the field of hematologic diseases, like multiple myeloma, and all the clinical input on the applied personalized immunotherapies.

Also I want to thank Dr. Sabrina Kraus and Dr. Andoni Garitano-Trojaola who introduced me to the field of leukemia and gave me a more immunological view of this disease.

For the constant supply of T regulator cells I want to thank Prof. Dr. Andreas Beilhack and Dr. Julia Delgado Tascón, but also for the helpful discussions and the insights how the immune response is regulated.

I would like to acknowledge Lisa Behringer-Pließ, Petra Geßner, Elke Meier, Ivan Simeonov, Marcus Behringer, Albert Gessner and Oliver Reichert who not only provided me with countless cells, but also helped to keep everything running.

A special thanks goes to Alexander Kuhlemann, Suhaila Rajab, Charlotte Rat and Jonathan Schubert. I was always happy sharing an office with you and it never got boring.

Last but not least, I would like to thank all the members of the Department of Biotechnology and Biophysics, from whom many friendships have developed. You all

contributed to this great working atmosphere and made sure that even a frustrating working day was bearable. Many thanks for that!

Publication list

(#) Targetable conformationally restricted cyanines enable photon-count limited applications (2021, Chemrxiv)

Patrick Eiring, Ryan McLaughlin, Siddharth S. Matikonda, Han Zhongying, Lennart Grabenhorst, Dominic A. Helmerich, Mara Meub, Gerti Beliu, Michael Luciano, Venu Bandi, Niels Zijlstra, Zhen-Dan Shi, Rolf Swenson, Philip Tinnefeld, Viktorija Glembockyte, Thorben Cordes, Markus Sauer and Martin J. Schnermann

<https://doi.org/10.26434/chemrxiv.14720883.v1>

Further Publications

Platelet lamellipodia formation is not required for thrombus formation and stability (2019, Blood)

Yvonne Schurr, Andreas Sperr, Julia Volz, Sarah Beck, Lucy Reil, Charly Kusch, Sheila Bryson, **Patrick Eiring**, Markus Sauer, Bernhard Nieswandt, Laura Machesky

<https://doi.org/10.1182/blood.2019002105>

(#) Actin cytoskeleton deregulation confers Midostaurin resistance in FLT3 mutant Acute Myeloid Leukemia (2021, Communications Biology)

Andoni Garitano-Trojaola, Ana Sancho, Ralph Götz, **Patrick Eiring**, Susanne Walz, Hardikkumar Jetani, Jesus Gil-Pulido, Matteo Claudio Da Vià, Eva Teufel, Nadine Rhodes, Larissa Haertle, Estibaliz Arellano, Raoul Tibes, Andreas Rosenwald, Leo Rasche, Michael Hudecek, Juergen Groll, Markus Sauer, Hermann Einsele, Sabrina Kraus

<https://doi.org/10.1038/s42003-021-02215-w>

(#) publication is associated with the dissertation

Affidavit

Eidesstattliche Erklärungen nach §7 Abs. 2 Satz 3, 4, 5 der Promotionsordnung der Fakultät für Biologie

Eidesstattliche Erklärung

Hiermit erkläre ich an Eides statt, die Dissertation: „**Hochauflösende Mikroskopie von Plasmamembran Rezeptoren**“, eigenständig, d. h. insbesondere selbständig und ohne Hilfe eines kommerziellen Promotionsberaters, angefertigt und keine anderen, als die von mir angegebenen Quellen und Hilfsmittel verwendet zu haben.

Ich erkläre außerdem, dass die Dissertation weder in gleicher noch in ähnlicher Form bereits in einem anderen Prüfungsverfahren vorgelegen hat.

Weiterhin erkläre ich, dass bei allen Abbildungen und Texten bei denen die Verwertungsrechte (Copyright) nicht bei mir liegen, diese von den Rechtsinhabern eingeholt wurden und die Textstellen bzw. Abbildungen entsprechend den rechtlichen Vorgaben gekennzeichnet sind sowie bei Abbildungen, die dem Internet entnommen wurden, der entsprechende Hypertextlink angegeben wurde.

Affidavit

I hereby declare that my thesis entitled: „**Super-resolution microscopy of plasma membrane receptors**“ is the result of my own work. I did not receive any help or support from commercial consultants. All sources and / or materials applied are listed and specified in the thesis.

Furthermore I verify that the thesis has not been submitted as part of another examination process neither in identical nor in similar form.

Besides I declare that if I do not hold the copyright for figures and paragraphs, I obtained it from the rights holder and that paragraphs and figures have been marked according to law or for figures taken from the internet the hyperlink has been added accordingly.

Würzburg, den _____

Signature PhD-student

Curriculum vitae

Patrick Eiring

Born 26.03.1993 in Schweinfurt

Education:

1999 – 2003 Primary school Aidhausen
2003 – 2011 High school Regiomontanus, Haßfurt, Germany

Higher Education:

2011 - 2015 Biology B.Sc.
 Julius-Maximilians-University, Wuerzburg
 (Der Einfluss von Modulatoren auf die *Xmrk*-vermittelte
 Tumorentstehung *in vivo* und *in vitro*)
 Supervisor: Prof. Dr. Manfred Scharl

2015 - 2017 Biology M.Sc.
 Julius-Maximilians-University, Wuerzburg
 (Characterization of membrane receptors with a super
 resolution microscopy method)
 Supervisor: Prof. Dr. Markus Sauer

2017 - Present PhD-student
 Department of Biotechnology and Biophysics
 Julius-Maximilians-University, Wuerzburg
 Supervisor: Prof. Dr. Markus Sauer

Würzburg, _____

Patrick Eiring